

3D Scaffolds with Integrated Electrodes for Neuronal Cell Culture

Jamal Abu Shihada

Information

Band / Volume 103

ISBN 978-3-95806-756-1

Forschungszentrum Jülich GmbH
Institut für Biologische Informationsprozesse (IBI)
Bioelektronik (IBI-3)

3D Scaffolds with Integrated Electrodes for Neuronal Cell Culture

Jamal Abu Shihada

Schriften des Forschungszentrums Jülich
Reihe Information / Information

Band / Volume 103

ISSN 1866-1777

ISBN 978-3-95806-756-1

Bibliografische Information der Deutschen Nationalbibliothek.
Die Deutsche Nationalbibliothek verzeichnet diese Publikation in der
Deutschen Nationalbibliografie; detaillierte Bibliografische Daten
sind im Internet über <http://dnb.d-nb.de> abrufbar.

Herausgeber
und Vertrieb: Forschungszentrum Jülich GmbH
 Zentralbibliothek, Verlag
 52425 Jülich
 Tel.: +49 2461 61-5368
 Fax: +49 2461 61-6103
 zb-publikation@fz-juelich.de
 www.fz-juelich.de/zb

Umschlaggestaltung: Grafische Medien, Forschungszentrum Jülich GmbH

Titelbild: Taken from Abu Shihada et al., Highly Customizable 3D Microelectrode
 Arrays for In Vitro and In Vivo Neuronal Tissue Recordings; Advanced Science,
 Volume 11, Issue 13; 2024

Druck: Grafische Medien, Forschungszentrum Jülich GmbH

Copyright: Forschungszentrum Jülich 2024

Schriften des Forschungszentrums Jülich
Reihe Information / Information, Band / Volume 103

D 82 (Diss. RWTH Aachen University, 2024)

ISSN 1866-1777
ISBN 978-3-95806-756-1

Vollständig frei verfügbar über das Publikationsportal des Forschungszentrums Jülich (JuSER)
unter www.fz-juelich.de/zb/openaccess.



This is an Open Access publication distributed under the terms of the [Creative Commons Attribution License 4.0](https://creativecommons.org/licenses/by/4.0/),
which permits unrestricted use, distribution, and reproduction in any medium, provided the original work is properly cited.

Abstract

Three-dimensional (3D) neuronal systems like neuronal tissues and organoids have become increasingly important in neural science as, due to their 3D nature, they provide a more realistic environment of the brain and thus can mimic specific brain regions more precisely than two-dimensional (2D) systems. However, these 3D systems need additional structures, called scaffolds, which support the neuronal growth in all three dimensions. Recent technological advances in microfabrication can be used to improve the quality of the scaffolds, and thus of the 3D systems. To get a better understanding of the complex 3D environment within such 3D systems it is furthermore essential to monitor the electrical activities of these environments. To be able to monitor electrical signals in all three dimensions real 3D electrodes have to be used as conventional 2D electrodes only can monitor surface activities. Therefore, this work introduces a new platform for real 3D electrodes as well as 3D scaffold systems to investigate different 3D neuronal systems. First of all, hollow cylinders are printed onto different 2D substrates with the help of a two-photon polymerization 3D printer. A template-assisted electrochemical deposition process of gold is used to extend the electrodes into the third dimension. 3D electrodes with less than 10 μm diameter and up to 150 μm height are then used to monitor spontaneous as well as light-induced electrical activities from extracted rat retina and human brain slices in different depths of the tissues. Finally, 3D electrodes are integrated into a scaffold system to enable a profound analysis of precisely controlled 3D neuronal environments. The high resolution stiff scaffold system is fabricated with using a two-photon polymerization process and supports the growth of embryonic, cortical rat neurons in all three dimensions. After the network has been established electrical signals with high amplitudes were monitored in different heights within the network. This combined approach allows for a comprehensive investigation of 3D neuronal in-vitro platforms at any life cycle stage.

Zusammenfassung

Dreidimensionale (3D) neuronale Systeme wie neuronale Gewebe und Organoide haben in der Neurowissenschaft zunehmend an Bedeutung gewonnen, da sie aufgrund ihrer 3D-Natur eine realistischere Abbildung des Gehirns bieten und somit bestimmte Gehirnregionen präziser nachbilden können als zweidimensionale (2D) Systeme. Allerdings benötigen diese 3D-Systeme zusätzliche Strukturen, so genannte Scaffolds, die das neuronale Wachstum in allen drei Dimensionen unterstützen. Aktuelle technologische Fortschritte in der Mikrofabrikation können genutzt werden, um die Qualität der Gerüste und damit der 3D-Systeme zu verbessern. Um ein besseres Verständnis der komplexen 3D-Umgebung in solchen 3D-Systemen zu erlangen ist es außerdem wichtig, die elektrischen Aktivitäten dieser Systeme zu messen. Um die Ableitung elektrischer Signale in allen drei Dimensionen zu ermöglichen, müssen 3D-Elektroden verwendet werden, da herkömmliche 2D-Elektroden nur Oberflächenaktivitäten messen können. Daher wird in dieser Arbeit eine neue Plattform für 3D-Elektroden sowie 3D-Gerüstsysteme zur Untersuchung verschiedener neuronaler 3D-Systeme vorgestellt. Zunächst werden Hohlzylinder mit Hilfe eines 3D-Druckers auf Basis der Zwei-Photonen-Polymerisation auf verschiedene 2D-Substrate gedruckt. Ein schablonengestützter elektrochemischer Abscheidungsprozess von Gold wird verwendet, um die Elektroden in die dritte Dimension zu erweitern. 3D-Elektroden mit einem Durchmesser von weniger als $10 \mu\text{m}$ und einer Höhe von bis zu $150 \mu\text{m}$ werden dann verwendet, um sowohl spontane als auch lichtinduzierte elektrische Aktivitäten von extrahierten Rattennetzhäuten und menschlichen Hirnschnitten in verschiedenen Gewebetiefen abzuleiten. Schließlich werden 3D-Elektroden in ein Gerüstsystem integriert, um eine tiefgreifende Analyse von präzise kontrollierten neuronalen 3D-Umgebungen zu ermöglichen. Das hochauflösende steife Gerüstsystem wird mit Hilfe eines Zwei-Photonen-Polymerisationsverfahrens hergestellt und unterstützt das Wachstum embryonaler, kortikaler Rattenneuronen in allen drei Dimensionen. So konnten elektrische Signale mit hohen Amplituden in verschiedenen Höhen innerhalb des Netzwerks gemessen werden. Dieser kombinierte Ansatz ermöglicht eine umfassende Untersuchung von neuronalen 3D-Plattformen in-vitro in jedem Lebenszyklusstadium.

Contents

Abstract	i
Zusammenfassung	ii
Abbreviations	vi
1 Introduction	1
2 Theoretical Background	6
2.1 Tissue Engineering	6
2.2 Multi-Photon Polymerization	7
2.3 Electrochemical Deposition	12
2.3.1 Metal	12
2.3.2 Polymer	15
2.4 Cell-Electrode-Interface	16
2.4.1 Cell Potential	16
2.4.2 Neuron	19
2.4.3 Electrode-Electrolyte Interface	20
2.4.4 Impedance	24
2.5 3D Tissue	26
2.5.1 The Brain	26
2.5.2 The Retina	26
2.6 Neuronal Implants	28
2.6.1 Brain Implants	28
2.6.2 Retina Implants	29
2.7 3D Electrodes	29
3 Materials and Methods	32
3.1 Microfabrication of Microelectrode Arrays	32
3.1.1 2D stiff MEA	32
3.1.2 2D flexible MEA	33
3.2 3D Microstructure Fabrication	34
3.3 Template-assisted Electrodeposition of Conductive Material	34
3.3.1 Electrodeposition of Gold	34

3.3.2	Electrodeposition of PEDOT:PSS	35
3.4	Electrochemical Impedance Spectroscopy	35
3.5	In-vitro Cell Culture	35
3.5.1	Fluorescent Microscopy	36
3.5.2	Cell Fixation and SEM	37
3.6	Ex-vivo Rat Retina	37
3.7	Ex-vivo Human Brain Slice	38
3.8	Electrophysiology	39
3.8.1	Stiff Samples	39
3.8.2	Flexible Samples	39
4	3D Neuronal In-Vitro System	41
4.1	Optimization of 3D Print	42
4.2	Optimization of the Stacking Process	47
4.3	Increasing Stack Stability	52
4.4	Investigation of 3D Neuronal Networks	59
4.4.1	Fluorescent Microscopy Investigation	59
4.4.2	SEM Investigation	62
5	3D Microelectrode Array	65
5.1	3D Electrodes	65
5.1.1	3D Electrode concept	65
5.1.2	Adhesion	69
5.1.3	Aspect Ratio Resolution	74
5.2	Towards a 3D MEA device	81
5.2.1	Stiff Probes	82
5.2.2	Flexible Probes	82
5.2.3	Electrochemical Deposition	85
5.2.4	Electrochemical Performance	100
5.3	Ex-vivo Experiments	109
5.3.1	Flexible Implants	109
5.3.2	Ex-vivo Rat Retina with Stiff Probes	117
5.4	Stability of PEDOT:PSS	120

6 Investigating 3D Neuronal Networks	123
6.1 Scaffold System	123
6.2 Electrochemical Deposition of Gold	132
6.3 Primary Cortical Embryonic Rat Neurons	133
7 Summary and Outlook	139
8 References	143
List of Figures	153
Acknowledgements	162

Abbreviations

2D	two-dimensional
3D	three-dimensional
DLW	direct laser writing
MPP	multi-photon polymerization
PDMS	Polydimethylsiloxane
CMOS	complementary metal-oxide-semiconductor
MEA	microelectrode array
TPP	two-photon polymerization
ECM	extracellular matrix
TPA	two-photon absorption
SHE	standard hydrogen electrode
Ag	silver
AgCl	silver chloride
Au	gold
Cl	chloride
SCE	saturated calomel electrode
CP	conductive polymers
CSC	charge storage capacity
CIC	charge injection capacity
PEDOT	poly 3,4-ethylenedioxythiophene
PSS	poly(styrenesulfonate)
AP	action potential
EIS	electrochemical impedance spectroscopy
AC	alternate current
DC	direct current
SNR	signal-to-noise ratio
IPA	Isopropanol

RIE	reactive ion etching
CAD	computer-aided design
CV	cyclic voltammetry
DIV	days in-vitro
SEM	scanning electron microscopy
CPD	critical point drying
PCB	printed circuit board
GCL	ganglion cell layer
NFL	nerve fiber layer
IPL	inner plexiform layer

1 Introduction

As one of our most important organs the human brain has fascinated scientist already for centuries. It consists of billions of neurons and synapses and is a highly complex and dynamic system [1]. Therefore, studying and understanding of the human brain and the disrupted mechanisms of neural activity in neurological diseases is still a crucial challenge in neuroscience. One straight forward and powerful tool to study the brain is using in-vitro neuronal networks which partially mimic the structures in the brain in a controlled environment. That is why, they can lead to a better understanding of neurological diseases such as Alzheimer's disease, Parkinson's diseases, and epilepsy [2][3][4][5]. So far most of the investigated in-vitro networks are simple and cost-effective two-dimensional (2D) neuronal cultures. Nevertheless, they limit cell-cell as well as cell-matrix interactions and signaling to a single plane, and therefore cannot represent and predict the three-dimensional (3D) environment of the brain very precisely [6]. 3D cultures have recently attracted the interest of scientists as they can mimic living tissue more precisely, and thus provide a more controlled, reproducible, and realistic environment with longer lifespan [6][7][8][9][10]. In in-vitro 3D neuronal networks cultured neurons are organized into 3D structures like organoids, spheroids, and micro tissues to mimic specific brain regions and cell types [11][12][13]. These structures are used to investigate neural activities, the propagation of neuronal signals in all three dimensions, neuronal plasticity, the effects of drugs and potential treatments for neurological disorders, and many more [14][15]. Recent technological advances in microfabrication and tissue engineering have improved the quality of 3D neuronal environments in the last years [16][17]. In general, for 3D environments scaffolds as growth supporting material are needed. It can be distinguished between two families of scaffolds. Either soft or hard biomaterials can be used. Soft biomaterials have the advantage that cells can grow with high degree of freedom, and they mimic the soft environment of biological tissues. However, these scaffolds generate random, not spatially controllable 3D neuronal networks. Mostly hydrogels are used as supporting material for soft scaffolds [18]. In contrast to soft scaffolds, by using hard biomaterials the growth is supported by solid scaffolds made from Polydimethylsiloxane (PDMS), graphene, photoresist scaffolds, and many more. Solid scaffolds enable higher structural complexity and increased cell survival. In addition, it is possible to control the cell growth with adjusting the scaffold design which results in a spatially well-defined 3D neuronal

network [7][8][15]. However, this requires scaffolds with feature sizes of a few μm and complex geometries. Direct laser writing (DLW) by multi-photon polymerization (MPP) is an attractive method for fabricating precisely controlled cell scaffolds for 3D neuronal networks [7][15]. It is a 3D printing technology based on the photon absorption by photopolymers. The non-linear physics of the absorption process allows the fabrication of complex polymer structures with sub-100 nm resolution [19]. Therefore, it enables the reliable fabrication of arbitrary geometries with the resolution of sub-cellular structures using biocompatible and non-toxic polymers. Cultivating neurons onto these scaffolds leads to the growth of a 3D neuronal network which can be precisely controlled by adjusting the scaffold geometry. Furthermore, different cell adhesion and cell repellent coatings can be applied to different regions of the scaffold to further tailor the system [20]. In the first part of this work 3D cage-like scaffolds with high resolution are used to introduce a platform for stable 3D neuronal environments using the two-photon polymerization (TPP) process. The used cage-like scaffold geometry is based on the work from Larramendy et al. [7]. In-vitro experiments are conducted to show the suitability of the scaffold system for neurite growth in all three dimensions.

To fully understand the different functions of the brain the monitoring of electrical neural activities from complex 3D neuronal environments is essential. The monitoring should have a high spatial resolution and happen over extended time periods. Microelectrode arrays are the most used devices to monitor electrical signals of neural activities. They can record multiple neurons simultaneously over a big area. However, due to their 2D nature they are inappropriate to investigate 3D neuronal tissue like brain slices, organoids, or in-vitro 3D networks as the planar microelectrodes can only monitor surface neural activity from the outside of the tissue [21]. Furthermore, the signal quality recorded by such planar electrodes is too low to profoundly analyze synaptic potentials [22]. To address these challenges implantable neuronal electrodes are used to record and stimulate deep inside the 3D tissue. For a use as a brain computer interface and to properly investigate cognitive processes in the brain such implants need to have high electrode densities. Furthermore, it is important that these implants can successfully reach and target regions of interest within the brain [23][24][25][26]. Recent developments in advanced microfabrication methods led to high density complementary metal-oxide-semiconductor (CMOS) based neuropixel probes using silicon as substrate material. Nevertheless, the high stiffness of the probes leads to functional failures

[27][28]. Two types, the “Utah” and “Michigan” platform, have been mostly used in neuroscience [29][30]. In the “Utah” platform thin silicon needles penetrate the tissue. However, due to its fabrication method the height of the needles can only be varied in a single plane (slanted height) [29]. In addition, the fabrication method limits the spacing between the needles and thus the recording density. Another approach stacks several in-plane Michigan-like arrays onto each other to achieve a real three dimensionality of the implant. However, the electrode density is limited to the spacing between each array which is needed for assembly and bonding [31][32]. Next to stiff silicon-based implants, neuroengineers recently have focused on flexible polymer based neuronal implants. Their mechanical properties are more compliant with the soft tissue of the brain which reduces the damage of the tissue and increases long-term stability. In this regard, thin, flexible “Michigan”-like retina implants could monitor cell activity across multiple depths within the retina while being minimal invasive [33]. However, flexible implants always need advanced implantation methods to be able to penetrate the tissue [34]. To target specific region of interest in different depth of 3D structures like for instant tissues and organoids real multi-level 3D neuronal implants are necessary. So far, many different approaches have been published to address the challenge of fabricating high density 3D electrodes. A 3D ink-jet print approach has been used to fabricate conductive micropillars with arbitrary heights, diameters, and electrode designs onto a 2D microelectrode array (MEA) substrate and then applied in in-vivo experiments [35][36]. Another research group fabricated a 2D mesh consisting of holey-like structures with electrodes at the edges or vertices. The mesh will then deform and conform according to the 3D biological target [37]. Furthermore, a folding of 2D “Michigan”-like shanks can lead to a flexible 3D microelectrode array [38]. Finally, the TPP printing technique has been used to print complex 3D conductive or non-conductive structures onto a 2D substrate [39] [40]. However, all the mentioned approaches require additional complex microfabrication steps like lithography and selective etching or are limited in the choice of materials and 3D electrode dimensions.

Therefore, the second part of this work introduces a new platform for real multi-site 3D electrode implants. The TPP process is used to print hollow cylinders with arbitrary heights and designs onto a 2D substrate. Template-assisted electrochemical deposition through these cylinders lead to high aspect ratio 2D electrodes with diameters below 10 μm and several 100 μm in height. The electrode arrays are used ex-vivo to monitor

neuronal activity of rat retina as well as human brain slices in different depths. All the electrode dimensions and designs can be easily adapted to the targeted tissue and can be tailored to the unique needs of the patient for future applications. Furthermore, this approach can be used with stiff as well as flexible substrates.

Finally, the last part of this work combines the first two parts, and thus introduces a platform for electrical characterization and profound analysis of highly controlled in-vitro 3D neuronal networks or neuronal structures like organoids. The TPP technique is used to simultaneously print the 3D scaffold design introduced in the first part and the hollow cylinders used in the second part. Electrochemical deposition is again used to fabricate the 3D electrodes within the scaffold for high signal recording of in-vitro networks.

Figure 1 summarizes the overall structure of this work.

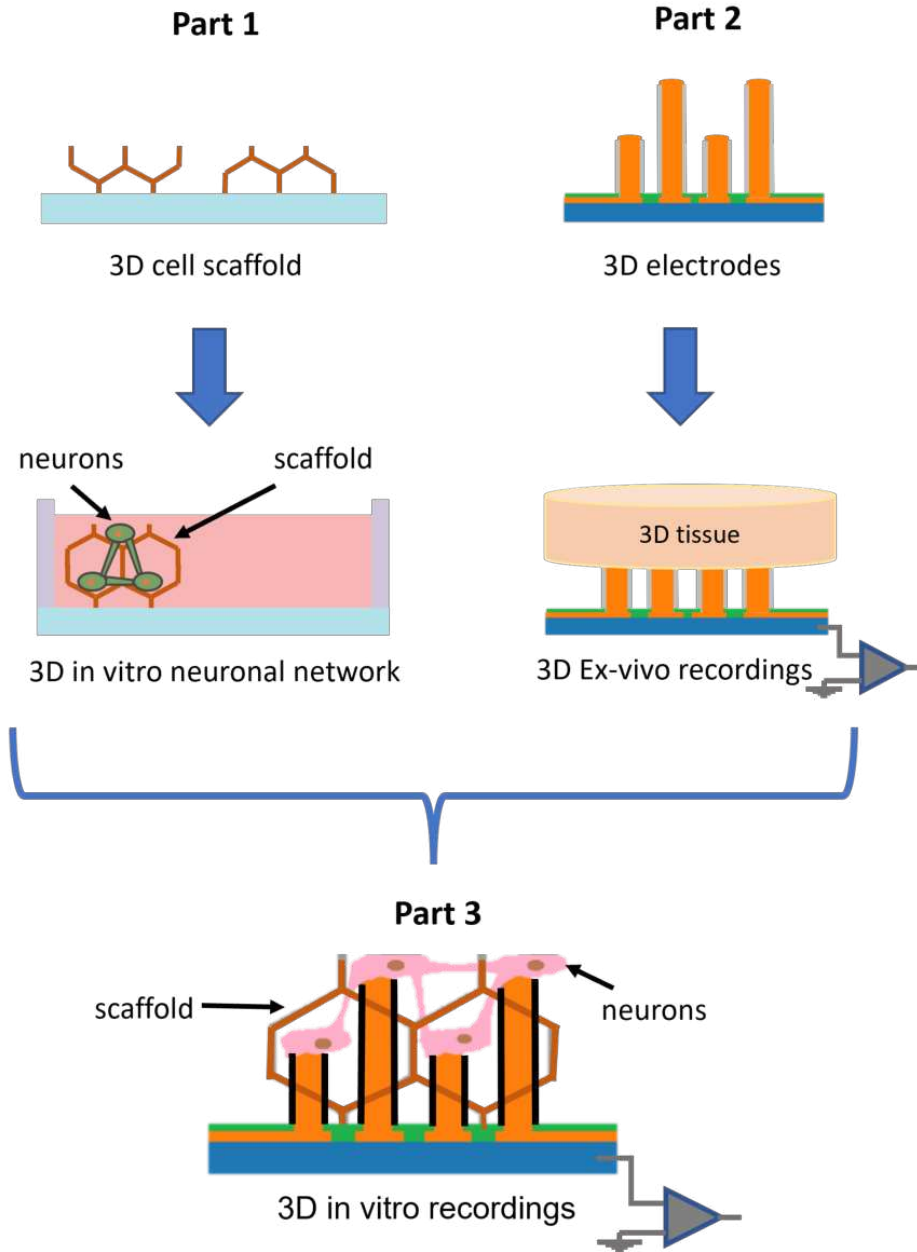


Fig. 1: Structure of the work. Part 1 illustrates the workflow for 3D scaffold system. Part 2 shows the new platform for real three-dimensional electrodes. Finally, part 3 combines part 1 and 2 with integrating 3D electrodes into the scaffold system.

2 Theoretical Background

2.1 Tissue Engineering

Tissue engineering is an interdisciplinary field that aims to develop functional replacement for tissues and organs for clinical applications with creating 3D complex structures that mimic the organization and function of native tissues. To do so, a broad understanding of how the native tissue works in 3D is of great importance. To get a better understanding 3D neuronal culture have emerged as a promising approach to model the complex structure and function of the brain tissue and to develop new therapies for neurodegenerative diseases [5]. To create a 3D environment that supports the growth of neuronal cells a scaffold which acts as a physical structure and where the cells can attach and grow is needed. Various biomaterials can be used for such scaffold systems [40]. In general, the choice of scaffold stiffness is a crucial factor that can influence the neuronal growth and tissue development. In the case of 3D neuronal scaffolds, both stiff and flexible scaffolds have been investigated for their ability to support neuronal cell growth and function. Hydrogels, a water-swollen network of polymer chains which mimic the extracellular matrix (ECM) of the brain are mainly used as a flexible 3D environment for the cells. Such hydrogels can be specifically modified to incorporate various ECM proteins and peptides to promote cell growth. The soft mechanical properties of hydrogels provide a more compliant and flexible environment that furthermore mimic the softness and elasticity of the brain tissue. Nevertheless, one big disadvantage of flexible scaffolds is the random and uncontrolled distribution of the cell within the scaffold system [41]. To overcome this drawback stiff scaffolds can be used instead. Stiff scaffolds are typically composed of materials with high stiffness and mechanical strength, such as polymers with high young's moduli (GPa). These scaffolds provide a rigid structure which supports neuronal cell growth and controlled organization. With specifically tailoring the scaffold geometry they provide a guiding structure that can guide dendrite and axon growth in a controlled manner and thus allow for precise 3D network analysis. In addition to stiffness, other factors such as scaffold porosity, surface chemistry, and biodegradability can also influence cellular behavior and tissue development in 3D neuronal scaffolds. By carefully selecting and designing these parameters, it is possible to create scaffolds that can support the growth and function of neuronal cells in a 3D environment, and that can offer new opportunities for tissue engineering and regenerative medicine [41][8]. In this work 3D scaffolds and electrodes

are introduced which allow a deep analysis of tissues like organs on a chip, organoids etc. in all three dimensions and thus can lead to an improved tissue engineering.

2.2 Multi-Photon Polymerization

DLW by MPP has recently been demonstrated as an attractive method for fabricating precisely controlled micro size cell scaffolds for 3D neuronal tissue engineering [7][15]. It is a 3D printing technology, based on the photon absorption by photopolymers. Due to the non-linearity physics of the absorption process the fabrication of polymer structures with sub-100 *nm* resolution is possible [19]. The 3D structures used in this work are printed based on the two-photon absorption (TPA) process. TPA is defined as the simultaneous absorption of two photons (in the infrared range) of identical or different wavelengths to excite an electron of the photon initiator molecule from the ground to the excited state. This usually triggers the molecule to polymerize and change its material properties. The polymers used in this work are organic, negative-tone photoresists which get solidified once exposed to irradiation. This way, it is possible to separate the written structures from the unwritten part during the development step. The polymers consist of photoinitiators, monomers, cross-linkers and solvents to dissolve the individual components to have a liquid-based photoresist. The photoinitiators on the one hand absorb the incoming photons, get excited and generate active species like free radicals. These radicals interact with the monomers which are unsaturated molecules and make 90 percent of the photoresist material. The interaction leads to a polymerization reaction of the monomer which has an active termination on which a new monomer can bound (monomeric radicals). The resulting polymeric chain grows rapidly without any further supplementary photon excitation. During the propagation stage the length of the polymeric chain increases until the active termination reacts with a free radical or another active termination from a second chain which ends the growth of the chain reaction [42]. The bandgap between the unexcited and excited state of the photo initiator usually has double the energy of the laser wavelength. Therefore, to reach the excited state and overcome the bandgap energy an electron located in the ground state has to absorb two photons. As the so called quasi state in the middle of the bandgap has a very short lifetime the absorption has to be taken place almost simultaneously. Otherwise, the electron first absorbs one photon, gets excited to the quasi state and drops down into the ground state again before the necessary second

absorption process can take place. The higher the amount of photons per area which reaches the photosensitive polymer the higher the chance to absorb two photons in the desired time frame. The amount of photons per area is also called light intensity. Figure 2 illustrates the theory of TPA. The light intensity to excite the molecule is only high enough in the focus spot of the laser.

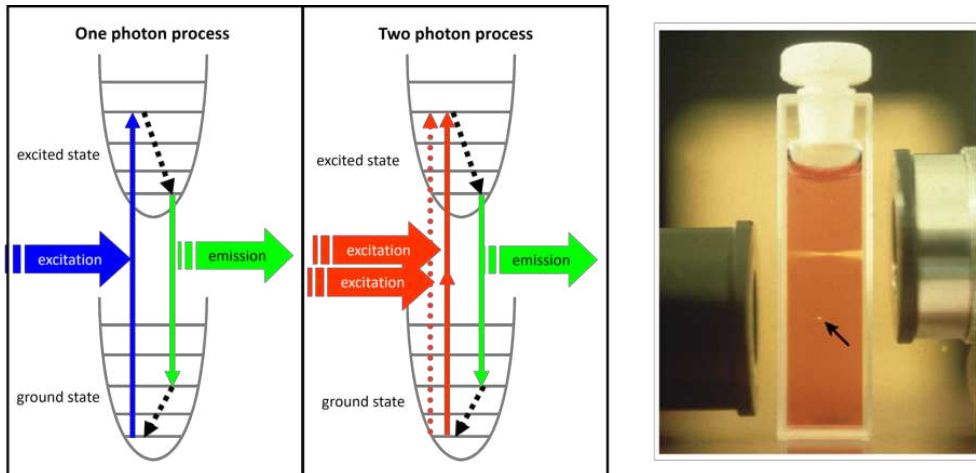


Fig. 2: Theory of one photon and two photon absorption process. The fluorescence indicates the high resolution of the two-photon process [43].

Thus, for simultaneous absorption the light intensity has to be higher than a specific threshold. This simultaneous absorption is a second-order process, which means that it is proportional to the square of the light intensity. The second order physics is the reason why it is possible to maintain complex 3D structure in the 100 *nm* range which is lower than the diffraction limit of the used wavelength. During the process the photoinitiator locally absorbs the high-energy laser light within a confocal volume. This leads to the mentioned polymerization reaction inside this confocal volume which is called voxel (3D pixel). However, the activated photoinitiator can also be deactivated through fluorescence, phosphorescence as well as initiator and radical quenching. Nevertheless, the quenching of the initiator can also be used as a method to prevent uncontrollable propagation of the polymerization. It can be achieved with dissolved oxygen or the addition of radical quenching compounds. This way it is possible to have a better control over the voxel size and thus voxel sizes even below 100 *nm* are possible [44]. During the movement of the laser focus, raster scanning as well as layer-by-layer writing, voxels are being printed next to voxels leading to the print of

the defined 3D polymeric structure. The cross linkers form covalent bonds between the polymer chains. The degree of polymerization of the monomers as well as the strength of the covalent bond between the polymers define the mechanical properties of the printed 3D structure. Thus, with adjusting the chemical formulation of the photoresist its mechanical properties can be tailored. In general an ideal photoresist for the two-photon polymerization should have four important characteristics. First, the photoinitiator needs to have a sufficient two-photon absorptivity near the excitation wavelength to trigger the photopolymerization. The photoresist has to cure rapidly within the confined laser focal spot to avoid overheating. Furthermore, it should be optically transparent in the wavelength spectrum of the used laser excitation to prevent irradiation blockage, generation of excess heat as well as absorption throughout the laser path. Finally, the mechanical properties of the polymerized and cross-linked polymer should be high enough so that the 3D print withstands the post print process like development and solvent washing [42].

In general, it is necessary to differentiate between the feature size and the resolution. The feature size is defined as the width and height of one printed voxel. This size is determined by the print solution set, thus objective, resin, laser wavelength etc. and can be less than 100 nm. The resolution on the other hand is defined as the minimum distance with which it is possible to print two voxels next to each other. This distance is determined by Abbe's criteria and thus depends on the wavelength and objective's numerical aperture. In addition, the so-called proximity effect of the polymerization further limits the resolution. The effect describes the unintended sub-threshold polymerization between neighboring lines written in close proximity causing undesired effects such as linewidth broadening. The mechanisms as well as the strength of the proximity effect are still not known in detail but can potentially range from polymer chain growth, scattering of light, thermal or molecular diffusion and dose addition during the different illumination steps. Next to the proximity effect also substrate reflection, temperature, and humidity each influence polymerization and thus should be considered [45]. The following equation (Equation (1)) describes the mathematics behind a multi-photon process.

$$P_{material} \propto LP_{avg}^n * t \quad (1)$$

In Equation (1) P is the absorption probability, LP the average laser power, n the number of absorbed photons (e.g. for two photon absorption $n=2$), and t the time of exposure. The so called iso-intensity surface which shows the intensity distribution around the focal spot of the laser beam in all planes in 3D, where the intensity is equal or above the threshold for polymerization defines the size and shape of the printed ellipsoidal voxel. This voxel is the smallest printable 3D volume which can be analogously seen as a 2D pixel. The closer the square of the excitation intensity is set to the polymerization threshold the smaller becomes the voxel size. The voxel size can be controlled with adjusting the dose in the focal spot. The dose is defined as the quantity of photons as a function of area and/or time. With using a pulsed laser the dose depends on many different parameters and thus becomes rather complex. The laser delivers a photon beam with a certain laser power which will be slightly reduced due to the optical components which shape and direct the beam through the objective lens [44]. The dose is then defined by the laser power and the scan speed at the objective lens (Equation (2)).

$$Dose = LP * time \quad (2)$$

The higher the laser energy, the higher the light intensity the more volume will reach the threshold. On the other hand, the less the scan speed, the longer the time the laser focus stays at one point and therefore the bigger the threshold volume.

For the actual printing process a femtosecond pulsed laser beam is precisely focused into the polymer and scans the desired geometry layer by layer and voxel by voxel. The laser pulses have a duration of $80 \text{ fs} - 100 \text{ fs}$ and are repeated at an 80 Hz rate. Due to the pulsed laser properties very high peak powers and thus high photon densities can be generated which are necessary for the TPP process. The complex solid structure is realized by overlapping the voxels (hatching) and overlapping the layers (slicing), thus enabling a truly additive fabrication process as it can be seen in Figure 3.

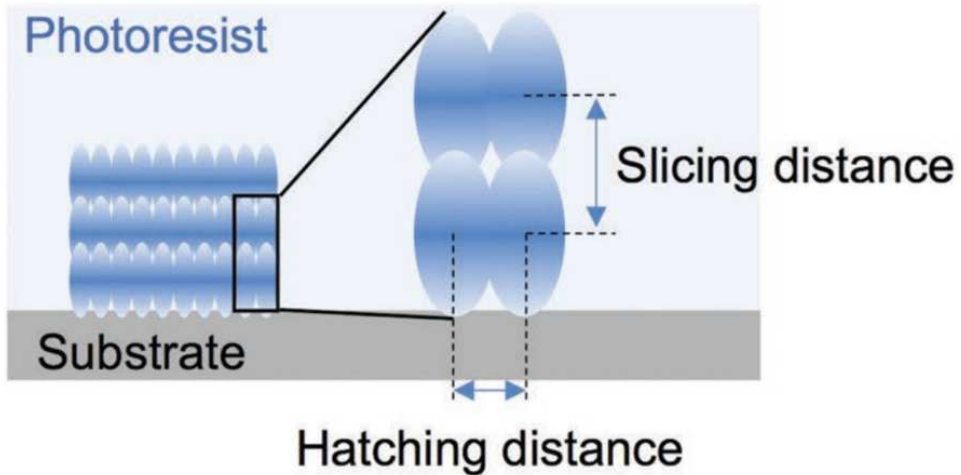


Fig. 3: Illustration of voxels being printed next to each other to realize the 3D geometry [18].

In contrast to the TPP process the very low feature sizes cannot be achieved with single photon absorption. The absorption of only one photon is much more likely and therefore this process is linearly proportional to the light intensity. This can also be seen in Equation (1) for $n=1$. Due to the first order physics the volume in which the necessary threshold for photon absorption is reached is much higher than for the two photon absorption process. Therefore, the polymer polymerized in the entire volume exposed to the laser beam. On the one hand this will drastically reduce the resolution and on the other hand does not allow printing complex 3D geometries [46].

As the laser beam triggers the polymerization at the wanted regions the properties of the polymer will slightly change. Especially a shrinkage of the polymer will occur during structuring and development. This might lead to a deformation and therefore limits the reproducibility of the fabricated structures. In the case of TPP shrinkage has not been fully understood. The amount of shrinkage in general strongly depends on the degree of polymerization and thus on resin type, printing parameters as well as the printed geometry. For negative tone resists (all the resists used in this work are negative tone resists) shrinkage occurs due to the reduction in volume induced by the polymerization reaction. The solidified material has a higher density than in liquid state [47]. In general shrinkage can occur during the writing process as well as during developing. During laser exposure the degree of polymerization is determined by the laser dose. The

higher the dose the lower the shrinkage. Nevertheless, the dose cannot be increased to far, as otherwise the resin will be burned away leading to micro bubbles [47]. During the development the dissolution of soluble components like unreacted initiators and unpolymerized monomers with the developer leads to further shrinkage. The amount of soluble components is lower for a higher degree of polymerization. In addition, a shorter development time can help to reduce shrinkage. Furthermore, a slight swelling in the structure occurs while development. Capillary effects during the drying process can then further lead to shrinkage. The drying process was determined to be the main contributor to shrinkage [47]. Usually, shrinkage is isotropic but depends on the geometry of the structure. The situation is different whether or not the structure is adhered to a substrate. If the size of the printed structures is really crucial for the application change in sizes due to shrinkage should be taken into account. The easiest way is to print test structures and determine the shrinkage in advance so it can be pre-compensated. Shrinkage can in general also be used to print structures smaller than the calculated recipe [47]. One big problem of shrinkage arises if structures have large contact areas with the substrate. In these cases, the structures cannot shrink isotropically due to the adhesion to the substrate and thus may curl up. As air is the medium with lower energy the system tends to minimize the contact area between structure and substrate to thermodynamically equilibrate to the state of minimum energy. The higher the relation of the surface area to the volume (thin and flat structures) the stronger the drive towards delamination. Activating the substrate (e.g. with oxygen plasma) might help to reduce the delamination, as it decreases the structure-to-substrate surface energy.

2.3 Electrochemical Deposition

2.3.1 Metal

Electrochemical deposition is a widely used method for depositing metals. An electric current will drive a chemical reaction resulting in the deposition of metal ions onto an electrode surface. A series of chemical reactions will take place at the electrode-electrolyte interface. While metal ions are being oxidized at the anode to form metal cations, at the cathode these cations are reduced to form metal atoms. The following reaction (3) represents the oxidation-reduction reaction.



In Reaction (3) Mn^+ represents a metal ion, ne^- represents the number of electrons required to reduce the ion, and M represents the deposited metal. As some metals (base metals such as zinc) releasing their valence electrons and form solvated ions more easily than others (noble metals) when coming in contact with a solution, the formed double layer potential also strongly differs. It is impossible to determine the potential of a single interface without a reference point. Therefore, the interface potentials for different metal electrodes in solution containing their ions in $1 \frac{mol}{l}$ concentration have been measured against the potential of the standard hydrogen electrode (SHE) which is defined as 0. The measured potential is called standard potential. The SHE consists of a platinum electrode that is bathed in hydrogen gas at a pressure of 101.3 kPa . The electrode is furthermore submerged in a solution with an H^+ activity $a(H^+) = 1$. All standard potentials are reported with respect to the reduction reaction of the SHE [48]. Each metal-solution (containing the ions of the metal) combination forms a half cell with its own characteristic potential. Each pair of reduced and corresponding oxidized species is called redox pair. Redox pairs with lower standard potentials act as reducing agents for redox pairs with higher standard potentials. To avoid the competing reaction of oxidation or reduction of water in aqueous solutions the potential region between -0.828 V and 1.229 V called water window is important. Within this window water is stable both against reduction and oxidation. For potentials higher than 1.229 V water is oxidized to oxygen ions, whereas it is reduced to hydrogen and hydrogen ions below -0.828 V [49]. For the electrodeposition of metals an electrolytic cell is used. It contains two redox pairs which are connected. In an electrolytic cell an external voltage leads to the reduction of one of the metals to its elemental state while the other metal is oxidized to form metal ions. The minimum potential which is needed to start the reaction can be calculated from the difference in their standard potentials (Equation (4)).

$$\Delta E = E_0^{Reduction} - E_0^{Oxidation} \quad (4)$$

If the reaction is not taken place under standard conditions the Nernst Equation needs to be used for the calculation of the potential based on the difference in standard potential and the activity a of the reactants. By definition the activity of solids is 1 [49] leading to Equation (5).

$$\Delta E = \Delta E_0 - \frac{RT}{zF} * \ln \frac{a^x(X) * a^y(Y)}{a^b(B) * a^g(G)} \quad (5)$$

In Equation (5) ΔE is the difference in standard potential, R the gas constant, T the temperature, z the amount of charge and F the faraday constant. The Nernst equation is only valid if the reaction is at equilibrium. Instead of using SHE as a reference electrode, for practical applications metal electrodes are used and therefore the Nernst equation can be simplified to Equation (6).

$$E = \Delta E_0 - \frac{RT}{zF} * \ln[A^{Z-}] \quad (6)$$

The potential of the overall reaction only depends on the activity of the anion A^{Z-} . The Ag/AgCl electrode is a common example for such a reference electrode. Ag is covered with a insoluble AgCl layer and immersed in a Cl^- containing solution. Once saturation of Cl^- is reached the Ag/AgCl electrode has a potential of 0.197 V vs. SHE [50]. To determine the potential at which a reaction occurs accurately a stable reference potential is needed as the acting electrochemical driving force will influence the potential of the electrodes themselves. Therefore, for electrochemical reaction a three-electrode setup is applied. The reference electrode is connected in parallel to the working electrode. It has a very high ohmic resistance and thus stays at a stable reference point. The current flows between working and counter electrode. Figure 4 illustrates the used circuit.

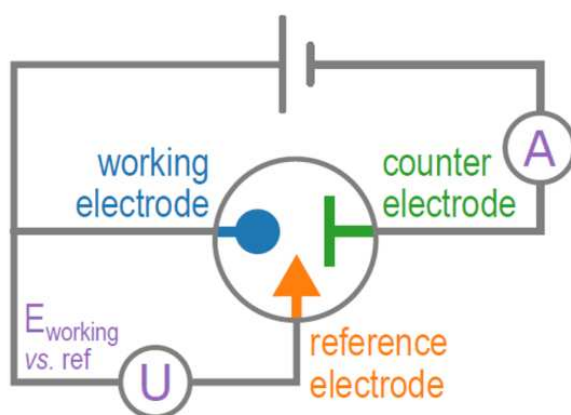
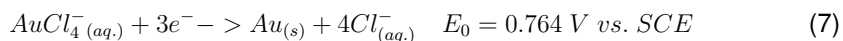


Fig. 4: Illustration of the electrical circuit of a three electrode arrangement [51].

The kinetics of the electrochemical reaction depend on a variety of factors, including the applied voltage or current, the concentration of metal ions in the electrolyte, and the

composition and properties of the electrode and electrolyte. During the process metal atoms will nucleate and grow on the electrode surface, where nucleation refers to the initial formation of metal atoms and/or clusters while growth refers to the increase in size and thickness of the deposited layer. Adding surfactants or other additives to the electrolyte will influence the size, shape, and orientation of the deposited metal clusters. By adjusting the deposition parameters like temperature, voltage, time, properties of the electrode and electrolyte and many more the film thickness, grain size and texture can be controlled [50].

In this work the template assisted electrodeposition of gold (Au) is used to create 3D electrodes. Au is used as electrodes due to its high electrical conductivity. The choice of an appropriate Au solution is very important for the successful electrodeposition of Au. One big challenge is the fact that Au^+ is highly unstable in aqueous solution. While for industrial applications the gold(I)cyanide complex $Au(CN)_2$ is most often used due to its high stability [51] in this work the 3D Au electrodes are deposited using the gold chloride ($HAuCl_4$) complex due to its lower health risk. The redox reaction can be seen in equation Equation (7) [52].



In Equation (7) the potential is specified against the SCE (0.238 V vs. SHE) [52].

By varying the applied potential of the deposition the growth behavior of the electrodes can be strongly manipulated. An applied voltage which is different from the standard potential of the chemical reaction is called overpotential [49]. When using low overpotentials the growth takes place at existing seeds resulting in sharp, dendrite like deposits. The same spiky deposition is achieved when applying very high overpotentials which leads to a depletion of Au ions close to the cathode due to diffusion limitations [50].

2.3.2 Polymer

Electrical, mechanical and biological properties of conductive polymers (CP) can be varied in a wide range by doping the conjugated bonds of the polymer [53]. Thus, it is possible to customize CPs for specific applications. With introducing (n-doping) or removing (p-doping) delocalized electrons of the double bonds it is possible to obtain conductivity values similar to semiconductors (10^{-6} S/m to 10^{-2} S/m) [54]. Although they have lower conductivities than metals CPs can have very low impedance values

and high charge storage capacity (CSC) and charge injection capacity (CIC) because their chemical structures enable both electronic and ionic charge transport in the entire polymer volume [55]. Furthermore, the higher surface roughness and porosity leads to a superior active electrode area compared to metals. At electrode/electrolyte interfaces the capacitance mainly depends on the surface area. However, for CPs the capacitance scales with the volume [56]. Due to their soft mechanical properties CPs are ideal candidates to reduce the mechanical mismatch between electrode and biological tissue when combined with flexible substrate materials. This will lead to an improvement of chronic in-vivo stability of neural implants. In this work the gold electrodes are coated with poly 3,4-ethylenedioxythiophene (PEDOT) doped with poly(styrenesulfonate) (PSS) to improve their electrical properties via an electrochemical polymerization process. PEDOT:PSS is used because of its outstanding electrochemical properties and stability [57]. EDOT in aqueous solution with poly(sodium 4-styrenesulfonate) (NaPSS) is polymerized by applying an electrical bias. The monomer is oxidized, and high order oligomers are stabilized by the polyanion NaPSS. Electrochemical deposited PEDOT:PSS appear in globular or cauliflower-like morphologies [57]. Conductivity and morphology can be controlled with adjusting the deposition parameters and thus the polymerization.

2.4 Cell-Electrode-Interface

2.4.1 Cell Potential

A biological membrane is made of a lipid bilayer containing two phospholipid molecules with a hydrophilic head and a hydrophobic tail each. The tails are oriented towards each other while the heads are oriented towards the inside and the outside of the cell. This results in a very large transmembrane resistance as the membrane forms a barrier against ion and charged molecules diffusion. Specific voltage gated ion channels and transporters inside the lipid bilayer allow controlled transmembrane ion transport and thus create a wanted net current flow by hydrolysis of adenosine triphosphate. This leads to different ion concentration outside and inside the cell resulting in a potential imbalance which forces the channels to open and an exchange of ions with the surrounding takes place. The change in ion distribution and concentration enables the creation and propagation of an electrical signal which is called action potential (AP). The two main ion species which are responsible for cell activities are potassium (K) and sodium (Na).

The concentration of potassium ions is higher inside the cell while the concentration of sodium ions are more prominent outside of the cell. Due to different concentrations a diffusion force is build up which leads to a flow of positively charged potassium ions out of the cell through the membrane. As negative ions like chloride (outside the cell) and proteins (inside the cell) are too big and cannot pass the membrane, a negative charge is built up inside the cell which leads to a potential difference and thus to an electric force which is increasing with ongoing diffusion. At some point the electric force compensate the diffusion force and no more ions are moving [43] anymore. The cell is in resting state with an equilibrium potential of a certain ion type which can be defined by the Nernst equation (8):

$$E_i = \frac{RT}{zF} * \ln \frac{i^{interior}}{i^{exterior}} \quad (8)$$

In Equation (8) R is the gas constant, z the number of electrons, F the Faraday constant, T the temperature and $[i]$ the concentration of ion species. The cell membrane can be seen as a capacitor and the sodium and potassium exchangers as a resistor with variable resistivity to the ion flow. Thus, with using the Nernst equation and by considering a relative permittivity of each ion type depending on the ion concentrations the membrane potential can be calculated with the Goldman equation (9).

$$\Phi = \frac{RT}{F} * \ln \frac{P_{Na}[Na^+]_{out} + P_K[K^+]_{out} + P_{Cl}[Cl^-]_{in}}{P_{Na}[Na^+]_{in} + P_K[K^+]_{in} + P_{Cl}[Cl^-]_{out}} \quad (9)$$

In Equation (9) P is the permeability of the ion through the membrane at the extra-cellular concentration *out* and the intracellular concentration *in*. The extracellular and intracellular electrolytes do have different ionic concentration and thus a Φ not equal 0 is established. At the equilibrium state, ion diffusion, pumping leakage and other interactions leads to a resting potential of the cell. Several stimuli such as temperature, mechanical stress, ligand binding or the membrane potential can lead to a change in permeability of the ions through the membrane. The resulting flow of ions across the membrane will change the membrane potential from its resting potential. The change can either be positive (depolarization) or negative (hyperpolarization) and will trigger voltage gated channels to be activated once a threshold is reached. Potassium has the highest permeability at equilibrium and therefore the resting potential is mainly defined by the equilibrium potential of potassium ions. Mechanical, thermal, electrical, and

chemical stimuli may open the channels and lead to positive and negative potential inputs into the cell. Such a stimulus may allow an inward flow of negative sodium ions due to opened channels forced by the negative equilibrium potential inside the cell. A certain threshold (typically around -50 mV) triggers much more voltage gated sodium channels to open fast allowing for an increased influx of Na^+ ions [58]. The process proceeds until all available ion channels are open which leads to a depolarization with a positive Nernst potential of Na^+ of 60 mV . The resulting membrane potential can reach up to 40 mV and more [58]. The change in the membrane polarity due to the high flux of sodium ions inactivates the sodium channels at some point. While sodium ions can therefore no longer enter the cells, transmembrane potassium channels are activated leading to an outward current of potassium ions forced by the positive cell potential. The repolarization of the cell potential below the resting potential can be observed due to the relatively slow kinetics of the inactivated sodium channels compared to the potassium channels (hyperpolarization) which need a few ms to recover. The time until ion pumps ensure the relaxation of the potential to the resting state is called refractory period. No further AP can be propagated during this period which is the reason for unidirectional signal propagation as channels which just passed the signal cannot be activated again immediately. The whole AP process for neurons lasts for less than 5 ms and is illustrated in Figure 5.

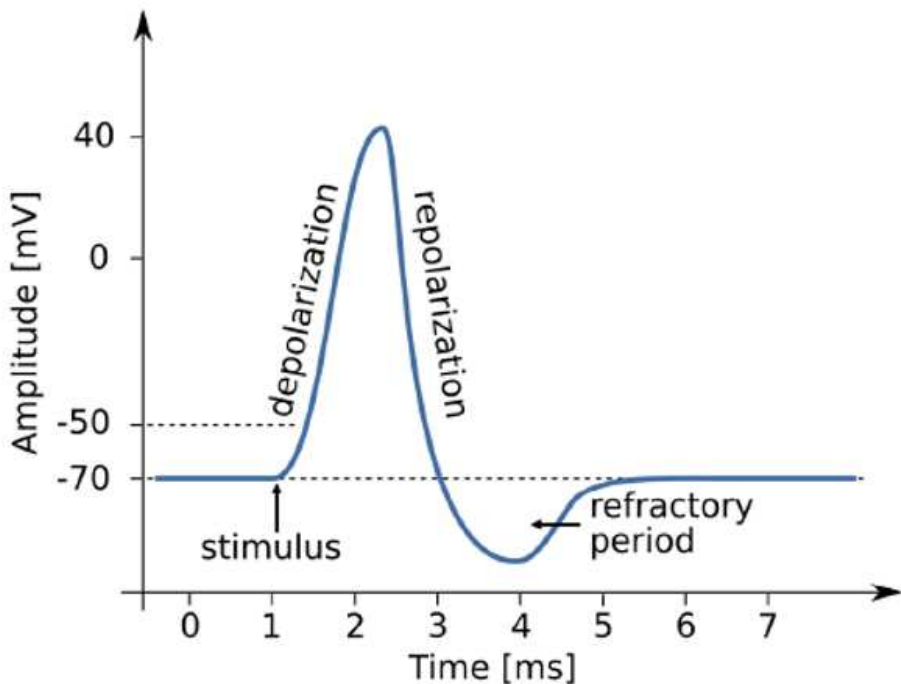


Fig. 5: Illustration of a typical action potential stimulus. Important parts are indicated [59].

2.4.2 Neuron

The basic working units of the brain are the neurons. Neurons are cells within the nervous system and communicate with each other using a specialized cell design to transmit information to neighboring cells. They are responsible for receiving sensory input from the external world as well as controlling all our motor commands. Neurons consists of a soma (cell body) containing the nucleus and cytoplasm, an axon extending from the cell body and transmitting the signal, and multiple dendrites receiving messages from connected neurons. The contact points between neurons at the end of dendrites are called synapses. Most of the protein synthesis occurs in the soma. While the dendrites usually spread in branches only a few μm from the soma the axon can extrude up to meters long [60]. In mammalian brains between 100 million and 100 billion neurons form a dense and complex 3D network. Connected neurons communicate with each other via electrical impulses called action potential (AP) which are transmitted along

their axons and which were explained further above. Usually, the axons are covered with a myelin sheath. This sheath is made by specialized cells called glia cells and accelerates the transmission of the signal [60]. Figure 6 shows the schematic of a neuron.

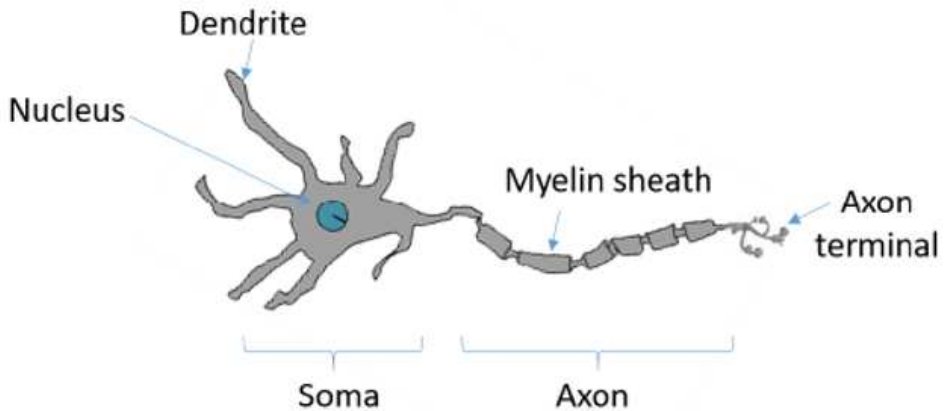


Fig. 6: Schematic of a neuron. Important parts of the cell are indicated [61].

2.4.3 Electrode-Electrolyte Interface

To be able to analyze the recorded signal of a neuron it is necessary to have an idea about the path way the electric signal will travel from the cell where it gets created to the electronic chip where it gets measured. As the electrode of an extracellular measuring device like the MEA is always in contact with an electrolyte which is between the cell and the chip it is important to understand what happens exactly at the electrode electrolyte interface. The electrode is made out of an electronic conductor like metals. In contrast the electrolyte is an ionic conductor and consists of the two main ion species for cell activities, potassium and sodium as well as polar water molecules. If both parts come into contact these water molecules and charge carrying atoms (counter ions) form interfacing layers at the interface due to excess charge formed at the electrode surface (charge determining ions). The concentration of counter ions decreases with increasing distance to the electrode. Much research has been done in the past hundred years trying to explain the phenomena at the electrode-electrolyte interface. One of the first approach was given 1879 by Helmholtz. He described the interface as an adsorbed layer of H_2O molecules and a layer of solvated ions in the electrolyte close

to the electrode surface attracted by surface charges of the metal. As he did not take diffusion processes into account (zero temperature) this so called ‘‘Helmholtz layer’’ described a rigid layer with no movement of the separated charges [62]. The charge separation can also be described as an electronic capacitance by Equation (10).

$$C_H = \frac{\epsilon_0 * \epsilon_r}{d} \quad (10)$$

In Equation (10) d is the distance between the metal surface and the ion layer, ϵ_0 is the relative permittivity and ϵ_r is the vacuum permittivity.

Due to the temperature none zero diffusion processes have to be taken into account which lead to a change in concentration of ions. The first try to introduce diffusion phenomena was done by Gouy and Chapman. With combining the Maxwell-Boltzmann statistics with the Poisson-Boltzmann equation they include the density of charged ions depending on the distance to the electrode surface, the kinetic energy and the relation between charge per volume and potential at distance x with which the potential can be expressed. The model leads to an increase in concentration of charge determining ions with increasing distance from the electrode surface. This results in an inhomogeneous distribution of ions which is called diffusive layer (Gouy-Chapman layer). The capacitance of the additional layer can be calculated with differentiating the potential difference over the surface-charge density and can be expressed as follows (Equation (11)):

$$C_G = \left(\frac{2z^2 * e^2 * \epsilon_0 * \epsilon_r * n^0}{kt} \right)^{\frac{1}{2}} * \cosh \frac{z * e * \Phi_0}{2k_b T} \quad (11)$$

In Equation (11) T is the temperature, n^0 is the bulk ion concentration in the electrolyte, e the basic charge of an electron, z the ion charge, k_b the Boltzmann constant, and Φ_0 the surface potential.

The additional layer will lead to a change in the formula of the capacitance. The distance d now depends on the electrolyte concentration and the potential applied to the electrode. A higher potential as well as a higher concentration of the electrolyte result in a decrease in double layer thickness and thus in an increase in capacitance (smaller d). With a higher concentration of the electrolyte the amount of counter ions per volume increases. Therefore, less volume of electrolyte is necessary to compensate the excess surface charge resulting in a decrease in double layer thickness. Figure 7 illustrates the interface between an electrode and an electrolyte.

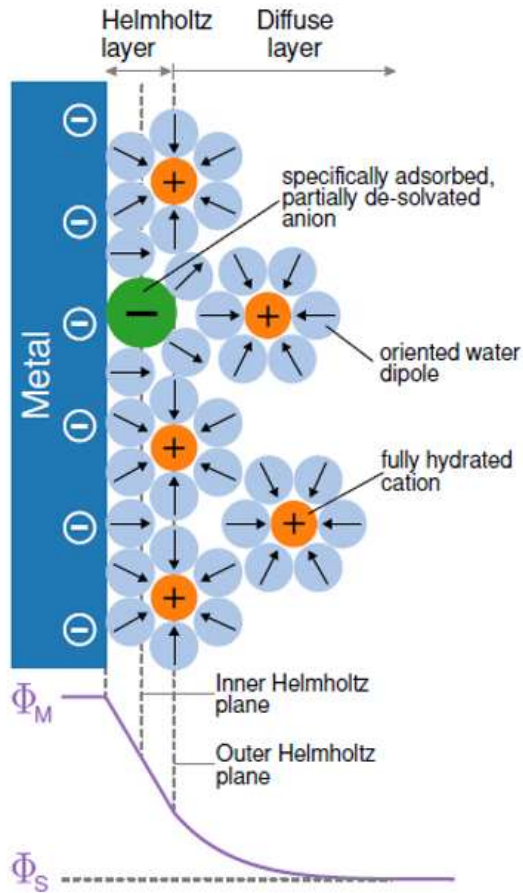


Fig. 7: Illustration of a typical interface between the electrode and the electrolyte. Important parts are indicated [51].

Gouy and Chapman considered the charges as point charges without an ionic radius. The ions can then approach the interface indefinitely close which quickly results in an infinity potential and thus infinite capacitance at higher ion concentrations. To overcome this drawback of the model, Stern combined the adsorbed rigid Helmholtz layer with the diffusive Gouy-Chapman layer. The capacitance of the so called Gouy-Chapman-Stern model can be expressed by the serial combination of the two layers (Equation (12)).

$$\frac{1}{C_S} = \frac{1}{C_H} + \frac{1}{C_G} \quad (12)$$

To simplify the interactions occurring at the electrode-electrolyte interface a so-called

Randles Cell model is used which is illustrated in Figure 8.

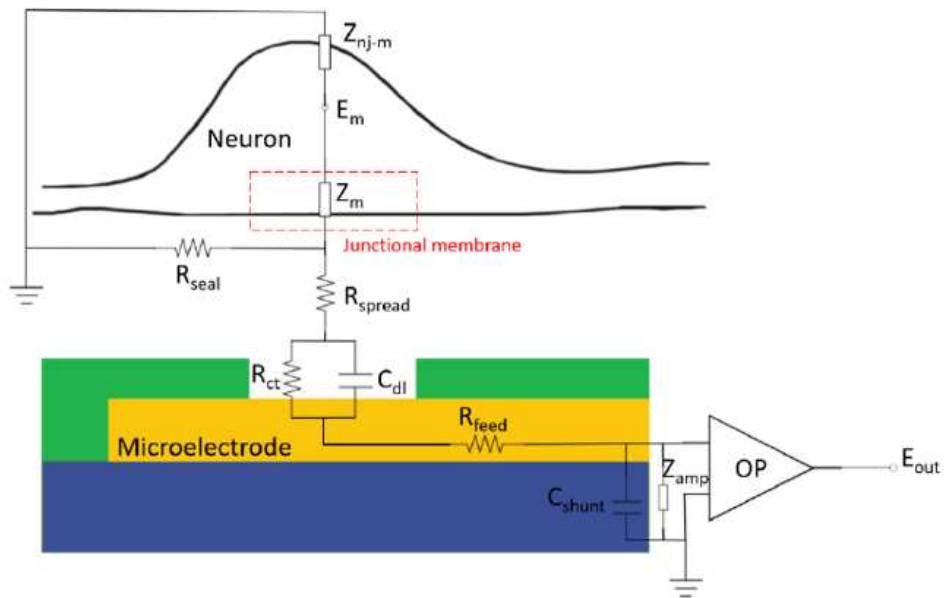


Fig. 8: Illustration of the electrical equivalent circuit at the interface between cell and electrode. The simplified Randles Cell model is applied [63].

Next to the described double layer capacitance C_S a charge transfer resistance R_{ct} in parallel and a solution resistance R_{spread} in series have to be added. R_{ct} is also called polarization resistance and describes the resistance for charges to travel between electrode and electrolyte. As the current has to pass through the electrolyte the solution resistance has to be taken into account. R_{spread} is defined as the spreading out of the current into the solution which leads to an ohmic drop concentrating near the electrode. This Randles point contact model is widely used to describe the neuron-electrode interface consisting of the electrode, the neuron and a cleft between them filled with an electrolyte. Using the contact model, it is important to distinguish between the non-junctional membrane (no contact with the electrode) and the junctional membrane (contact with the electrode). As mentioned, the electrode in an electrode-electrolyte interface can be electrically described as a capacitance C_{dl} parallel to a resistor R_{ct} . When the ion channels open during an AP process, ions will flow across the membrane and have to pass the cleft to reach the electrode to be measured. Part of the cell current leaves the cell through the free membrane and the electrolyte resistance without being recorded by the electrode. The existing cleft between the cell and the electrode provides

a second part for the current to leave the cell without being detected (R_{seal}). Losses due to those currents and the capacitive coupling at the electrode-electrolyte interface leads to a decrease in action potential recording qualities. As a result, to monitor some smaller features like sub-threshold potentials a very high coupling between the electrode and the cell as well as high quality electrodes are necessary. A larger R_{seal} leads to an increase in coupling behavior between cell and electrode and thus to an increased signal quality (high signal-to-noise ratio (SNR)). Depending on the electrode material as well as geometry the cleft thickness typically ranges between 150 nm and 40 nm which leads to an R_{seal} of several 100 kOhm up to GOhm respectively [64].

2.4.4 Impedance

To characterize the electrode-electrolyte interface electrochemical impedance spectroscopy (EIS) can be used. As the device is fabricated to measure electrical stimuli from cells, like the AP, and these stimuli have changing potential values the alternate current (AC) behavior of the interface is from interest. In direct current (DC) situations it is enough to have a look at the value of the resistance R to characterize the interface. For a DC case the “resistance” of the capacitor is infinite. Thus, once the capacitor is charged to the set potential, the current will only flow through the polarization resistance R_{ct} . The amount of charges to be stored at the capacitor to reach the set potential depends on its geometric feature like area and distance of the double layer at the electrode-electrolyte interface. The proportional value between the potential and the amount of charges is called capacity C [65][49]. The situation drastically increased in complexity when using an AC. While the resistance R_{ct} and R_{spread} are independent from the frequency of the potential, the resistance of the capacitor decreases lineally with increasing frequency. To understand this behavior in AC conditions a new value Z must be introduced. Z is a vector describing the impedance of the system and contains both, the normal resistance (as in DC case) and the reactance as scalar values. The resistance electrons experience traveling among the atoms in a material is observed in AC and DC and is described by the value R . The reactance on the other hand describes how a system stores and releases energy. This happens because of fluctuating currents and voltages. Thus, the reactance is only observed in AC conditions and expressed in imaginary numbers. In case of a capacitor, where the energy is stored and released in form of an electric field the reactance Z_c shows a capacitive behavior. In this case

the current has a phase shift of 90° with respect to the voltage. While at the beginning the voltage at the capacitor is zero and the current for charging the capacitor is at its maximum, during the charging process the voltage at the capacitor increases and thus the current decreases. In the situation the capacitor is fully charged the voltage is at its maximum while the current is zero [65][49]. For frequencies approaching zero (DC case) the resistance of the capacitor is infinite and the total impedance is determined by the sum of the two resistances (R_{spread} and R_{ct}). The higher the frequency the lower the resistance of the capacitor and thus the lower the total impedance. It can be imagined as a more and more easy way for the electrons to “pass” the capacitor instead of flowing through the parallel resistor. For high frequencies the resistance of the capacitor is approaching zero. Thus, the parallel resistor does not play any role anymore and the total impedance is only determined by R_{spread} . The drop in impedance for higher frequencies therefore only depends on the properties of the capacitor, in particular on its capacitance C which determines the amount of charges and thus the amount of energy which can be stored. The capacitance depends on the geometrical sizes of the capacitor which in case of electrolyte-electrode interface (like in a MEA measurement) is the surface area of the electrode opening. The bigger the electrode surface in contact with the electrolyte the lower the impedance. Thus, higher electrode openings will lead to lower impedances of the chip. The impedance of the system can be calculated with applying an AC potential and measuring the current response. To reduce complexity of the situation a linear system is assumed, where a sinusoidal potential E_t leads to a sinusoidal current I_t with the same frequency but shifted in phase (as explained above). In this case, a DC situation can be thought of as an impedance with zero phase angle [65][49]. With using Ohm’s law the impedance can be calculated as follows (Equation (13))

$$Z = \frac{E_t}{I_t} = \frac{E_0 * \sin \omega t}{I_0 * \sin \omega t + \Phi} = Z_0 * \frac{\sin \omega t}{\sin \omega t + \Phi} \quad (13)$$

In Equation (13) E_0 is the applied potential, I_0 the flowing current, ω the frequency, t the time, and Φ the phase shift. The value of the impedance of a MEA chip determines the quality of the recorded signals, in particular with increasing impedance, the SNR will decrease.

2.5 3D Tissue

2.5.1 The Brain

The brain is a very complex organ. It contains of many different structures with unique roles in regulating various physiological and psychological processes. To fully understand the brain the role of each single structure has to be investigated. The outermost layer of the brain, the cerebral cortex, is responsible for many of the higher cognitive functions, such as perception, language, and decision-making. The cortex itself is divided into different regions specialized on different types of processing. The visual cortex for instant is responsible for processing visual information. On the other hand, the prefrontal cortex is involved in decision-making and planning. The cerebellum is located at the base of the brain and coordinates movement and balance with using small neurons called Purkinje cells. Another key structure which is located at the base of the brain is called brainstem. It sits just above the spinal cord and regulates many basic functions including breathing, heart rate and blood pressure. The limbic system in the center of the brain is responsible for regulating emotions and motivation and includes for instant the hippocampus with its function to form and retrieve memories [66]. One theory in brain research is the idea of neural plasticity which describes the brain's ability to change and adapt over time due to experiences and environmental factors. In this regard practicing a skill for example can lead to structural changes as neural connections are strengthened and new pathways are formed. Furthermore, it is important to study the way in which the brain interacts with the body and the environment like sensory information such as sight, sound and touch [67].

2.5.2 The Retina

The retina is a complex neural tissue located at the back of the eye. It is responsible for converting light into neural signals which are processed and transmitted to the brain. It is a thin layer of tissue and contains several layers of cells such as photoreceptors, bipolar cells and ganglion cells with output cells that transmit the information to the brain. The photoreceptors are located in the outermost layer of the retina and are responsible for detecting and converting incoming light into electrical signals. It can be distinguished between cones and rods. While rods are the majority and are responsible for vision in low light conditions, cones are responsible for color vision and are located in the central region of the retina (fovea). The photoreceptor cells are arranged in a specific

pattern that allows them to detect orientation, movement and contrast of visual stimuli [68]. Figure 9 illustrates the schematic of the eye and the retina.

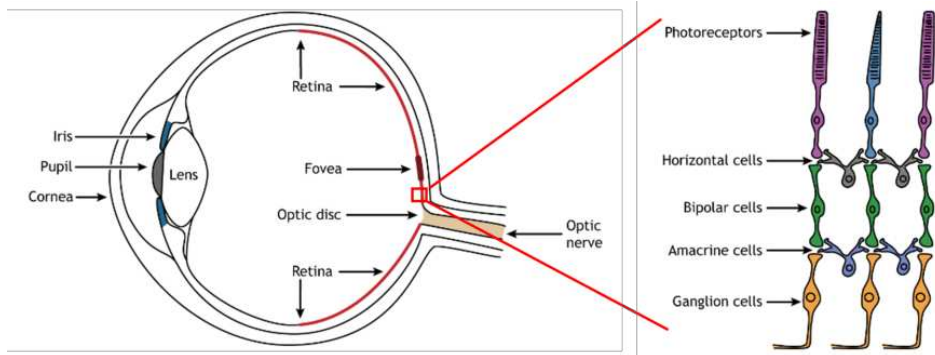


Fig. 9: Overall structure of the eye. The retina consists of several layers with different cell types [69].

For the processing of the visual information complex interactions between the different cell types are needed. In general, the electrical signal travels from the photoreceptor cells to the bipolar cells further to the ganglion cells and finally are transmitted to the brain via the optic nerve. The optic nerve is located at the center of the retina and appears at a round optic disc without any photoreceptors and thus creates a blind spot in the visual field. The transmission of the AP is modulated by neurotransmitters like glutamate, which is released by photoreceptors and bipolar cells. These bipolar cells sit between the photoreceptors and the ganglion cells and act as intermediaries. They receive the signals from the photoreceptors process them and transmit them to the ganglion cells. This processing is highly complex and a series of synaptic interactions between different cell types are involved. Interneurons like horizontal and amacrine cells contribute to the spatial and temporal processing with modulating the synaptic interactions. The photoreceptor cells can adapt to changes in light conditions with changing their sensitivity to light. This allows the retina to function in a wide range of lighting conditions, from bright sunlight to dim moonlight. Photoreceptor cells themselves do not fire AP but respond to light changes in releasing different amounts of glutamate onto the bipolar cells. This release is triggered by the graded receptor potential along the photoreceptor cells. They hyperpolarize in light and depolarize in dark. A hyperpolarization will lead to less glutamate being released [70]. In general two main types of bipolar cells can be distinguished in the retina. They respond in opposite

way to the glutamate coming from the photoreceptor cells. The “ON” cells are being activated when the light level increases and thus most active in bright conditions with less glutamate being released by photoreceptor cells. “OFF” cells on the other hand are being activated when the light level decreases (glutamate level increases) and therefore are most active in dim conditions. The ON-OFF response leads to a strong visual signal and allows the retina to detect changes in light levels and contrast. ON and Off bipolar cells are connected to ON-center and OFF-center ganglion cells, respectively. Only the ganglion cells send information out of the retina to the brain and thus are the only cell type capable of firing AP. A light stimulus will cause OFF-center ganglion cells to decrease their firing rate and ON-center cells to increase the rate [70].

2.6 Neuronal Implants

Neuronal implants have the goal of restoring lost or impaired sensory or motor function. They interface with the nervous system of the body and thus the biocompatibility of these implants is a critical factor. It determines how well the implant interact with the tissue and therefore how it performs over time. A variety of materials including metals, polymers and ceramics can be used. The materials should be chosen carefully to fulfill all the high standards and requirements of a neural implant. In general, the implant should not cause inflammation in the surrounding tissue. It should be mechanically compliant so it will bend and flex with the movement of the tissue without causing damage. Finally, it should not be toxic and cause any damage or degradation to the tissue. Each neuronal implant has to be designed according to the targeted tissue. For the use in the retina for example the implant must be able to deliver electrical stimulation to the tissue without damaging it. On the other hand, brain implants directly interface with the brain allowing for the recording and stimulation of neural activity [71].

2.6.1 Brain Implants

Brain implants are bioelectrical devices which are implanted into the brain with the aim of restoring and enhancing neural functions. Their aim is to help with treatments of a wide range of neurological disorders, such as Parkinson’s disease, epilepsy and spinal cord injuries. Both, recording implants as well as stimulation implants are existing. Recording implants, or neural prostheses, are used to record neural activity form the brain and typically consists of electrode arrays. These arrays are implanted into specific brain regions of interest. With decoding the recorded electrical signals external devices

like computers can be controlled. Those brain-computer interfaces allow individuals to interact with computers with only using their thoughts or brain activities. The implant can detect people's intention to move which allows individuals with paralysis to control a robotic arm. Furthermore, recording brain activities in different regions of the brain lead to a better understanding of how information is processed and represented in the brain [3][5]. On the other hand, stimulation implants are used to stimulate neural activity. They are usually used to treat diseases like Parkinson's disease where a stimulation of specific brain regions can help to reactivate neurons and thus alleviate symptoms. For instant, electrodes of deep brain stimulation implants are placed into specific regions of the brain to regulate abnormal patterns of activities to reduce the symptoms of neurological disorders [3][5].

2.6.2 Retina Implants

Retina implants are implanted into the retina to restore vision of people with certain types of blindness. They are electrical devices and stimulate the remaining viable retinal cells to create visual perceptions. In doing so they have the potential to improve the visual perception of people with severe vision loss due to diseases like retinitis pigmentosa and age-related macular degeneration. For that, they can replace the photoreceptor layer which is damaged with electrically stimulate the remaining underlying retinal cells to generate visual signals which are transmitted to the brain. When designing retinal implants, it is very important that the electrical stimulation is delivered to the correct retinal cells as the retina has different types of retinal cells with different sensitivities to electrical stimulation. The retinal implant has to be biocompatible and designed in such a way to minimize the risk of inflammation. Furthermore, it has to be long term stable and does not move or shift over time. The design, the number and location of the electrodes as well as their electrical properties is crucial and determines the efficacy of the implant [72].

2.7 3D Electrodes

The MEA is a chip based device for extracellular (outside) cell recording. Unlike intracellular recordings like the Patch Clamp technique which penetrate the cell membrane for better cell-electrode coupling (and thus better signal qualities) MEAs are non-invasive and capable for long-term recordings. The MEA consists of a multiple electrodes which are passivated by a dielectric material. Feedlines connect the outer bond pads with

which the chip can be connected to the recording device with the center of the electrode areas. The ionic current generated by a neuron during an AP is capacitively coupled to the MEA electrodes and thus to the recording device. Figure 10 illustrates the schematic of a 2D MEA chip.

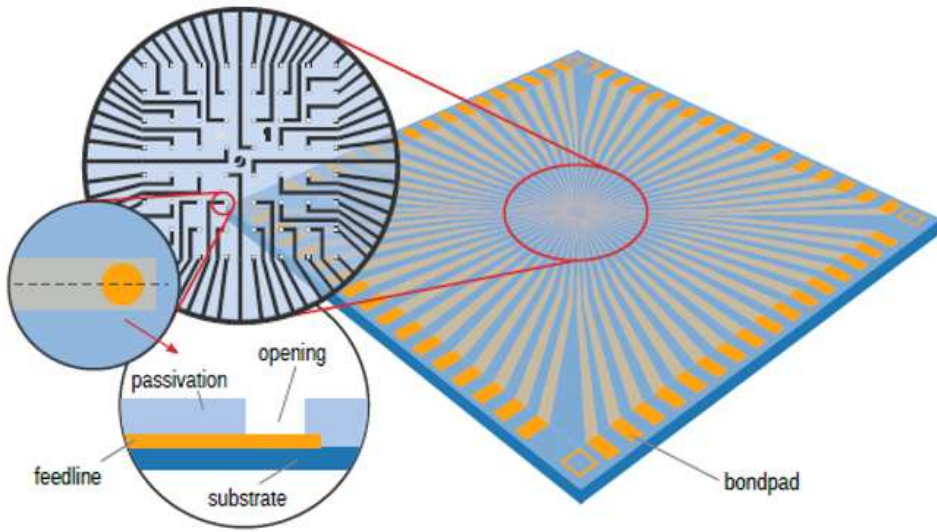


Fig. 10: Schematic of a typical 2D multi electrode chip with electrode openings in the center of the chip [51].

One drawback of the MEA chip is its two-dimensionality. Two-dimensional neural implants are limited in precisely target specific regions of the tissue which leads to unreliable recordings and stimulations. To overcome the challenge a MEA with three-dimensional electrodes is needed. In this regard 3D devices are a promising technology for improving the functionality of neural implants. They can provide a more stable and tighter interface with the tissue leading to better performance in treatment of neurological disorders as well as better understanding of the brain function [5]. The design of a 3D implant can be adjusted to fit the unique shape of each patient's neural tissue which results in more effective treatments. Additionally, by having multiple electrodes with different heights it is possible to record tissue activities from multiple regions of for instant the brain simultaneously which provides a more comprehensive picture and lead to a better understanding of how the brain works [6]. New technologies like 3D printing and advanced microfabrication techniques allow to fabricate highly customized 3D neural implants. Those implants are tailored to the unique needs of each patient

and can be optimized for specific applications.

This work introduces a new platform to fabricate fully customizable real 3D microelectrode arrays and implants using template assisted electrochemical deposition. The templates are fabricated using a TPP 3D printer. The 3D implants are used to record neuronal activities in 3D tissues like retina and brain ex-vivo. With further adding 3D scaffolds the 3D electrodes can also be used to record signals in highly controlled in-vitro three-dimensional neuronal networks to investigate signal propagation in 3D and to perform precise network analysis.

3 Materials and Methods

3.1 Microfabrication of Microelectrode Arrays

3.1.1 2D stiff MEA

The electrodes are technically openings of 10 μm or 6 μm in the passivation layer. This layer is located on top of the feedlines which guide the current from the electrodes to the edges of the chip where the so-called bondpads are located. These bondpads are non-passivated metal pads which ensure the ability to contact the electrodes to external electronics. The dimension of the entire chip is 24 mm x 24 mm. The whole fabrication process of the used MEAs take place in the ISO certified HNF cleanroom facility at the research center Jülich. First, the quartz substrates were cleaned with Acetone and Isopropanol (IPA) and then baked at 150 °C for 5 min on a direct contact hot plate. To define the metal contact pads, feedlines, and electrodes the photoresist LOR 3B (MicroChemicals GmbH, Germany) was spin-coated on the cleaned quartz substrate at 3000 rpm for 45 s with a ramp of 500 $\frac{\text{rpm}}{\text{s}}$, followed by a soft-bake at 150 °C for 5 min on a direct contact hot plate. This first photoresist helps to to get a cleaner lift-off. Afterwards a second photoresist nLOF 2020 (MicroChemicals GmbH, Germany) is spin-coated at 3000 rpm for 45 s with a ramp of 500 $\frac{\text{rpm}}{\text{s}}$ and soft-baked at 110 °C for 5 min. This photoresist was then exposed at at 20 $\frac{\text{mJ}}{\text{cm}^2}$ with broadband UV using a mask aligner (Suss, MA-4), followed by a post-exposure bake step at 110 °C for 1 min on a direct contact hot plate, and a developing step in AZ 326 MIF (MicroChemicals GmbH, Germany) for 40 seconds, The substrates were then evaporated with a metal stack of 10/100/10 nm of Ti/Au/Ti using an electron-beam assisted evaporation machine (Balzer PLS 570, Pfeiffer). The followed lift-off process for nLOF2020 was done in Aceton for 3h. The substrates were then cleaned in Aceton, IPA and deionized water and placed in AZ 326 MIF (MicroChemicals GmbH, Germany) for 5 min to remove the second photoresist LOR3B. To increase the adhesion of the passivation, the substrates are placed in a Piranha solution ($\text{H}_3\text{O}^+/\text{H}_2\text{SO}_4$ 2:1) for 5 min. SU-8 2002 (MicroChemicals GmbH, Germany) is then spin-coated at 3000 rpm for 45 s with a ramp of 500 $\frac{\text{rpm}}{\text{s}}$ and soft-baked at 90 °C for 1 min. To define the electrode opening in the passivation as well as the bond pad openings, SU-8 was exposed at 162 $\frac{\text{mJ}}{\text{cm}^2}$ with UV light at 365 nm using a mask aligner (MA-5 vacuum contact) followed by a post-exposure bake step at 90 °C for 1 min and a developing step in MR Dev 600 (MicroChemicals GmbH, Germany) for

100 s and IPA for 20 s. To finalize the 2D MEA fabrication the Titanium layer on top of the Gold layer at the electrode openings as well as the bondpads was removed using reactive ion etching (RIE) with a gas mixture of Ar/O_2 30/2, RF/ICP powers of 50/500 at 10 °C for 15 s.

3.1.2 2D flexible MEA

The fabrication of the 2D MEA for in-vivo applications consisted on the intercalated deposition of two flexible thin film layers and one metal layer. First, a 5 μm thick Parylene-C layer was deposited on a host silicon wafer via chemical vapor deposition using a PDS 2010 Labcoater 2 (Specialty Coating Systems Inc., USA) and a process vacuum pressure of 25 $mTorr$. In a second step, a metallization process was performed using a lift-off technique. Here, the metal base layer for contact pads, feedlines, and electrodes was patterned after spin-coating the negative photoresist AZ LNR-003 (MicroChemicals GmbH, Germany) at 4000 rpm for 45 s with a ramp of 500 $\frac{rpm}{s}$, followed by a soft-bake at 120 °C for 2 min on a direct contact hot plate. The photoresist was then exposed at 240 $\frac{mJ}{cm^2}$ with a defoc of 2 and a CBD of 800 with UV at 375 nm using a maskless aligner (MLA 150, Heidelberg Instruments, Germany), followed by a post-exposure bake step at 100 °C for 1.5 min on a direct contact hot plate, a developing step in AZ 326 MIF (MicroChemicals GmbH, Germany) for 1.5 min, and a cleaning step in deionized water. The wafer was evaporated with a metal stack of 20/100/10 nm of Ti/Au/Ti using an electron-beam assisted evaporation machine (Balzer PLS 570, Pfeiffer). As a passivation layer, a second 5 μm thick parylene-C layer was deposited. To finalize the 2D MEA fabrication, the outline of the shape of the device, the contact pads, and electrode openings were removed with reactive ion etching. Here, an etch mask was patterned on top of the passivation layer by spin-coating the photoresist AZ 12XT (MicroChemicals GmbH, Germany) at 1000 rpm for 180 s with a ramp of 200 $\frac{rpm}{s}$, performing a soft bake using a hot plate at 110 °C for 4 min, and exposing it to a dose of 350 $\frac{mJ}{cm^2}$, a defoc of 2, and a CBD of 800 with UV at 375 nm with a maskless aligner. Afterward, the wafer was subjected to a post-exposure bake using a hot plate at 90 °C for 1 min, followed by a developing step of 2 min using AZ 326 MIF. After patterning the etch mask, a RIE step using an O_2/CF_4 gas mixture of 36/4 $sccm$, respectively, with RF/ICP powers of 50/500 W was conducted to etch parylene-C. Immediately, a second RIE step was performed to etch the top 10 nm Titanium layer using an O_2/Ar

gas mixture of 20/20 *sccm* with an RF power of 150 *W*. After RIE, the etch mask was stripped using AZ 100 remover (MicroChemicals GmbH, Germany) in a two-bath system. In the first bath, an ultrasound bath using low power for 5 *min* is used, followed by a second bath using fresh AZ 100 remover without ultrasound. Then, the wafer was rinsed in three baths of IPA and cleaned with deionized water.

3.2 3D Microstructure Fabrication

The 3D structures are designed using a computer-aided design (CAD) software, exported as STL files, and converted to print job instructions using Describe (Software by NanoScribe GmbH). For the fabrication of a 3D device a two-photon polymerization 3D printer (Photonic Professional GT2, NanoScribe GmbH, Germany) is used. In this process an erbium-doped femtosecond laser source (center wavelength of 780 *nm*) is focused into a liquid droplet of a photoresin. The used photopolymer is called IP-L 780 and developed by the NanoScribe company for high resolution prints down to 200 *nm*. Two objectives, a Zeiss 25XNA0.8 and a Zeiss 63XNA1.4, are used to print the cylinders, depending on the electrode layout. When using the 25X objective scan speed of 50000 $\frac{m}{s}$, a Laser Power of 100 % and a Power Scaling of 1.2 were used. The slicing distance is set to 700 *nm* and the hatching distance to 400 *nm*. For the 63X objective a scan speed of 8000 $\frac{m}{s}$ and 10000 $\frac{m}{s}$, a Laser Power of 100 % and a Power Scaling of 1.0 is used. Under default conditions given by NanoScribe (Power of 100 % and using the 63X objective) the mean power value delivered by the laser entering the aperture is 50 *mW* [73]. The slicing distance is set to 300 *nm* and hatching distance is set to 200 *nm*. A developing step after the printing process will wash away not polymerized remaining photopolymer. The samples are placed into fresh Mr-Dev 600 developer (MicroChemicals GmbH, Germany) for 10 *min* followed by another 10 *min* fresh Mr-Dev 600 to ensure complete development. Finally, the sample is placed into fresh IPA for another 5 *min* and then air dried. All the mentioned steps are conducted in a certified clean room environment to ensure a stable fabrication environment.

3.3 Template-assisted Electrodeposition of Conductive Material

3.3.1 Electrodeposition of Gold

For the deposition process a liquid gold bath aqueous solution containing 50 *mM* $AuCl_4$ is used. The gold deposition has been done in 2 steps. For the first step a constant

potential (chronoamperometry) of -1.3 V is applied until the current reaches a certain value. A second step is then used to create a homogeneous cap on top of the cylinder with a slight and controlled overgrowing of the gold. For that a constant current is applied for a certain time. The deposition process is conducted using a multichannel potentiostat (CH Instruments Inc., USA) and a three-electrode set up with an Ag/AgCl reference electrode and a Platinum counter electrode.

3.3.2 Electrodeposition of PEDOT:PSS

PEDOT:PSS is being deposited from a self-prepared EDOT:PSS solution containing 0.1 M of EDOT and $75\frac{\text{g}}{\text{ml}}$ of PSS using a multichannel potentiostat (CH Instruments Inc., USA) with a three electrode set up with an Ag/AgCl reference electrode and a Platinum counter electrode is used. Two different techniques are used for the deposition.

- Constant potential (chronoamperometry): A constant potential (chronoamperometry) of 1 V is applied for 20 s .
- CV: A cyclic voltammetry (CV) step is performed as an alternative to the chronoamperometry. The initial voltage is set to 0 V the final voltage is set to 1 V and the scan rate is $0.1\frac{\text{V}}{\text{s}}$. 2 - 15 cycles are deposited.

3.4 Electrochemical Impedance Spectroscopy

Impedance measurements are done on a Biologic VSP-300 (Bio-Logic SAS, Claix, France) potentiostat using a configuration of three electrodes with the MEA electrodes as working electrode, a Platinum wire as counter electrode and an Ag/AgCl pellet as reference electrode. The impedance is measured in 0.1 M phosphate buffered saline (PBS).

3.5 In-vitro Cell Culture

An oxygen plasma surface activation step is performed for 1 min which renders the surface of the 3D MEA to be hydrophilic. The power is set to 100 W , the pressure is set to 0.8 mbar . Prior to cell seeding, the chips are then sterilized in 70% ethanol and washed three times with sterile MilliQ water. Afterwards, the chips are coated with $10\frac{\text{g}}{\text{ml}}$ poly-L-lysine (PLL, Sigma-Aldrich, Steinheim, Germany) diluted in Hank's balanced salt solution (HBSS) $\frac{1}{100}$ at room temperature and in sterile environment for one hour. Before seeding the remaining coating solution is aspirated and the

chips are cleaned three times with HBSS. Cortical neurons are extracted from the hippocampus of Wistar E18 rat embryos (animal testing approval: Landesumweltamt für Natur, Umwelt und Verbraucherschutz Nordrhein-Westfalen, Recklinghausen, Germany, number 81-02.04.2018.A) and separated into individual cells by incubation at 37 °C with 0.05 % trypsin EDTA (Life Technologies GmbH, Darmstadt, Germany), 5 % CO₂, and 95 % humidity for 10 min. The tissue is gently removed and washed 5 times with Supplemented Neurobasal medium (NB medium, Life Technologies GmbH, Darmstadt, Germany), 1 % B-27 supplement (Life Technologies GmbH, Darmstadt, Germany), 0.5 mM L-glutamine (Life Technologies GmbH, Darmstadt, Germany) and 50 $\frac{\mu\text{g}}{\text{ml}}$ of gentamicin (Sigma-Aldrich, Steinheim, Germany). After the last washing step, the supernatant is replaced with fresh supplemented Neurobasal medium and the tissue is triturated until it is completely dissociated. Cells are counted with Neubauer improved cell counting chamber and the wanted amount of cells is plated onto each sample. The samples are kept at 37 °C and 5 % CO₂. One to four hours after cell seeding, the medium is replaced completely with medium. From the first day in-vitro, every three to four days, half of the medium is replaced with fresh warm medium.

After the experiments the samples are cleaned. Trypsin EDTA is used to remove the attached cells from the sample. For that, the sample is immersed into trypsin at 37 °C. After 20 min the trypsin is removed, and fresh trypsin is added for another 1 h to ensure proper detachment of the cells from the complex 3D structures. Samples are then immersed in a 1 % Tergazyme solution in ultra-pure water for several hours.

3.5.1 Fluorescent Microscopy

Fluorescent microscopy after 7 days in-vitro (DIV) is used to analyze the interaction between 3D printed scaffold and neurons. For the staining with the orange dye Dil (1,1'-Diocadecyl-3,3',3'-Tetramethylindocarbocyanine Perchlorate, Thermo Fischer, USA) 3.5 μL Dil (2 $\frac{\text{mg}}{\text{ml}}$ in ethanol) is mixed with 1 mL neurobasal medium (NB medium, Life Technologies GmbH, Darmstadt, Germany). The sample is incubated in the Dil solution for 20 min in an incubator and washed with fresh NB medium three times. For a deep red staining the dye cell mask deep red (Thermofischer, USA) is used. $\frac{1}{1000}$ solution in Hank's balanced salt solution (HBSS, Sigma-Aldrich, Steinheim, Germany) is prepared. The sample is incubated for 30 min and washed three times with HBSS. After staining the samples are measured immediately with ZEISS Axio imager Z1 (Carl

Zeiss Microscopy GmbH, Oberkochen, Germany) with a 20X and 63X water objective.

3.5.2 Cell Fixation and SEM

To investigate the neuronal growth on the 3D printed structures via scanning electron microscopy (SEM) the neurons have to be fixated. For that, the sample is rinsed three times with war PBS (37 °C, Sigma Aldrich, USA) and chemically fixed with 2 % glutaraldehyde (GA) (Sigma Aldrich, USA) solution in PBS for 15 *min* at room temperature. Afterwards the sample is washed three times with PBS and MilliQ water to remove fixative residues. For SEM investigations the fixated neurons need to be dried. critical point drying (CPD) is used to dry the cells. First of all, water in the sample is moderately replaced with ethanol (intermediate medium). The sample is incubated for 5 *min* in 10 %, 30 % and 50 % ethanol, 15 *min* in 70 % ethanol, followed by three times for 5 *min* in 90 % and 95 % ethanol. The sample is then transferred in 100 % ethanol at 4 °C and transported to the chamber of the CPD (CPD 030, BAL-TEC Company). The chamber of the CPD is filled with 100 % ethanol and the samples are placed inside. The chamber is cooled down to 10 °C and ethanol is exchanged by CO_2 . The exchange process is repeated several times until the chamber is filled with CO_2 followed by an increase in temperature to 40 °C and in pressure to 73 *bar*. The CO_2 in the chamber goes into a supercritical phase. Eventually the chamber is evacuated while the sample is dried and dehydrated. To improve the SEM investigations with enhancing the conductivity of the cells and the printed scaffold, a thin layer of iridium oxide (6 *nm*) is sputtered onto the sample (current 15 *mA* for 1 *min*). SEM characterization is carried out with a Gemini 1550 instrument (Leo/Zeiss). The imaging was taken at 3 *kV* acceleration voltage.

3.6 Ex-vivo Rat Retina

The retina was extracted from adult rats provided by Charles River Laboratories, USA and all experiments were approved by the Landesumweltamt für Natur, Umwelt und Verbraucherschutz Nordrhein-Westfalen, Recklinghausen, Germany (record number: 81-02.04.2018.A190). First the animal was deeply anesthetized with CO_2 followed by a decapitation. Right away the eyeballs were enucleated and immersed in fresh ACSF (artificial cerebrospinal fluid), which contains (in *mM*) 124 *NaCl*, 24 *NaHCO₃*, 3 *KCl*, 1.25 *NaH₂PO₄*, 1.25 *MgCl₂*, 2 *CaCl*, and 10 glucoses. The medium was constantly oxygenated with carbogen gas containing 95 % O_2 and 5 % CO_2 (The Linde Group,

Germany) and pH of 7.4 adjusted with sodium bicarbonate ($NaHCO_3$). The preparation of the retinal tissue was performed. One eyeball was opened along the ora serrata to extract the cornea, lens, and carefully remove the vitreous body. The procedure was then executed with the second eye to ensure constant oxygenation. After that, the posterior eyeball is cut in half and the two pieces of retina are carefully isolated. One piece is then stored again in oxygenated ACFS and the other one is prepared for the first experiment. Here, the retina is placed on a donut-shaped piece of filter paper with a pre-cut central hole of 1.5 mm with the ganglion cell layer facing upwards. It is then flipped, placed inside the perfusion chamber, where it is fixed with insect pins to hold it in its place. A constant perfusion was given to the tissue to keep its vitality.

3.7 Ex-vivo Human Brain Slice

Human neocortical brain slice cultures were prepared from access tissue (cortical tissue outside the epileptic focus, resected in order to gain access to the pathology) obtained from patients undergoing epilepsy surgery. Approval (EK067/20) of the ethics committee of the University of Aachen as well as written informed consent was obtained from all patients. The tissue preparation was performed by the clinic for neurology, Uniklinik RWTH Aachen. To ensure tissue integrity the cortex was carefully micro dissected and resected with only minimal use of bipolar forceps. The section is cut perpendicular to the surface, thus it contains all 6 layers of the Cortex. It was then directly transferred into ice-cold artificial cerebrospinal fluid (aCSF) (in mM: 110 choline chloride, 26 $NaHCO_3$, 10 D-glucose, 11.6 Na-ascorbate, 7 $MgCl_2$, 3.1 Na-pyruvate, 2.5 KCl , 1.25 NaH_2PO_4 , und 0.5 $CaCl_2$) equilibrated with carbogen (95 % O_2 , 5 % CO_2) and immediately transported to the laboratory. During the whole process the tissue was kept submerged in cool and carbogenated aCSF at all times. After removal of the pia, tissue chunks were trimmed perpendicular to the cortical surface and 250–350 μm thick acute slices were prepared using a Microm HM 650V vibratome (Thermo Fisher Scientific Inc). Afterwards the slices were immediately transported to the laboratories at the IBI-3, Forschungszentrum Jülich. During the 30 min transportation the slices were kept in aCSF oversaturated with carbogen. Once the slices reached the laboratory they were placed into aCSF (in mM) 124 $NaCl$, 24 $NaHCO_3$, 3 KCl , 1.25 NaH_2PO_3 , 1.25 $MgCl_2$, 2 $CaCl$, and 10 glucoses oxygenated with carbogen and placed on a hot plate. Electrophysiological recordings were conducted up to one day after slice preparation.

3.8 Electrophysiology

3.8.1 Stiff Samples

The Bioelectronic Multifunctional Amplifier System (BioMAS) has been developed in the IBI-3 institute of FZ Jülich and is used for extracellular measuring and recordings of cultured cells on MEA chips. This setup consists of a pre-amplifier, main-amplifier, analog-digital converter (ADC) and a software written in LabVIEW. The pre-amp is integrated into a headstage which includes a holder for the chip and thus enables the connection between the BioMAS and the MEA with contact pins within the headstage. These contact pins ensure a tight contact of the bondpads of the chip with the measuring set up. The pre- amplification converts the measured current signal into a voltage signal which is then amplified by a factor of 10. Further post amplification of 1, 10, 100 can be performed by the main amp which can lead to a maximum amp of the output voltage signal of 1000. The ADC enables simultaneous acquisition from the 64 electrodes within one MEA chip and converts the analog signal into 16-bit long digital samples. Shielding of the set up from external impacts is ensured by placing the measurement setup into a grounded Faraday cage. The measured signals can be observed in real time by a LabVIEW based software. Besides the real time observation, the program gives the opportunity to change the settings of certain parameters (e.g. parameter range and sampling rate) and the recording of the voltage signals. First the headstage is connected to the measuring set up and the chip is placed in this headstage. A silver/silver-chloride reference electrode is located into the culturing medium. The wanted parameters for the measurement are changed in the LabVIEW software. The recorded data sets can be post processed in BioMAS Analyzer, a MatLab based program (provided by Brings, F., ICS-8, Research Center Jülich).

3.8.2 Flexible Samples

For ex-vivo recordings, the ME2100-System (Multi Channel Systems MCS GmbH, Germany) and a 32 channel headstage (ME2100-HS32-M-3m) were used. The NeuroNexus adapter (ADPT-NN-16/32) connects the headstage to the customized 16 channel PCBs. The headstage was mounted on a micromanipulator (Luigs and Neumann GmbH, Germany) to enable precise, remotely controlled insertions. Offline data processing was performed using the McsMatlabDataTools Matlab toolbox (Armin Walter (2023). McsMatlab-DataTools (<https://github.com/multichannelsystems/McsMatlabDataTools/releases/tag/1.3.1>),

GitHub. Retrieved March 23, 2023.) to import HDF5 files and self-written script for filtering and extracting the spiking characteristics.

4 3D Neuronal In-Vitro System

To study and control neuronal networks in all three dimensions a suitable, high resolution scaffold geometry is necessary. As already mentioned, the TPP process allows for a very high design freedom. Therefore, the scaffold geometry can be designed to study different properties of 3D neuronal networks. With printing many freestanding microchannels which connect elevated cavities Harberts et al. [15] have created defined neuronal networks where the microchannels act as guidance for neurite growth to investigate neuronal outgrowth. Larramendy et al. [7] on the other side have printed complex microcontainers to define the position of each neuronal body while at the same time allow for cells to freely grow their projections to form a 3D arrangement which can be used for potential applications in drug screening or creating artificial organs in the future.

The scaffold geometry used in this thesis is based on the mentioned work from Larramendy et al. [7]. They investigated the most suitable cage geometries like cage diameter and cage edge diameter. The aim was to have only one cell body in each cage. They introduced cell barriers between the single cages to prevent cell bodies from moving between the cells and on the same time allow connections between the neurons. With printing several arrays of half cages next to each other followed by a stacking procedure after cell seeding they could create a controlled 3D neuronal network where the cell bodies were kept inside the cages and the cage edges were used as a guiding system for axons and dendrites. The introduced cell barriers allowed for a high directional freedom in cell connections which led to healthy 3D neuronal networks in-vitro. To stack the cages on top of each other and thus create the third dimension they added alignment blocks at the side of each cage array. The alignment blocks are used to improve the alignment of the different cage layers. Furthermore the cage arrays have small holes at the bottom and small pins at the top. During the stacking process the pins fit into the wholes and lead to an increase in adhesion between the stacked layers. Nevertheless they mentioned problems with the stability of the stacked layers which often disconnect during transportation. Furthermore, the alignment was not perfect.

Based on their results the aim of the first part of this thesis is to develop an optimized approach to obtain stable, healthy and precisely controlled 3D neuronal networks. The TPP process is used to 3D print stiff cell scaffolds with high resolution. As mentioned

already, compared to flexible scaffolds, stiff scaffolds have the advantage to precisely control the network formation by adjusting the scaffold geometry in the sub μm range. The following Figure 11 illustrates the idea to create 3D neuronal networks.

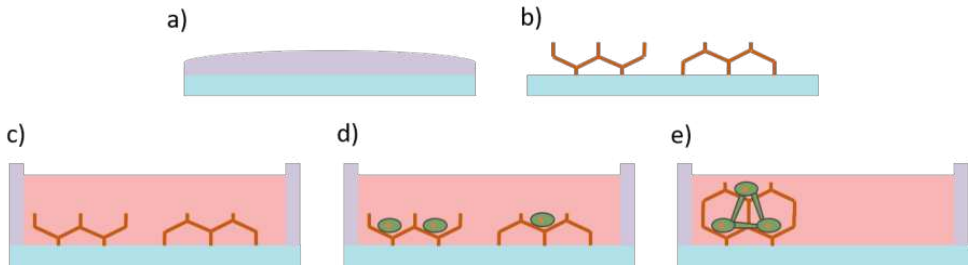


Fig. 11: Approach to create 3D neuronal networks with the help of a printed stiff scaffold. a) Liquid droplet of photopolymer IP-L 780 on a glass substrate. b) Printed cage geometry after development of the structure. c) Coat polymer with Poly-L-Lysine and define seeding volume. d) Seed primary cortical rat neurons onto the printed geometry. e) Stack cages onto each other to create third dimension.

4.1 Optimization of 3D Print

The CAD software CATIA V5 is used to create the cage design. The same geometries are used which Larramendy et al. [7] found to be the most suitable once. The geometry can be seen in Figure 12.

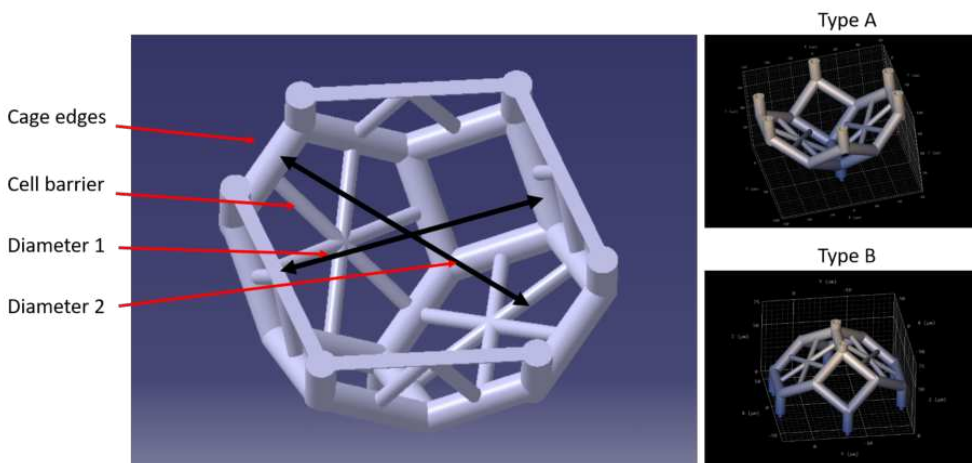


Fig. 12: CAD design of a single cage. Illustration of the difference in Type A and Type B designs.

The cage diameter 1 is $42 \mu m$ and cage diameter 2 is $46 \mu m$, the cage edge diameter is $4.5 \mu m$, and the cell barrier diameter is $2.25 \mu m$. Two slightly different designs are

created, Type A and Type B. The Type A structure includes small holes ($2\ \mu\text{m}$ diameter) matching the pins of the Type B structures. During the stacking process of Type B onto Type A the pins will fit into the holes and ensure a certain stability. After the geometry is created the software DeScribe (NanoScribe GmbH, Germany) is used to slice and hatch the geometry. As the dimensions of the cages are very small the slicing distance is set to $300\ \text{nm}$ and the hatching distance is set to $200\ \text{nm}$ to ensure a suitable print resolution. Figure 13 illustrates the difference in hatching distance and slicing distance. Hatching and slicing subdivide the structure and determine the distance of the single voxels.

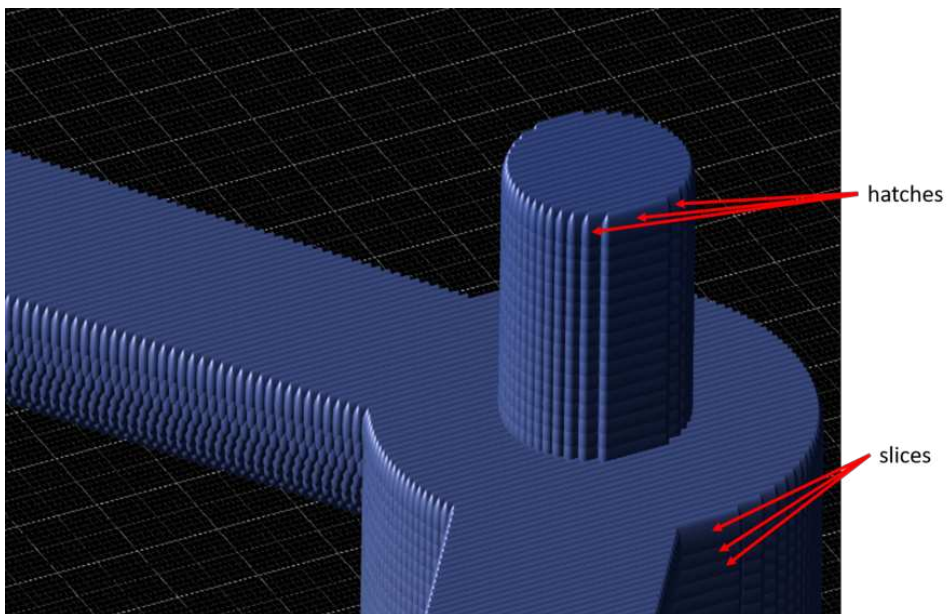


Fig. 13: Illustration of the sliced and hatched scaffold design in DeScribe (NanoScribe GmbH, Germany).

Next to the hatching distance also the hatching direction is an important parameter which influences the print result. Figure 14 illustrates the difference between a hatching angle of 0 degree and of 90 degrees.

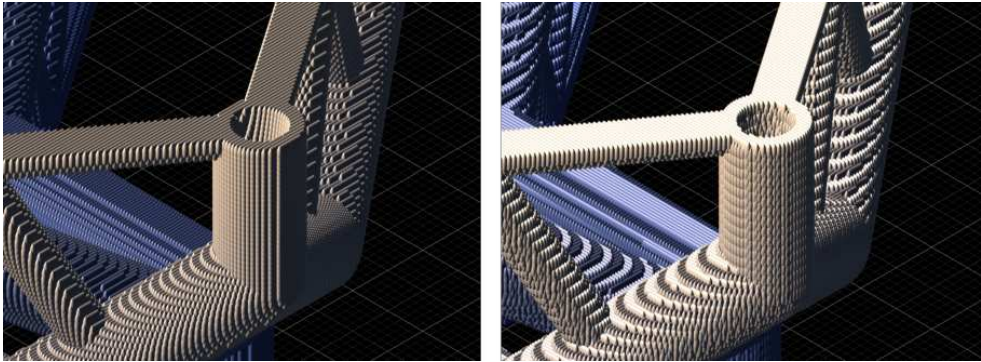


Fig. 14: Difference between a hatching angle of 0 degree (left) and 90 degrees (right). Especially round structures are printed more homogeneously with a hatching angle of 90 degrees.

Some properties of the printed structure like morphology, or dimensions are not necessarily homogeneously distributed along the print but may differ parallel to the hatching direction and perpendicular to it. Especially for small dimensions this difference can be crucial. Therefore, the hatching angle is set to 90 degree. The hatching direction changes by 90 degree from layer to layer. Especially round structures like the cage edges and cage barriers can be printed more precisely in this way. To achieve stable structures the high resolution photoresist IP-L 780 (NanoScribe GmbH, Germany) in combination with a 1.4N 63X objective is used for the print process. IP-L 780 has been developed by the NanoScribe Company for high stability of high resolution prints as well as small shrinkage. Several print parameters like laser power and scan speed have to be optimized to get a stable print. NanoScribe GmbH developed special print recipes for certain objective, resin and substrate combinations. For the first prints the recipe for IP-L 780 on ITO coated glass substrates is used as a starting point and thus the laser power is set to 80 % and the scan speed is set to $10000 \frac{\mu m}{s}$.

Figure 15 shows printed cages after the development in a diamond 4X4 array.

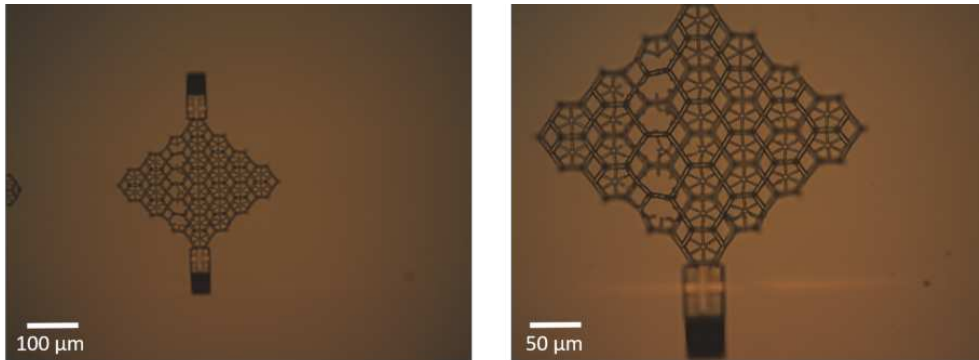


Fig. 15: Light microscopy pictures of printed cage scaffolds in a 4X4 diamond shape array. Too less laser power leads to unstable small features.

Especially the smallest structures, the cell barriers, are not printed well completely. A too low degree of polymerization of the resist leads to unstable small features. Those features then either get destroyed already during the printing process or during the developing process. To increase the degree of polymerization and thus the structure stability the laser power has to be increased for the next print. Anyway the laser power should not be increased too much as otherwise the resist will burn which will lead to bubbles. Therefore, the laser power is increased to 100 %.

The result can be seen in Figure 16.

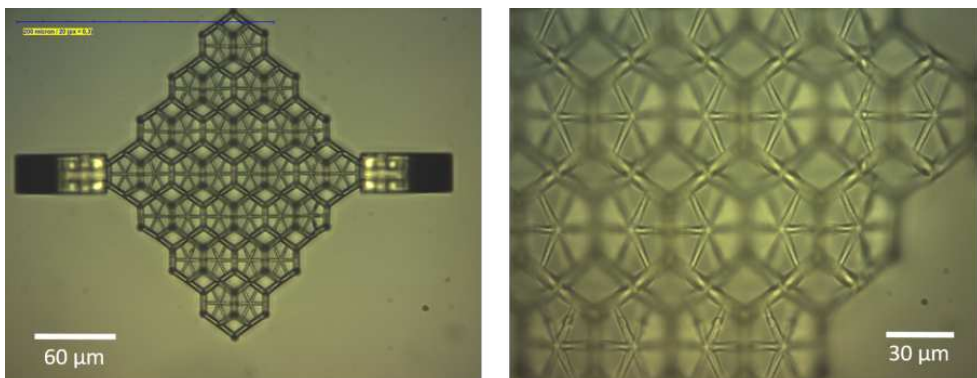


Fig. 16: Light microscopy pictures of a stable 4X4 cage array (left). Zoomed in picture of stable smallest features (right).

All of the cages are being printed well without any broken cell edge. Even the smallest structure like the cell barriers are stable after the development. To get a closer look at the printed cage structure SEM investigations of the print are conducted. Figure 17

shows a cage structure after development.

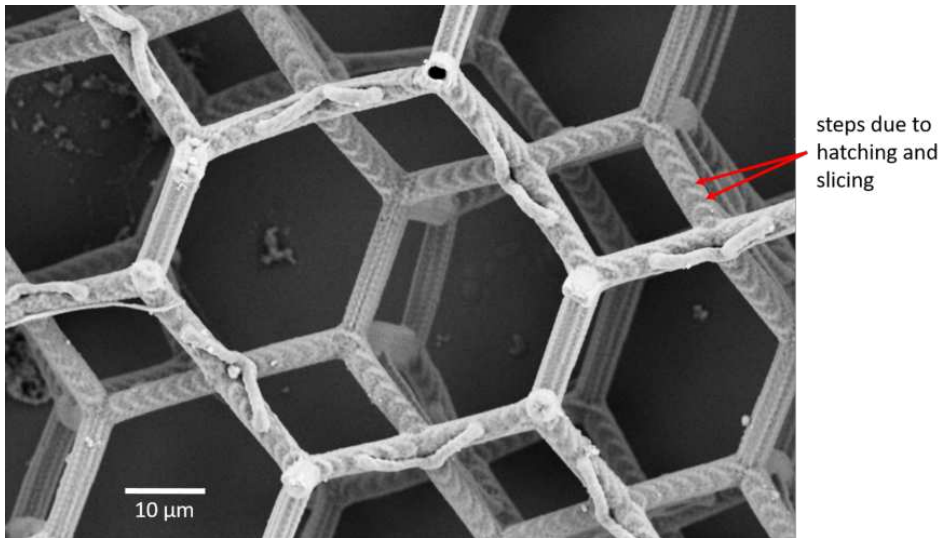


Fig. 17: SEM picture of a printed cage scaffold. The single steps at the surface of the cage edges due to hatching and slicing can be seen.

Also the SEM investigations proof the suitability of the TPP 3D print technique for such complex and high resolution structures. All parts of the structure can be printed well with increased laser power. The high resolution of the SEM can moreover even display the surface roughness of the printed cage edges. These steps (highlighted in Figure 17) come from the hatching and slicing of the structure. They already can be seen in the preprint software after subdividing the structure in hatches and slices (see Figure 13). The structures are subjected to shrinkage during the developing step due to a change in material properties. IP-L 780 is used also because it supposes to have less shrinkage than other resists [73]. Table 1 compares the theoretical cage diameters, cell edge diameters and cell barrier diameters with the practical values after development.

Tab. 1: Comparison of theoretical diameters and diameters after shrinkage to determine the overall shrinkage of the photopolymer.

	Theoretical dimensions in μm	Printed dimensions in μm	Shrinkage in %
Cage diameter 1	46	44	4.5
Cage diameter 2	42	39	7.2
Cell edge diameter	4.5	4	12
Cell barrier diameter	2.25	2	12

NanoScribe claims shrinkage values for the IP-L resist between 1 % and 15 % [73]. As the amount of shrinkage highly depends on the degree of polymerization (e.g. higher degree of polymerization leads to lower shrinkage) the shrinkage varies for different objective- substrate combinations as well as printing parameters. As the laser power is set to be higher than what is used for the standard recipes from NanoScribe the shrinkage it expected to be lower than 15 %. Thus the shrinkage values which can be seen in Table 1 lay within the expected range. The reason for the higher shrinkage for the smaller edge and barrier structures most likely come due to the inaccurate placing of the measuring bar. This influence increases with smaller structure size as here 1 % already lays within the sub 50 *nm* range.

4.2 Optimization of the Stacking Process

After finding the optimized printing parameters as a next step the printed structures have to be stacked on top of each other to create a three-dimensional scaffold system. For that, first of all alignment blocks, similar to those used in the work from Larramendy et al. [7] are added to the cage structures. They consists of blocks with 50 μm X 50 μm X 50 μm with cross shapes at the top and the bottom which slide into each other during stacking (similar to the idea with the pins and the holes). Additionally to the alignment blocks, carrying systems are added to be able to carry single arrays and align them on top of each other. Each cage layer has a height of 35 μm , e.g. a stack of 3 cage arrays on top of each other leads to a 3D scaffold with 200 μm , 250 μm and 105 μm in x, y, z direction and 16 cages in each layer. The carrying systems can be seen in Figure 18.

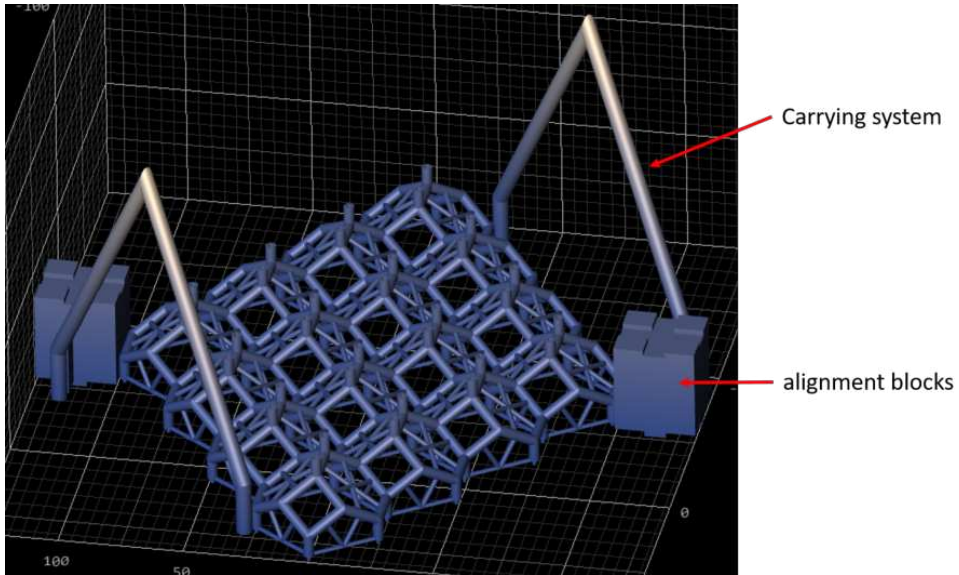


Fig. 18: CAD design of 4X4 cage array including the carrying system and alignment blocks.

They have diameters of $10\ \mu\text{m}$ and a height of $200\ \mu\text{m}$. To carry the structures, a glass pipette is pulled out to a width of only a few micrometer (similar to the glass pipettes used for patch clamping) and fixed to a micromanipulator which allows the manipulation of the x,y, and z direction of the glass pipette in the μm range. This is necessary to precisely align the cage structures on top of each other. As a first step the glass pipette tip is driven underneath the carrying system of one array. With driving the glass pipette upwards the cage array is carried up as well as it can be seen in Figure 19.

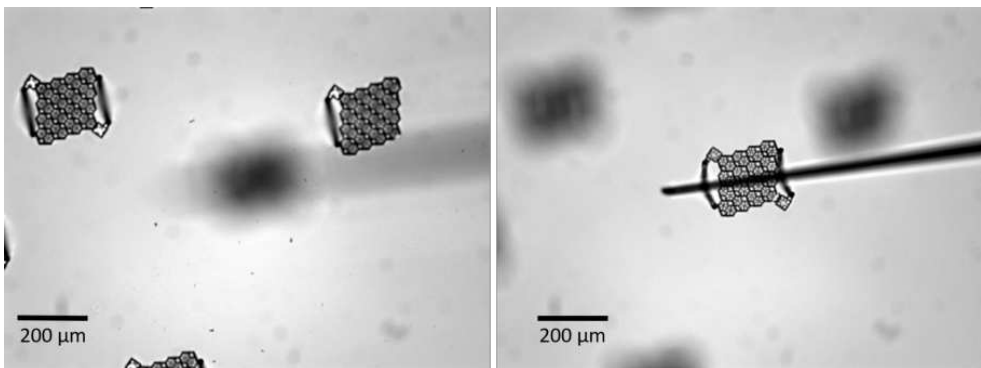


Fig. 19: Carrying procedure using the carrying system and a thin glass pipette. Left: Focus is set to the substrate surface; right: Focus is set to the lifted up cage array.

The focus of the left image of Figure 19 is set to the printed structures still adhering to the substrate. The focus of the right image is set to the structure which is lifted up with the glass pipette. The cage structure as well as the carrying system is stable enough to survive the lifting up as well as moving process.

The connection between the cage array and the carrying system has to be stable enough to not break during the moving process. A thickening of the connection between cage array and carrying structure leads to an increase in stability of the stacking process. After lifting up of one array and driving it on top of another array it is lowered down again. The alignment blocks are used for the correct alignment in x, y. Once the carried array is lowered and placed on top of the lower array the glass pipette is lowered down a few micrometers more to lose the contact with the carrying system and then driven away. The stacking process is completed. If wanted additional cage arrays can be also stacked on top the same way. The first attempts are carried out in air. To be closer to the final application where cells are cultivated into the cages and thus they are placed into cell medium, for the next step the stacking process is carried out in water. Figure 20 shows the cage structures in water.

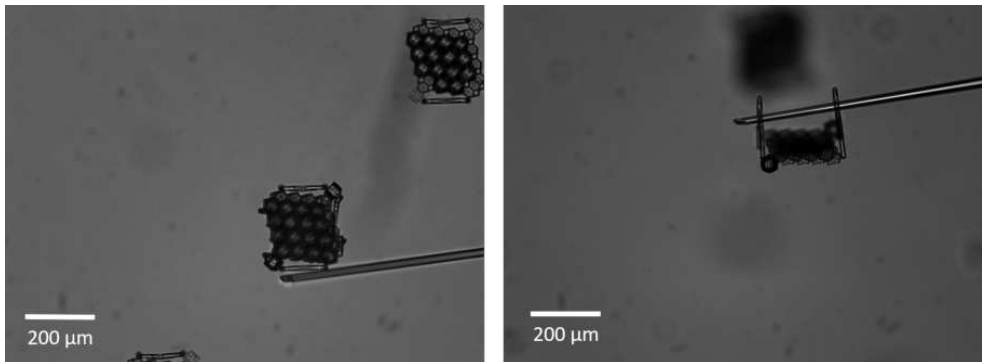


Fig. 20: Stacking process in water. Due to the hydrophobic nature of the polymer air bubbles are trapped underneath the cage array and hinder the stacking procedure.

The reason why the cage arrays appear black is air which is trapped underneath the structures because of the hydrophobicity of the printed polymer. The air bubble leads to problems during the stacking process as it starts to rise as soon as the cage array is released from the substrates. The right image of Figure 20 illustrates this challenge. As soon as the cage structure is lifted up the rising air bubble forces the structure to turn around the glass pipette. Therefore, it can be seen from the side. Furthermore, for

the later application air bubbles will harm the cells and prevent them from forming their network. This is why an oxygen plasma treatment has to be done prior to the stacking procedure to turn the polymer hydrophilic.

In general, the stability of stacked structures is quite low. Similar to what Larramendy et al. [7] experienced, the stacked structures deattach from each other during movement of the substrate due to mechanical disturbances like medium flow. Therefore, the next step is to improve the stability of the stack. For that, guiding rods are added to the lower cage array as it can be seen in Figure 21. The rods have a diameter of $20\ \mu m$ and heights up to $250\ \mu m$. The narrowed tip at the top simplify the alignment and leads to a certain degree of self-alignment.

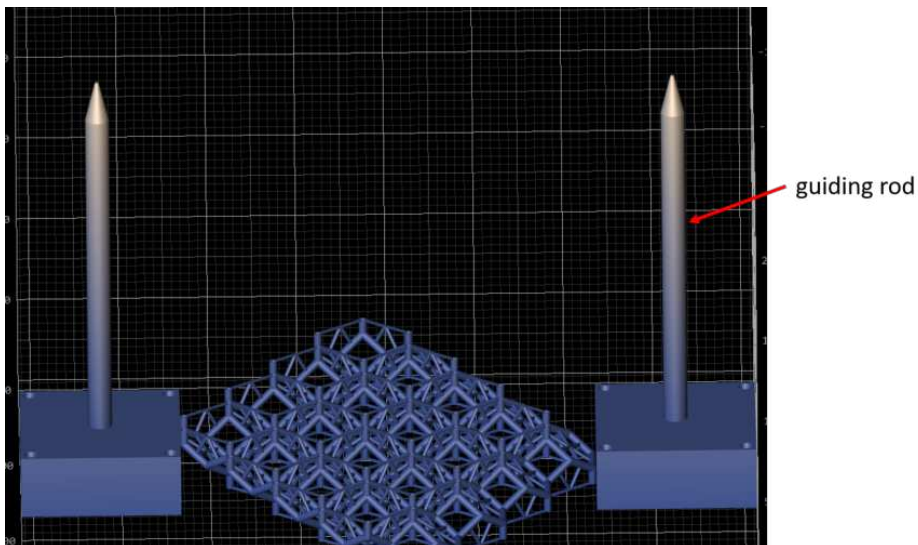


Fig. 21: CAD design of the a 4X4 cage array with integrated guiding rods to improve the stack stability.

Additionally, to the guiding rods, holes are added to the alignment blocks of the upper arrays which diameter matches the diameter of the guiding rod. Thus, the structures can slide down the rods. To further increase the degree for self-alignment the holes of the alignment blocks have a cone shape structure. Its diameter is bigger at the bottom side ($60\ \mu m$) and gets smaller towards the top, finally reaching an opening diameter matching with the guiding rod. The idea is visualized in Figure 22.

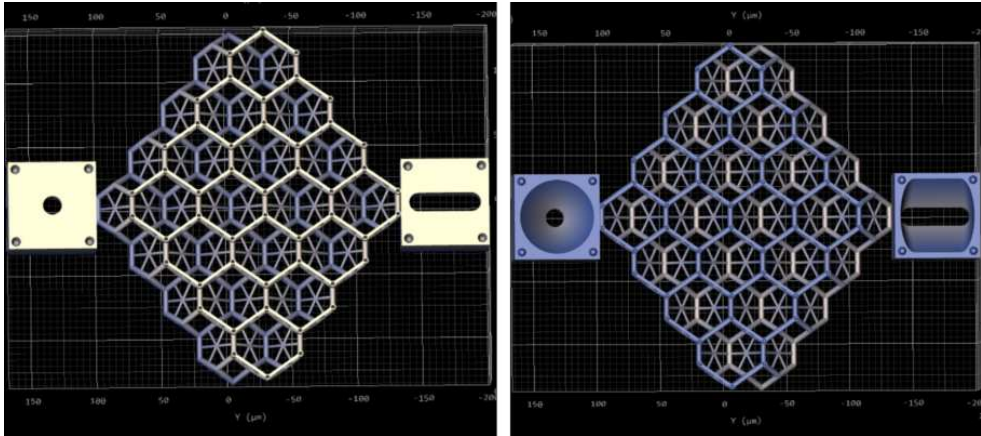


Fig. 22: CAD design of the upper 4X4 cage arrays with adjusted alignment blocks. The designed holes are bigger at the bottom (right image) and match with the guiding rod diameter at the top (left image).

Shrinkage of the structures during the developing step can happen inhomogeneously and might slightly differ from cage array to cage array. In this case the distance between the guiding rods and their diameter and the distance and diameter of the holes can slightly be different which can lead to stacking problems as the rods do not fit anymore into the holes. To overcome this problem the holes are elongated into x and y direction as seen in Figure 22 which lead to a certain degree of freedom in x and y direction but still results in a stable stack. With adding the guiding rods it is possible to stack more than 5 cage arrays on top of each other without losing the stability of the stack which can be seen in Figure 23.

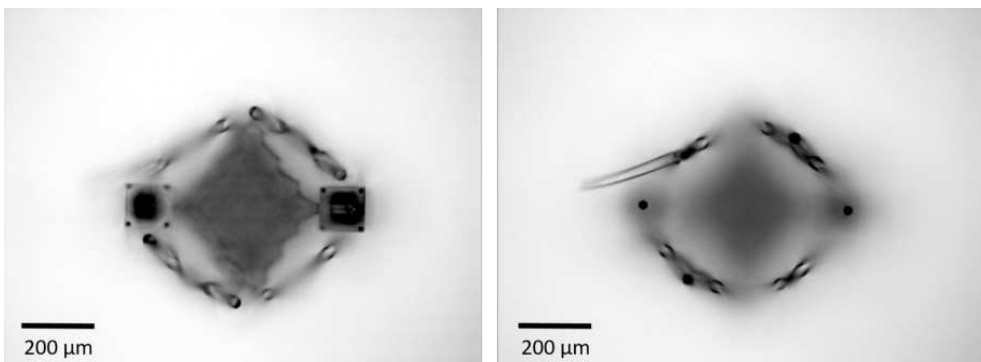


Fig. 23: Light microscope image of a stable and perfect aligned final stack of 5 cage layers. Left: Focus is set to the alignment blocks of the upper most cage array; right: Focus is set to the top of the guiding rod.

The focus on the left image is set to the alignment blocks of the upper most cage array. The focus on the right image is set to the top of the guiding rods. Only the height of the guiding rod limits the amount of layers which can be stacked. To avoid a crashing of the carrying systems the cage arrays are stacked in an alternating orientation of 90 degree.

The developed cell cage structure from Larramendy et al. [7] could be successfully reproduced. Suitable printing parameters were found to get a stable structure. SEM investigations show a shrinkage of the printed structure lower than 10 %. To stabilize the stacked structure guiding rods were introduced to the structure. They furthermore drastically simplify the alignment procedure with allowing a certain degree of self-alignment. This way, it was possible to stack more than five layers on top of each other without losing the stability of the stack.

4.3 Increasing Stack Stability

Next to the adhesion of the layers between each other, also the adhesion between the printed structures and the substrate is of high importance for the overall stability of the stacked layers. The adhesion of the lowest cage array to the substrate should be as high as possible to ensure a high stability during the whole stacking as well as cell seeding procedure. On the other side the adhesion of the cage arrays which are meant to stack onto the lowest structure should not be higher than the stability of the cage structure itself otherwise the lifting up process is impossible and the cage structure will be destroyed.

For the first experiments the structures are printed onto a glass substrate which is coated with a thin Indium tin oxide (ITO) layer. This thin layer helps for an automatic interface finding scenario. The 3D printing software has the option to automatically find the interface between the resist and the substrate. The software checks for a transition between two materials (liquid resin and substrate surface) with different optical properties (e.g. change in refractive index along the optical path). Finding the correct interface is of high importance. Without an accurate interface position, the laser will either be focused too deep in the substrate or too far above. Printed parts within the liquid resin that are not connected to the substrate drift away during printing as a result of convection or mechanical disturbance such as stage movements. Unconnected parts are washed away during development of the structure. Starting too deep inside the

substrate will lead to only part of the structure being printed. Automatic interface finding works well for the default resin- substrate combination (e.g. IP-L 780 printing on ITO coated glass substrate). After the system has found the interface it is possible to start the print at a certain depth “inside” the substrate. The laser will then set the focus for writing the first layers of the structure inside of the substrate resulting in the first (or even more) layer(s) not being printed completely. The deeper the starting point of the print process is set into the substrate the more laser energy is being absorbed at the substrate-resin interface and thus the higher is the degree of polymerization of the first layers at the interface which leads to slightly higher adhesion to the substrate.

This phenomenon is used to increase the adhesion of the lowest structure with starting the print 800 *nm* inside the substrate. The adhesion of the other structures is kept smaller with starting the print only 300 *nm* inside the substrate. In any case the adhesion has to be high enough so that the printed structures survive the developing step.

After the stacking process was optimized the next step is to seed primary cortical neurons onto the printed structures and stack them on top of each other. For that, one cage array with the guiding rods as well as several cage arrays with alignment blocks are printed next to each other on one substrate. An oxygen plasma step is used to turn the polymer hydrophilic, first to avoid trapped air bubbles as mentioned above, and second to improve adhesion to the cell coating which is applied as a next step. Poly-L-Lysine (PLL) is used as cell coating to improve cell adhesion to the printed structures. A cell density of around 750 neurons per mm^2 is used. After cell seeding the substrates are placed in an incubator for at least 1 *hour* to ensure cell attachment to the cages followed by the stacking process. The stacking process is taking place outside of an incubator only on a hot plate. Therefore, the stacking process has to be done as fast as possible to not harm the neurons.

Figure 24 shows neuronal cells inside and around the cage structures (left image). Furthermore it illustrates the function of the cell barriers (right image).

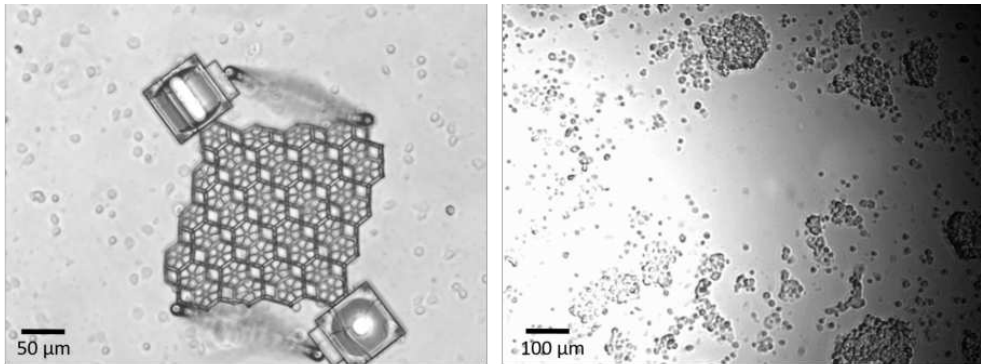


Fig. 24: Left: Light microscopy picture of an 4X4 cage array surrounded by neurons; right: Light microscopy picture of a removed 4X4 cage array after cell seeding.

A cage array has been removed from its original place to be stacked onto the lowest cage array. No cells can be seen on the substrate where the cage array was located. Therefore, no cells could go through the cell barriers and reach the substrate but rather were transported together with the cage array during the stacking process.

However during the stacking process with cells two main challenges occur. First of all, the neurons are not only sticking to the cages but also to the guiding rods, the alignment blocks and the carrying system. With doing so they prevent the upper structures from sliding down the rods. Additionally some remaining tissue from the neuron extraction process is always captured by the triangle shape of the carrying system and agglomerates at the triangle tip where the glass pipette needs to carry the cages. Figure 25 illustrates the challenge.

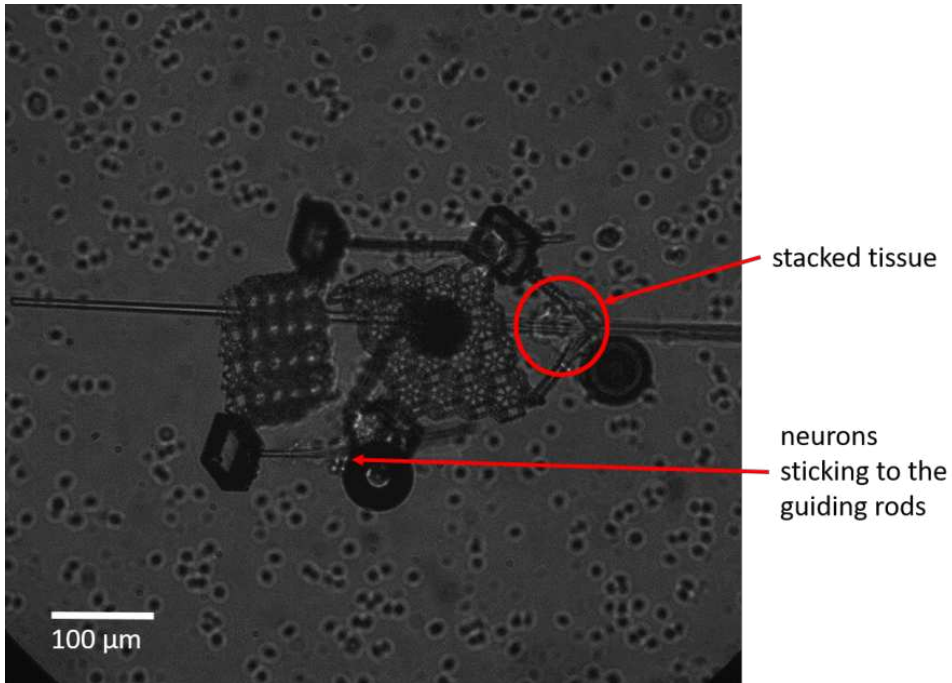


Fig. 25: Light microscopy image of a stacking procedure with cells. Cells and remaining tissue sticking to the guiding rods and carrying system prevent a stable stacking process.

The second challenge is the low adhesion of the lowest cage array to the substrate. During the whole cell culture procedure like seeding and feeding the printed structures are all the time subjected to strong medium flow. Thus during the stacking procedure the lowest structure detaches from the substrate as it can be seen in Figure 26.

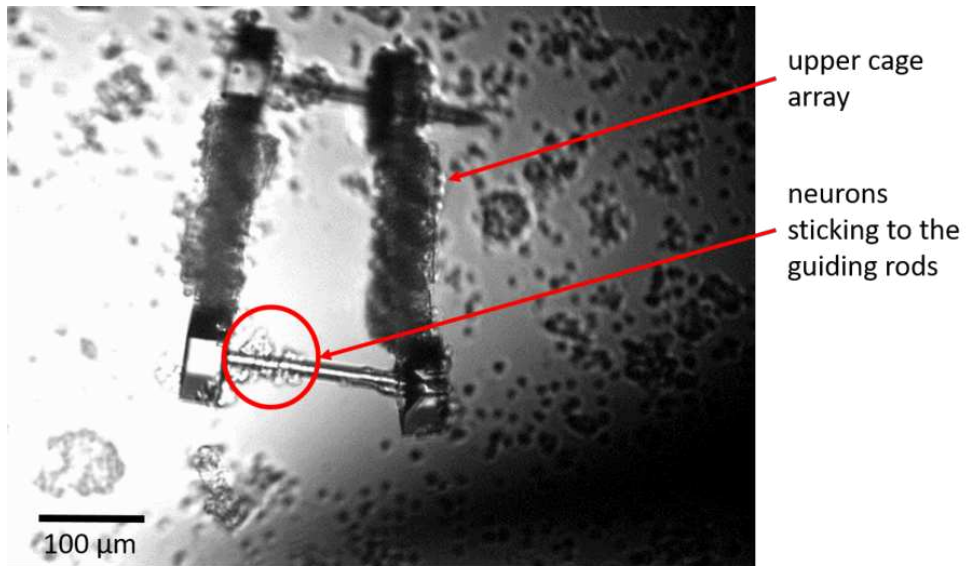


Fig. 26: Light microscopy image of a detached and tilted stack. Again cells sticking to the guiding rods prevent the upper array from sliding down the rod

The lowest cage structure is released from the substrate during the stacking process and tilted to the side. The alignment blocks of the upper cage layer could not slide down the whole rod because of neurons and tissue sticking to the rod.

The use of a microtweezer as handling unit instead of the glass pipette overcomes the challenge of the sticking cells. No carrying system is needed anymore as the cage arrays can be grabbed by the alignment blocks with using microtweezers. The grabbing, moving and alignment of the structures are more reliable and faster which minimize the harm to the cells. Furthermore, the use of the microtweezer allows for actively pushing the cage arrays down the guiding rod in case there are cells sticking onto it preventing the structures from sliding down. Figure 27 demonstrates the use of a microtweezer as well as a side view of a 3 layer cage stack with cells achieved with the use of a microtweezer.

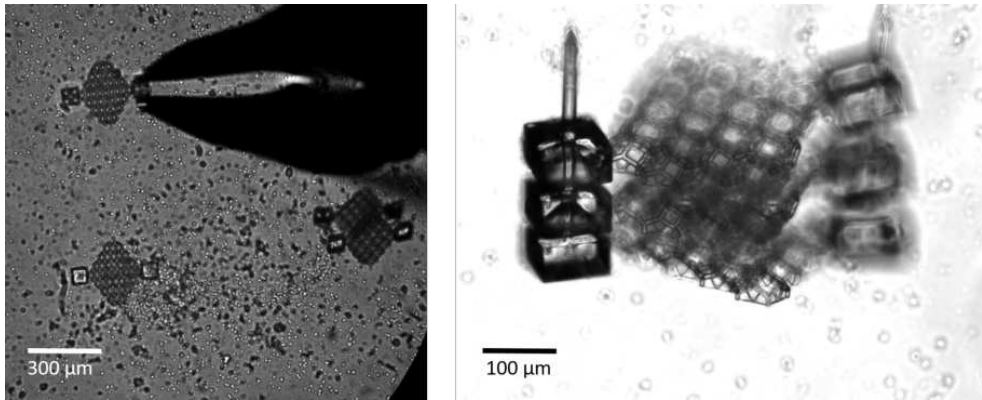


Fig. 27: Left: Light microscopy image of the stacking procedure with the use of a microtweezer; right: Light microscopy side view of a three layer stack.

However the microtweezer will not help with the challenge of the low adhesion of the lowest structure as it can be seen in the right image of Figure 27. A possible way to improve the adhesion is to activate the substrate surface with oxygen plasma before printing. Nevertheless, this is not enough to completely overcome the adhesion challenge. Therefore, as a next approach a silanization step is applied which leads to a hydrophobic surface and a chemical bond between polymerized IP-L 780 and the substrate. For that silane 3-(trimethoxysilyl)propyl methacrylate is used [73]. Before printing the substrate surface is activated with oxygen plasma and then immersed into a solution with the silane and ethanol (ratio $\frac{1}{200}$) for 30 *min*. The silanization results in an effective improvement of the adhesion. However, not only the adhesion of the lowest structure is increased but also for all the other structures. As a result they cannot be lift up anymore as the adhesion is stronger than the stability of the structure and thus the connection between the cage array and the alignment block gets destroyed while moving the microtweezer upwards. This challenge is visualized in Figure 28.

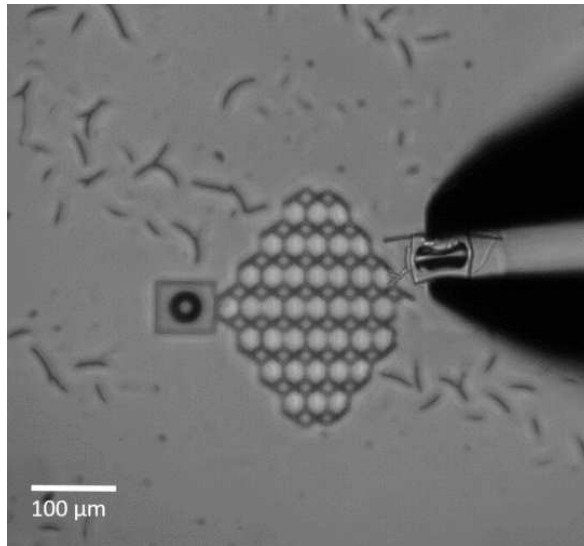


Fig. 28: Light microscopy image of a released grabbed alignment block due to too high adhesion of the cage array to the substrate.

The right alignment block is grabbed by the microtweezer. While the alignment block can be released from the substrate the adhesion to the substrate of the remaining structure is too high and thus the connection between cage array and alignment block is destroyed while lifting up the microtweezer. To overcome the challenge, the silane is only applied to half of the substrate while the other half remains untreated. The lowest array is then printed on the silanised half of the substrate and all the other arrays are printed on the untreated part. This procedure finally leads to a working stacking process resulting in stable cage stacks with cells inside which can be seen in Figure 29.

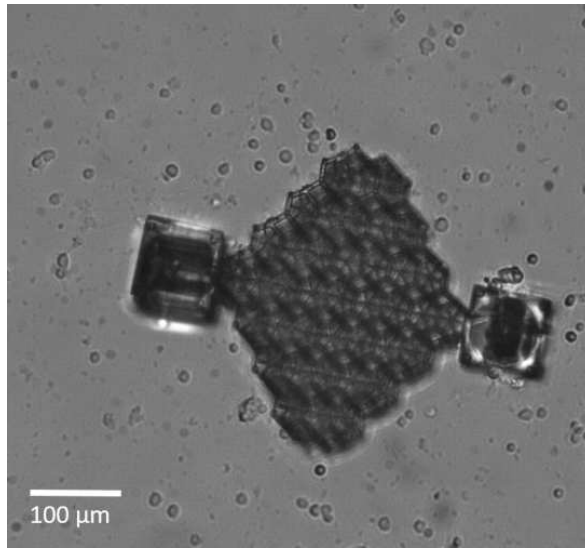


Fig. 29: Light microscopy image of a successful stack of 3 cage layers with cells.

Three cage arrays with cells inside could be successfully stacked onto each other. The stack is stable and thus can be further investigated. The use of a microtweezer instead of glass pipettes led to a significant improve of the stacking process. The stacking was faster and more reliable. Furthermore, the microtweezer allowed for an active pushing of the cage structures which overcame the challenge given by sticking tissue and neurons. Finally, after optimizing the adhesion with adding a silanization step it was possible to get stable 3D neuronal stacks which will be analyzed in the following chapter.

4.4 Investigation of 3D Neuronal Networks

After successfully developing a stable stacking process and fabricating 3D cage stacks with neurons the formed 3D network has to be investigated. For that, both, fluorescent microscopy methods as well as SEM investigations are conducted.

4.4.1 Fluorescent Microscopy Investigation

After the successful stacking procedure the samples are placed back in the incubator. Within 7 days in the incubator the neurons establish their network which then can be investigated and characterized. For a first investigation of the 3D neuronal network the neurons are labeled with a fluorescent dye and observed under a fluorescent light microscope to get an idea about their interaction with the 3D scaffold. Figure 30 shows a two layer cage stack with cultivated neurons after 7 DIV.

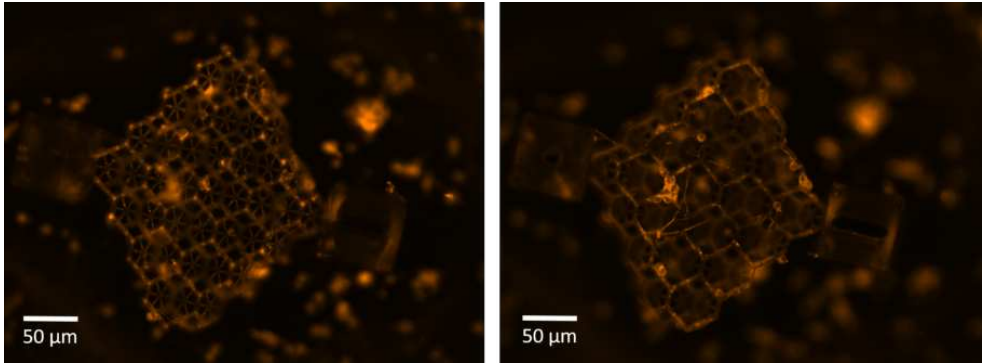


Fig. 30: Fluorescent microscopy image of a 2 layer stack with the membrane labeling dye Dil. Left: Focus is set to the substrate surface; right: Focus is set to the second cage array.

The cells are labeled with Dil (Thermo Fischer, USA), a cell membrane dye in the orange spectrum. Neurons grow inside the cages and are still alive after 7 DIV. They do not avoid the cages which indicates the biocompatibility of the used scaffold material IPL-780. The figure demonstrates the same position at the substrate at different focus planes. Neuronal cell bodies can be seen at all the different heights inside the cage stack and around the cage stack at the substrate surface. The used cell density of 750 neurons per mm^2 and cage diameters of about $50 \mu m$ seem to be suitable to have only few cells sitting in one cage. The cell bodies are not only adhering to the top part of the cage edges but along the whole cage depth and thus in some cages several cell bodies sit at the cage edges of one cage but at different depths of the cage. Further optimizations have to be done in future to only get one cell in one cage.

One challenge which appeared during the first fluorescent experiments is the high autofluorescence of IP-L 780. It reaches almost the whole spectrum with a peak in the green spectrum. To get deeper inside about the interaction of the neurons, axons and dendrites with the scaffold system high resolution images are necessary. But with increasing the resolution, e.g. with using a higher objective, the autofluorescence does not allow to distinguish between the cells and the scaffold anymore. Therefore, another dye has to be used. IP-L 780 does not react to deep red wavelength that is why for the next experiments the dye Cell Mask deep red (Thermofischer, USA) is used. Figure 31 shows a comparison between the dyes Dil and cell mask deep red.

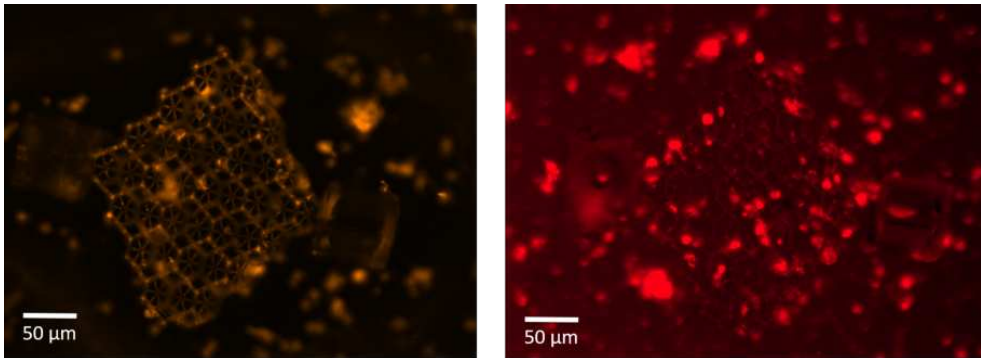


Fig. 31: Fluorescent microscopy image of a 2 layer stack. Left: Membrane labeling dye Dil; right: Membrane labeling dye Cell Mask deep red.

Using the Dil dye in the orange spectrum (left image) the cage edges can be clearly seen. In contrast when using Cell Mask deep red (right image) the cage structure can only be guessed which indicates a sufficient low autofluorescence.

Figure 32 shows a high resolution image with the help of an Apotome (ZEISS company, Germany) of the 3D network labeled with Cell Mask after 7 DIV.

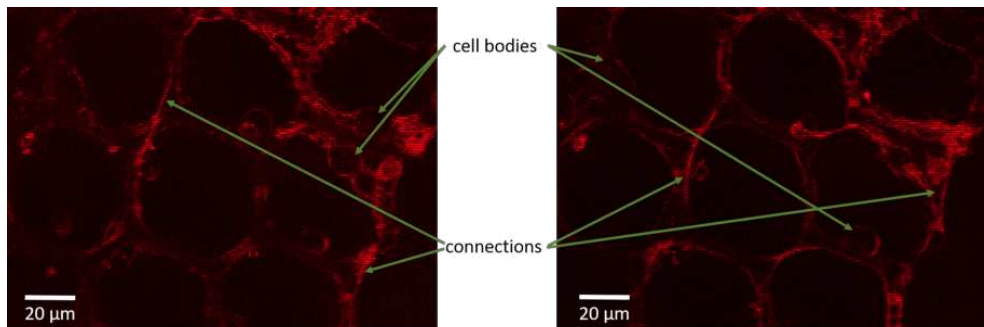


Fig. 32: High resolution fluorescent microscopy image of a 2 layer stack with the membrane labeling dye Cell Mask deep red. Cell bodies as well as cell connections via axons and dendrites are indicated.

The Apotome uses several images with different grid positions, with which the optical section is being calculated. It projects a grid structure into the focal plane of the specimen and then moves it to defined positions using a scanning mechanism. Fluorescence excitation light passes through two glass plates in a slider. When a grid structure is projected onto the first glass plate, the grid pattern is "imprinted" into the excitation light as well. The scanning mechanism tilts the second glass plate and the image of the grid is laterally shifted in the focal plane of the sample. At each grid position, it automatically

captures a digital image. Using a patented algorithm by ZEISS, the system processes all images into a high-contrast, high-resolution optical section. The resulting image has no visible grid structure. This reliable method removes light from non-focal planes even in thicker samples. Cell bodies as well as established connections can be seen. They grow along the cage edges and connect the cell bodies. As expected the cell edges act as guiding and supporting structures for the network. Nevertheless, only the network at the top part of the cage stack can be investigated with the fluorescent microscopy method as the objective comes from the top. As soon as the focus plane is moving further down into the structures towards the substrate surface the pictures get blurry and it is not possible to get high quality pictures. The loss in quality comes from the increase in background signal of the top layers when focusing further down the stack. Even with the help of the Apotome it was not possible to get high quality pictures along the whole cage stack height. In principle the use of a confocal microscope can help to overcome the challenge. However, in the confocal microscope the objective comes from the bottom and thus the maximum height of the structures which want to be investigated is strictly limited to the working distance of the objective. Even though a very thin cover slip can be used as substrate material the height of the stack of already 2 cage layers is too high to be investigated completely. For further investigations in the future the use of a confocal microscope with a high working distance objective is needed.

4.4.2 SEM Investigation

To get a better idea of the established network the cells are chemically fixed inside the cages after 7 DIV with using glutaraldehyde. It binds to nucleophiles of which the amino groups are the most abundant but binding to, e.g., sulfhydryl groups also occurs [74]. The result is a crosslinking of the proteins of the cell. A CPD step afterwards is needed to carefully exchange the water inside the cells with CO_2 to prepare the sample for a SEM investigation. During the CPD process shrinkage of the cells occurs due to the liquid-gas transition which leads to surface tension, and the reduction in physiological volume up to 20 % [74]. The cell stack seen in Figure 33 consists of two cage layers on top of each other.

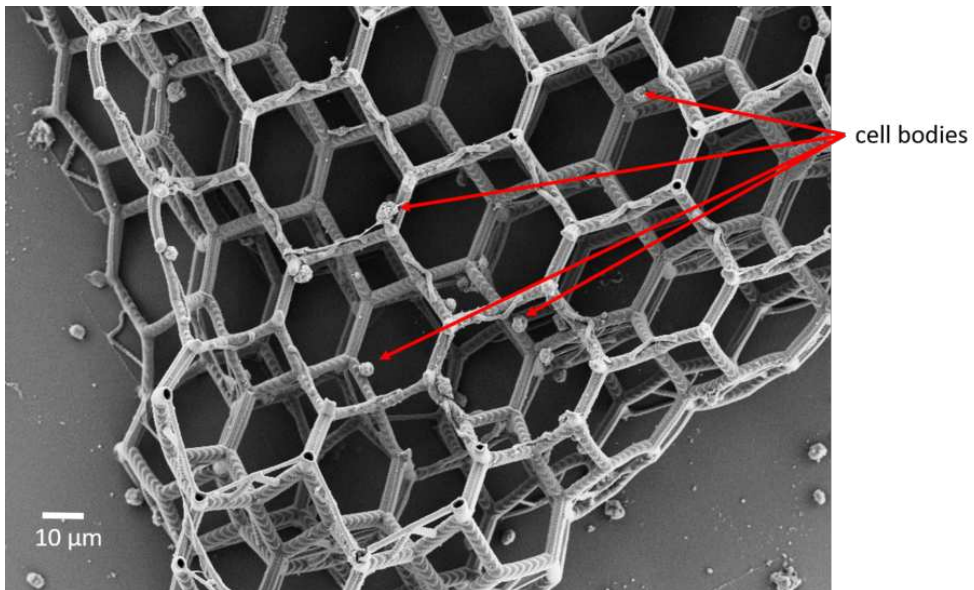


Fig. 33: Scanning electron microscopy image of a two layer stack. Cell bodies inside the cages are indicated.

Single cell bodies can be seen inside the cage structure as well as outside of it. Neurons sit on the cell edges at different heights of the cell stack which agrees with previous fluorescent experiments. Only few cells sit in one cage at the same time which confirms previous findings. To investigate established connections between the neurons Figure 34 shows a zoomed in SEM picture of part of the cage structure.

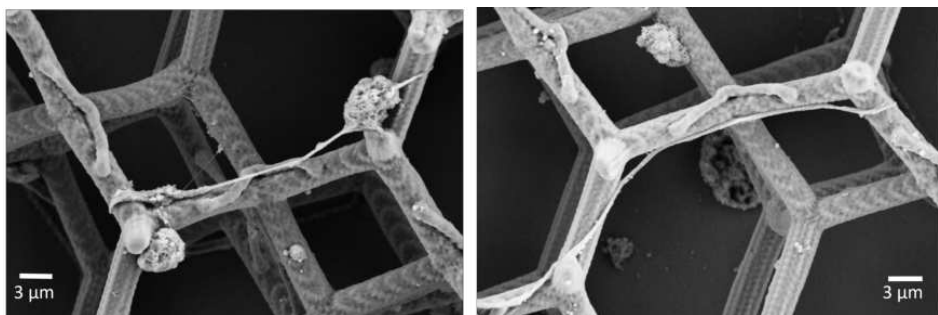


Fig. 34: Scanning electron microscopy image of cell bodies and their connections at two different positions of the cage stack.

The left image in Figure 34 shows two cell bodies in different cages growing at the cage edge. They established a connection which grows along the cage edge using it as a supporting structure. Another connection can be seen on the right image. It also

nicely follows the cage edges. The SEM investigation proves the suitability to guide 3D neuronal growth with using the cage structures as a 3D scaffold system.

In the first part of this work the cage scaffold design has been introduced. The printing parameters were optimized to obtain stable structures. The shrinkage of the scaffolds is in the range of 10 %. Additional parts like the guiding rods are developed and added to the overall printed structure and thus the reliability and stability of the stacking process has been improved significantly. It was possible to stack up to 5 layers onto each other without losing the stability of the stack. Fluorescent microscopy investigations with primary cortical neurons have shown the need of a 3D scaffold as guiding structures for the successful implementation of a controlled 3D neuronal network. Deeper investigations with fixating the cells and using SEM confirms the fluorescent microscopy results. The scaffold material is biocompatible and used by the neurons as a guiding structure to establish connections in all three dimensions.

For possible future applications the developed stacking approach can also be used with all kind of different structures which have to be stacked on top of each other. Further optimizations have to be done to improve the network quality. In this regard, a selective surface coating of the scaffold which for example has been demonstrated in the work of Richter et al. [20] can lead to an even higher controllability of the network. Furthermore, a hybrid system containing a stiff 3D scaffold surrounded by a more flexible matrix will lead to a higher biocompatibility and improved cell growth behavior of the system while at the same time allows for a controlled network growth. NanoScribe GmbH together with BIO INX published new biocompatible, flexible and 3D printable materials which are promising candidates for such a hybrid approach.

5 3D Microelectrode Array

After the development of in-vitro 3D scaffolds for neuronal cell growth and the investigation of the networks with fluorescent microscopy and SEM the next part of the work deals with the electrical characterization of 3D networks.

5.1 3D Electrodes

Being able to measure 3D networks and neuronal tissues like the retina or the brain electrically will allow a deeper inside of how such networks behave. The development of real three-dimensional electrodes for recording and stimulation of neuronal systems in different depths is thus necessary. Therefore, in this chapter, a novel concept for fabricating real, high aspect ratio 3D electrodes is introduced. Figure 35 demonstrates the idea on developing three-dimensional electrodes.

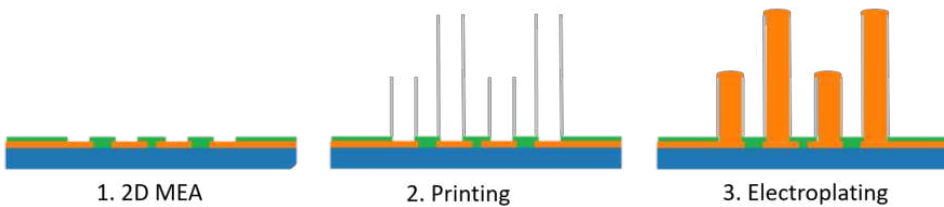


Fig. 35: Schematic of the concept for introducing high aspect ratio 3D microelectrodes.

As a first step, hollow cylinders are printed onto a 2D MEA device using a TPP 3D printer. The cylinders are aligned to the 2D MEA and printed around the electrode openings. In this work, both stiff and flexible 2D MEAs with several different layouts are used to fabricate stiff and flexible 3D implants. This shows the high flexibility and adaptability of the approach. Finally, arbitrary electrode heights are achieved via an electroplating process using the printed cylinders as templates for the deposition and as passivation for the final 3D electrodes. The height of the electrodes is determined by the heights of the cylinders and can be randomly distributed within one MEA design and thus adapted to the final application.

5.1.1 3D Electrode concept

The hollow cylinders are 3D printed on top of a 2D electrical device with the help of a TPP printer (NanoScribe Company, Germany) which has been also used to print the 3D cages in the previous chapter. The hollow cylinders are aligned to the 2D layout and

printed around the electrode openings. Due to the fabrication method the dimensions of the hollow cylinders are not restricted and can be easily changed. The dimensions of the cylinders have to be defined with respect to the final application of the device. The dimensions are given by the height of the cylinders and the wall thickness (outer diameter d_o – inner diameter d_i). The definition of height and wall thickness is illustrated in Figure 36.

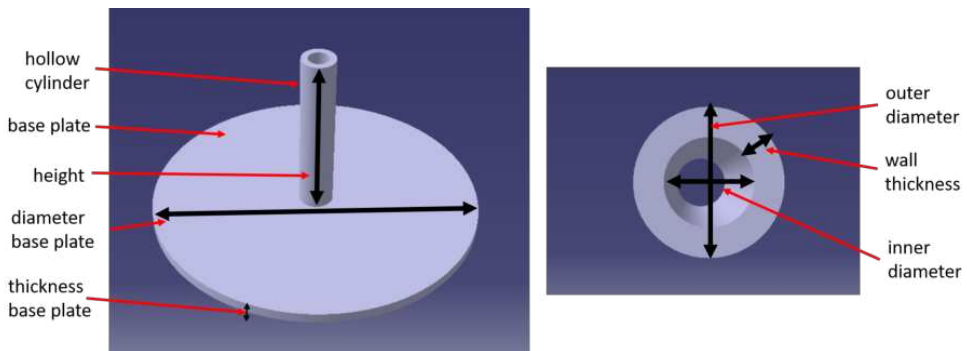


Fig. 36: CAD design of the hollow cylinders which act as templates for the electrochemical deposition. Important structure dimensions are indicated.

To improve the adhesion between the cylinders and the 2D substrate, a base plate is added to the design with a specific diameter and thickness. If the 3D electrodes are used to measure biological tissue where the cylinders will penetrate into the tissue the outer diameter of the cylinder will define the insertion cross-section. Previous work showed that a higher insertion cross-section leads to a higher tissue damage [75]. A small outer diameter of the cylinders is therefore preferred. In both cases, for tissue recordings and in-vitro 3D networks, the electrode dimension will influence the spatial resolution of the electrodes. For single cell recordings the electrodes need to be as small as possible. Next to the x-y dimensions of the cylinders also the z dimensions, meaning the height, has to be chosen with respect to the application. For 3D retina measurements for example the height of the electrodes need to be adjusted to the thickness of the ganglion cell layer within the retina (around $50 \mu m$ [76]). To be able to reach into deeper layers of the brain on the other hand, electrodes with up to several mm height are needed. In principle the used 3D printing technique is not limited in the z-direction wherefore it is in theory possible to print cylinders with several mm up to cm height. The limiting factor is the stability of the structures which is defined by its aspect ratio (cylinder length divided by outer diameter) and wall thickness. Being able to print

high cylinders with small cross sections is preferable. But the higher the aspect ratio the lower is the stability of the structure and the better the printing parameters as well as the geometry of the cylinders have to be optimized to get stable structures which survive penetration experiments into the tissue.

To achieve a stable and accurate print result first of all an appropriate combination of the used objective and photoactive material has to be chosen. As for the cage scaffolds the photoactive material IP-L 780 is used to print the hollow cylinders. IP-L 780 is both optimized for printing with a 63X objective and a 25X objective depending on the needed resolution. The smallest possible printed feature is called voxel (an oval 3D pixel). The overall 3D structure is created by printing voxel next to voxel. The size of the voxel is determined by the objective and the printing parameters. For the 63X objective the smallest possible voxel has dimensions of 200 nm diameter and 700 nm height. Whereas, for the 25X objective the smallest printable voxel has dimensions of 600 nm diameter and 3.6 μm height. Using the 25X objective has the big advantage of reducing printing time tremendously (e.g. 15 min instead of 90 min for 64 cylinders). Nevertheless, the bigger voxel size has a huge influence of the cylinder shape as it can be seen in Figure 37.

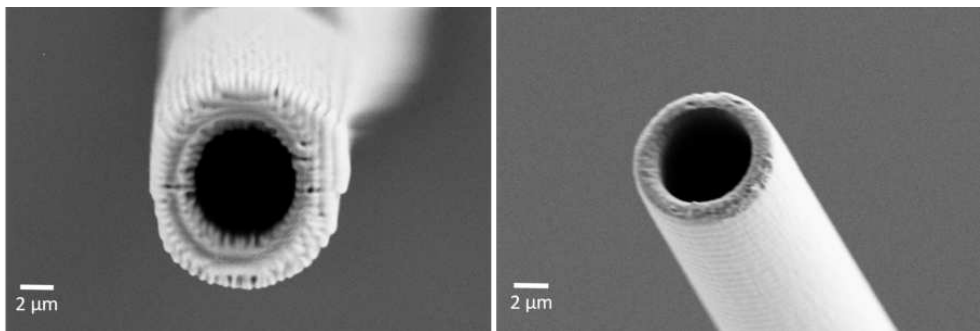


Fig. 37: Scanning electron microscopy top view images of hollow cylinders. Left: Printed with a 25X objective; right: Printed with a 63X objective.

The figure 37 shows a comparison of a printed hollow cylinder with 8 μm opening and 2 μm wall thickness printed with a 25X objective (left image) and a 63X objective (right picture). The surface of the cylinder printed with the 63X objective is much smoother. Due to the bigger size of the individual voxels when using the 25X objective the tiny round structure of the cylinder cannot be printed as accurately as it is the case for the 63X objective. Next to the higher surface roughness also the resulting dimensions of the

cylinder depends on the used objective. For the 63X objective the resulting dimensions match with the CAD design. In contrast the wall thickness and the inner diameter of the cylinder differs from the CAD design when using the 25X objective. Because of the bigger voxels the thin wall thickness of $2\ \mu\text{m}$ cannot be printed accurately resulting in a wall thickness of $3\ \mu\text{m}$ and thus a smaller inner diameter of only $6\ \mu\text{m}$. The outer diameter of $12\ \mu\text{m}$ is achieved with both objectives with a shrinkage of less than 10%. The shrinkage is expected to be low when using IP-L 780 with high laser powers and thus high degree of polymerization and also confirmed in Chapter 4.

Figure 38 compares a cylinder with $12\ \mu\text{m}$ outer diameter (left image) with a cylinder with $20\ \mu\text{m}$ outer diameter (right image) both printed with the 25 X objective.

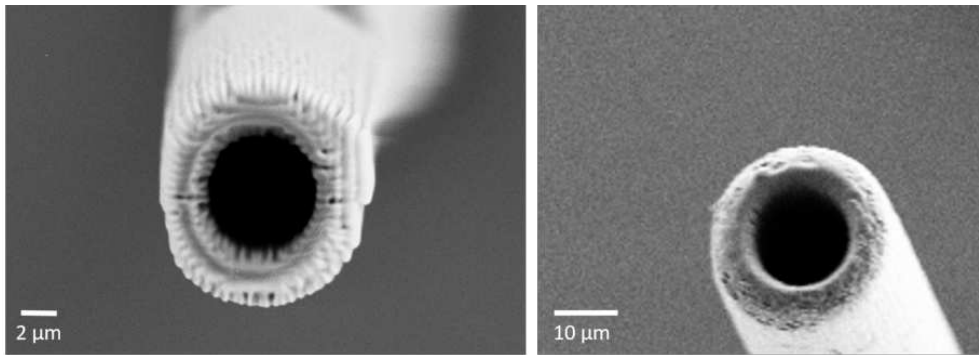


Fig. 38: Scanning electron microscopy top view images of hollow cylinders printed with the 25X objective. Left: $12\ \mu\text{m}$ outer diameter; right: $20\ \mu\text{m}$ outer diameter.

For both dimensions the resulting wall thickness is still more than $1\ \mu\text{m}$ bigger than designed in the CAD file. This is expected as NanoScribe states a minimum structural feature size between $5\ \mu\text{m}$ to $10\ \mu\text{m}$ using the 25X objective with IP-L 780. Nevertheless, due to the bigger dimensions of the $20\ \mu\text{m}$ cylinder the printed voxels form a smoother surface than for the smaller cylinder.

Using a hatching angle of 90 degree showed promising results for the 3D scaffold of Chapter 4. Therefore, also for the cylinders the hatching angle is set to 90 degree. This results in more accurate structure shapes especially for tiny round structures. Next to the slicing and hatching distance, also the laser power and scan speed are important printing parameters which have a big influence of the properties of the printed structure. The higher the laser power and the lower the scan speed of the laser, the higher is the degree of polymerization and the higher is the stability of the structure. Nevertheless, a

higher laser power will increase the size of the voxel, as a bigger area around the focal spot will polymerize. Additionally, too high laser powers will result in burning resist.

Figure 39 shows two cylinders which are printed with low laser powers and thus a low degree of polymerization. This will reduce the mechanical strength of the printed structures and therefore will lead to oval cylinder openings.



Fig. 39: Light microscopy image of hollow cylinders printed with low degree of polymerization and thus leading to structural deformation.

To sum up, an optimization of the different printing parameters as well as objective- resin combinations is crucial for a stable and accurate print result of the hollow cylinders.

5.1.2 Adhesion

After finding the most suitable printing parameters, the adhesion between the 3D print and the 2D MEA has to be increased as it is very important for the fabrication of the 3D device. If the adhesion is too low a successful electroplating process through the cylinders cannot be performed as in this case the solution will creep between the printed structure and the surface of the 2D MEA. Almost no gold will deposit inside the cylinders but rather will grow underneath and around the cylinder as it is illustrated in Figure 40.

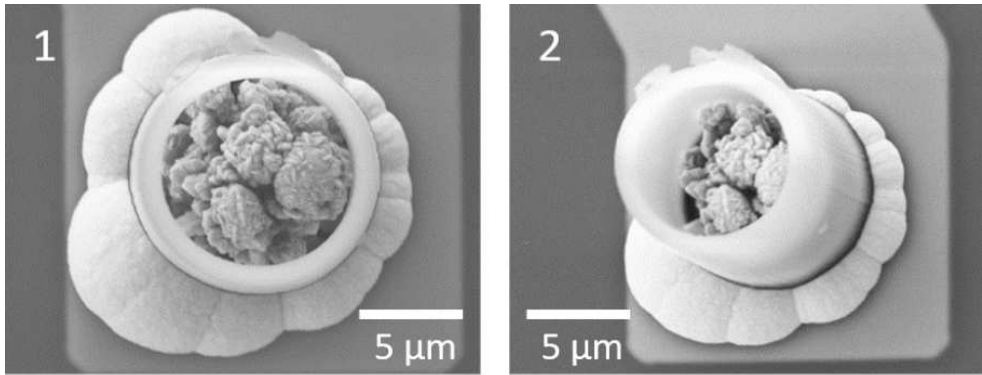


Fig. 40: Scanning electron microscopy images of cylinders with too low adhesion to the substrate. Gold grows not only inside the template but also underneath [77].

In general, there are two possible ways to increase the adhesion. In the first approach the interface area between the structure and the 2D MEA is increased with printing a thin (only $3 \mu\text{m}$ thick) round plate as a base to the pillars. Adding additional printed volume will nevertheless lead to bending of the structures due to increase shrinkage during the developing step. As mentioned in Chapter 4 already shrinkage of the structures occur due to a change in materials properties. The amount of shrinkage is defined by the used printing parameters, the printed geometry as well as the printed material. Since the lower side of the base plate is connected to the 2D MEA surface the usually isotropic shrinkage is restricted at this side. The upper side of the plate can shrink unrestrictedly resulting in a tension and thus slightly curling-up of the structure. The responding physical property is the surface energy. The molecules at the surface have a larger energy than those in the bulk material. The energy difference depends on what the surface is in contact with. In the case of the cylinder structures, the molecules are either in contact with air or the 2D MEA surface. During developing the system will move towards minimum energy and thus will maximize the surface area where the surface energy of the molecules is minimized. Usually air is the medium with lower energy. Therefore, the contact area between structure and substrate is minimized. An easy way to reduce the structure- substrate surface energy is to activate the MEA surface with using oxygen plasma. Unfortunately, this is not enough to get an appropriate surface adhesion. Thus, the approach of adding the base plate only leads to an improved performance if the adhesion between printed material and MEA surface will counteract the mechanical tension due to shrinkage. Therefore, one simple approach is to change

the surface in particular the material used for the passivation layer of the 2D MEA. Usually a stack of Silicon dioxide and Silicon nitride layers coated via plasma enhanced chemical vapour deposition (PECVD) is used as passivation layer (ONONO stack). First experiments show that the adhesion between IP-L 780 and ONONO is not sufficient enough. Therefore, additional layers deposited via atomic layer deposition (ALD) are added on top of the ONONO layer. Aluminium oxide, Titanium oxide as well as Tantalum pentoxide are tested but could not significantly improve the adhesion. As it has been done in Chapter 4 a silanization step is applied which leads to a hydrophobic surface and a chemical bond between polymerized IP-L 780 and the substrate. However this was not enough to obtain sufficient adhesion. The increase in adhesion after the silanization of the ITO coated glass substrates used in Chapter 4 was huge. A possible reason for the low adhesion after silanization this time are the different tested sample surfaces (e.g. ONONO and different ALD layers) which cannot be silanized as effectively as the ITO coated glass substrate.

As a next approach a 2 μm spincoated SU-8 layer (MicroChemicals GmbH, Germany) as passivation is tested. SU-8 is a polymer and apparently forms a strong connection to the polymerized IP-L 780. Figure 41 shows a successful deposition step. Printed cylinders on top of a 2D MEA with a SU-8 passivation can be seen after a gold deposition step was performed. The gold caps at the top of the cylinders indicate a successful deposition step.

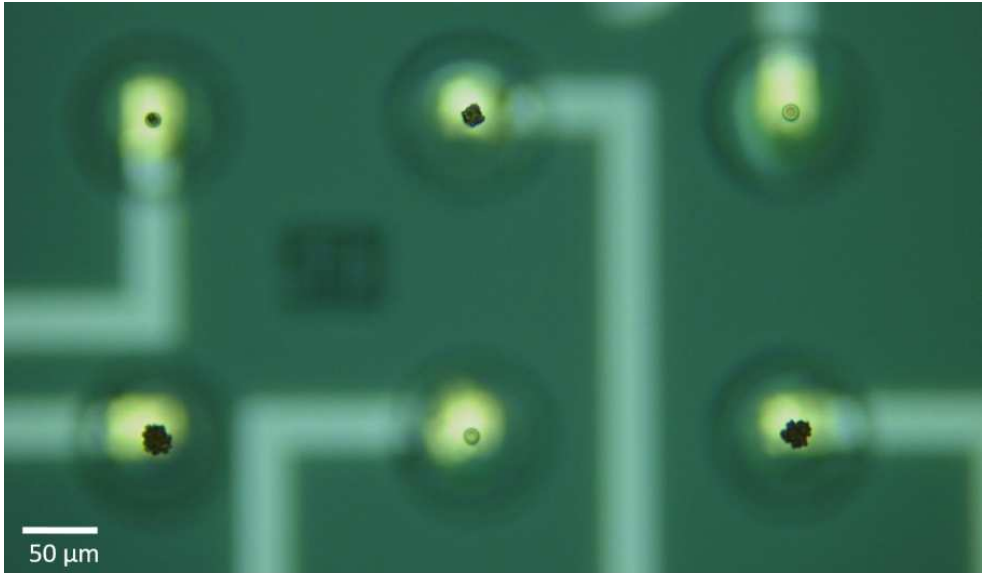


Fig. 41: Light microscopy image of hollow cylinders printed around the electrode openings of a 2D MEA. Gold caps at the top indicate a successful deposition through the cylinders.

The adhesion between SU-8 and the printed IP-L 780 is sufficient to create 3D gold electrodes. Besides the very strong adhesion, spincoated SU-8 as passivation layer has the advantage of having less pinholes than the ONONO passivation. This is of big importance as the gold deposition step is highly sensitive to pinholes. In the presence of pinholes the gold will only grow through the pinholes instead of growing through the cylinders as it can be seen in Figure 42.

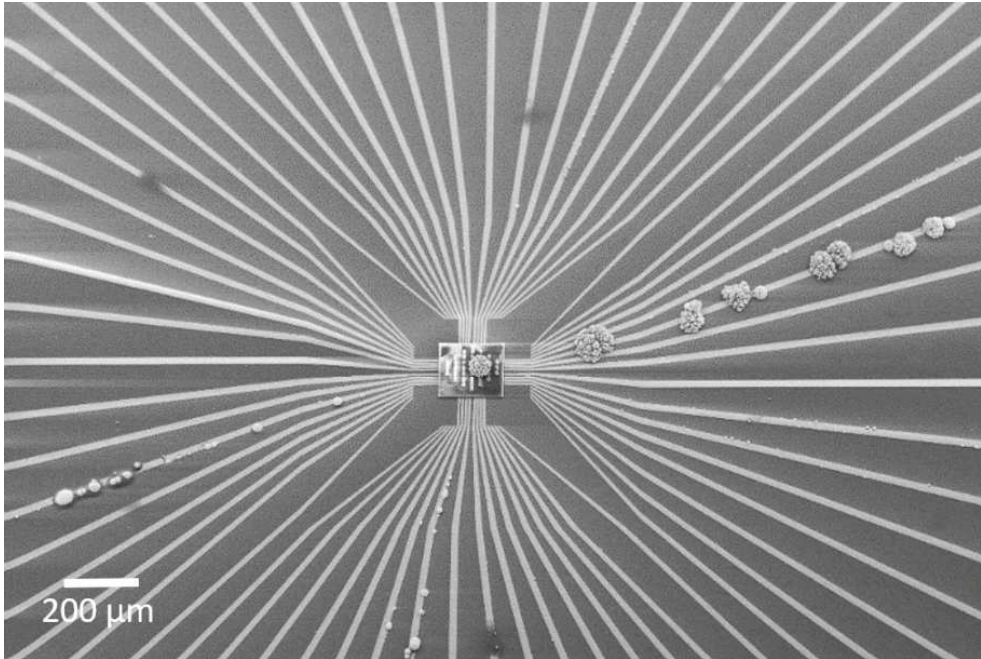


Fig. 42: Scanning electron microscopy image of a 2D MEA after gold electrodeposition. Big gold clumps grew through pinholes in the passivation.

Furthermore, SU-8 is photostructurable and thus no RIE step to open the passivation layer is necessary during fabrication of the 2D MEA device.

To get an appropriate adhesion it is also necessary to start the printing process directly at the MEA surface. The software of the 3D printer has the option of an automatic interface finding. The software checks for a transition between two materials (liquid resin and substrate surface) with different optical properties (e.g. change in refractive index along the optical path). Finding the correct interface is of high importance as already explained in Chapter 4. Automatic interface finding works well for the default resin- substrate combination (e.g. printing on ITO coated glass substrate). Printing on polymer passivations like SU-8 the optical properties are too similar to IP-L 780. That is why the automatic interface does not work in this case. Therefore, the interface has to be found manually. As the 2D device has metal feedline structures the manual approach is done by focusing onto these feedline structures. As the passivation layer is $2\ \mu\text{m}$ thick the focus is set $2\ \mu\text{m}$ away from the feedlines to ensure a print on top of the passivation.

5.1.3 Aspect Ratio Resolution

The aspect ratio (height divided by the outer diameter) of the cylinders is one important parameter to determine the stability of the structure. As mentioned above the 3D print is not limited in height and it is possible to print cylinder with *mm* up to *cm* height. To be able to interact with biological tissue in different depth a high aspect ratio is highly desired. Therefore, it has to be tested which dimensions lead to stable structures. One challenge with high aspect ratio cylinders occurs already during the developing process of the print. During the drying process after the development of the print capillary forces caused by the surface tension of IPA will lead to a bending of the cylinders towards each other [17]. The closer the cylinders with similar heights are printed next to each other the higher is this bending force towards each other. In case the mechanical stability e.g. the bending stiffness of the cylinders is too low to withstand this bending force the cylinders will collapse. With respect to the final application and considering the drawbacks of thicker structures (higher penetration cross-section and lower spatial resolution) cylinders with heights between 40 μm and 500 μm , and different outer diameters, between 3 μm and 12 μm have been printed and characterized to get an idea about their stability. The smaller the dimension of the pillars the smaller the insertion cross section and thus the smaller the tissue damage. Next to the aspect ratio also the wall thickness is an important dimension which restrict the stability. Different wall thicknesses, between 500 *nm* and 2 μm , have also been tested. Figure 43 shows printed high aspect ratio cylinders with thin wall thickness and 150 μm height which collapsed after the drying process.

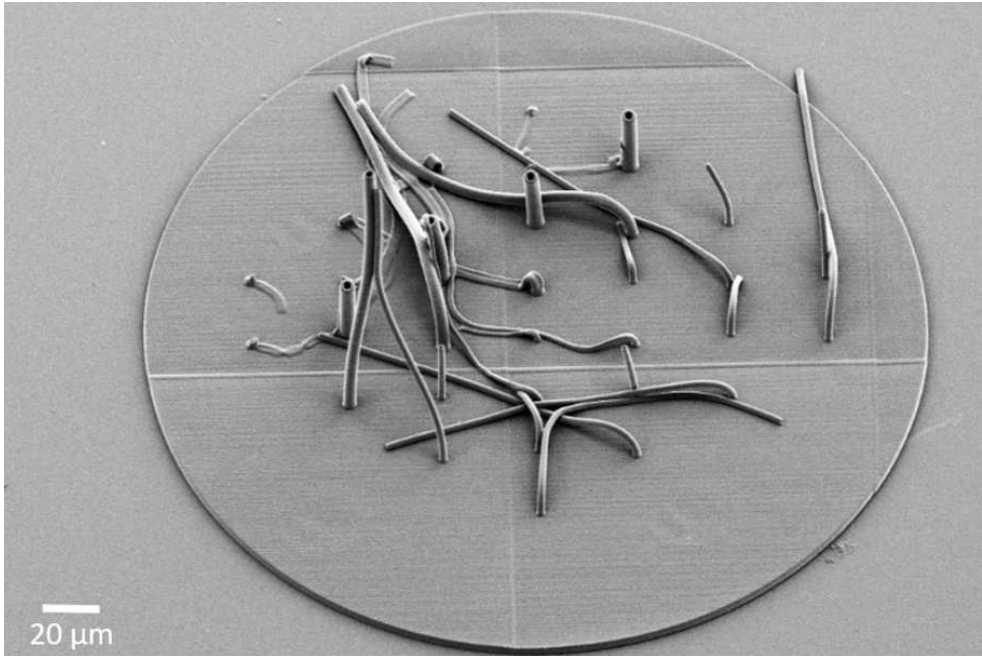


Fig. 43: Scanning electron microscopy image of high aspect ratio cylinders which collapsed during the development process.

The cylinders are printed in close proximity with a distance of $25\ \mu\text{m}$ to stimulate a high density device. For cylinders with $40\ \mu\text{m}$ height they were stable enough to be printed and developed for every tested wall thickness (maximal aspect ratio was around 13 for $40\ \mu\text{m}$ height and $2\ \mu\text{m}$ outer diameter). In comparison, the smallest dimension which lead to stable cylinders with a height of $150\ \mu\text{m}$ were $6\ \mu\text{m}$ outer diameter (aspect ratio of 25) with $1.5\ \mu\text{m}$ wall thickness.

As mentioned above it is possible to overcome the problem with the capillary forces with increasing the distance between the cylinders with similar heights. Thus, designing an array of cylinders with different heights which are close to each other in such a way that cylinders with the same heights are printed apart from each other as far as possible will reduce the problem with collapsing cylinders. Thus a next step the distances between the cylinders are increased to $200\ \mu\text{m}$ to reduce the capillary effect during the development step. Figure 44 shows printed cylinders with heights of $500\ \mu\text{m}$. Five different dimensions, 12/2, 6/2, 6/1, 2/0.5, 4/1, are printed in a 10X6 array. The first number represents the outer diameter in μm and the second number the wall thickness in μm .

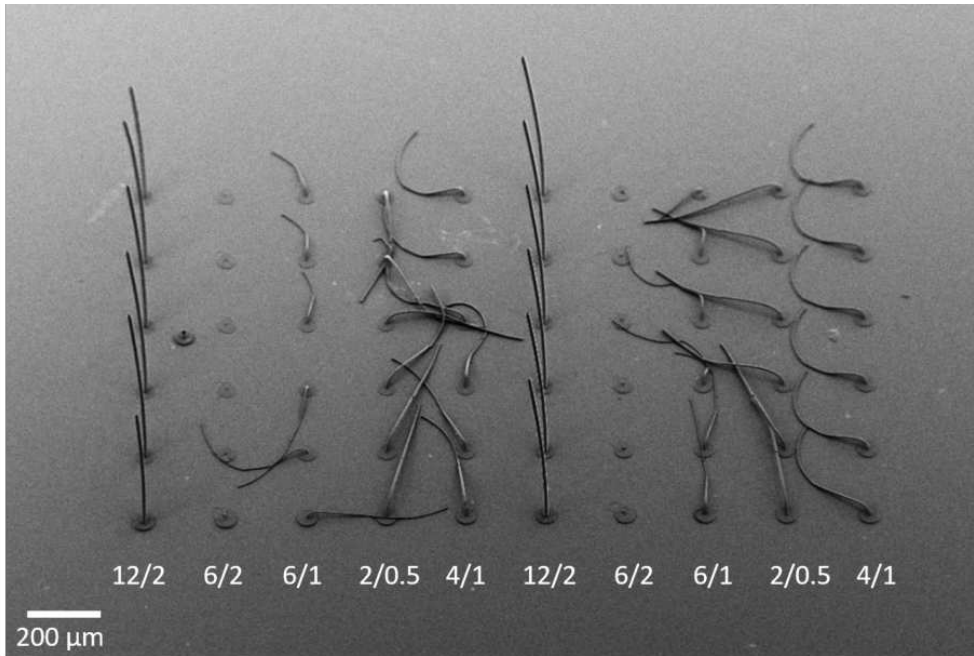


Fig. 44: Scanning electron microscopy image of cylinders with $500\ \mu\text{m}$ height, $200\ \mu\text{m}$ spacing and different outer diameters as well as wall thicknesses. The first number represents the outer diameter and the second number the wall thickness in μm .

As it can be seen only the cylinders with $12\ \mu\text{m}$ outer diameter and $2\ \mu\text{m}$ wall thickness seem to be stable to not collapse. Here the reason for collapsing cylinders is not the capillary force but rather the low effective bending stiffness of the pillars. The aspect ratio is so high, that the structure collapse due to its own weight as well as the medium flow during stage movement and the developing step. Another issue which leads to a decreased stability of high cylinders is the block splitting in z direction. As the objectives (25X and 63X) have a working distance of around $300\ \mu\text{m}$ the cylinders are split into several blocks of $200\ \mu\text{m}$ height to avoid driving the objective into neighbouring structures with heights above the working distance. If in this case the part of the cylinder which is already printed slightly bends to the site the next block is not printed perfectly aligned to the lower one, thus leading to a mismatch which can be seen in Figure 45.

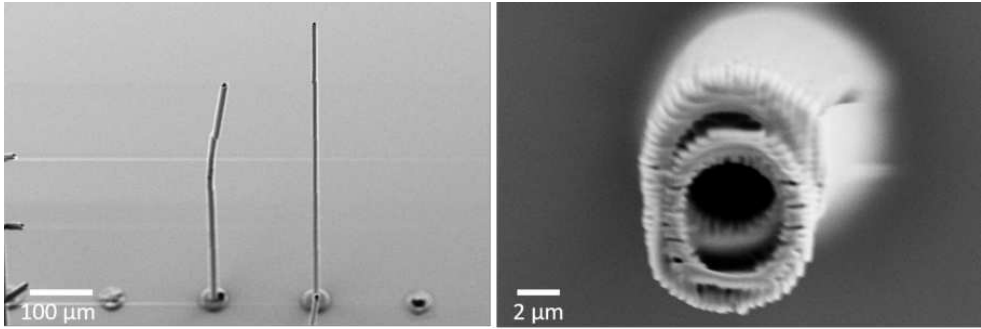


Fig. 45: Scanning electron microscopy images illustrating the challenge of misalignment due to block splitting in z direction. Left: side view; right: top view.

The side view (left image) of a high aspect ratio cylinder as well as the top view (right image) clearly shows the mismatch in alignment of the different blocks. This leads to an unstable cylinder and destroyed template for the electrochemical deposition process. After analyzing the print results for 500 μm high cylinders the wall thickness as well as outer diameters are increased when testing cylinders with 1 mm height. The distance between the electrodes is kept to 200 μm . The outer diameter is increased to 20 μm with a wall thickness of 4 μm . Nevertheless, even the bigger dimensions do not give stable print results. Thus, for cylinders with 1 mm height even bigger dimensions have to be tested in the future. In general it is expected that lower aspect ratios always will lead to more stable print results. Thus, if the tested cylinder dimensions for a given height will lead to a stable print also lower cylinders with the same dimensions are printed well. In this regard Figure 46 shows cylinders with 12 μm outer diameter and 2 μm wall thickness printed with different heights ranging from 200 μm up to 500 μm in an 8X8 array.

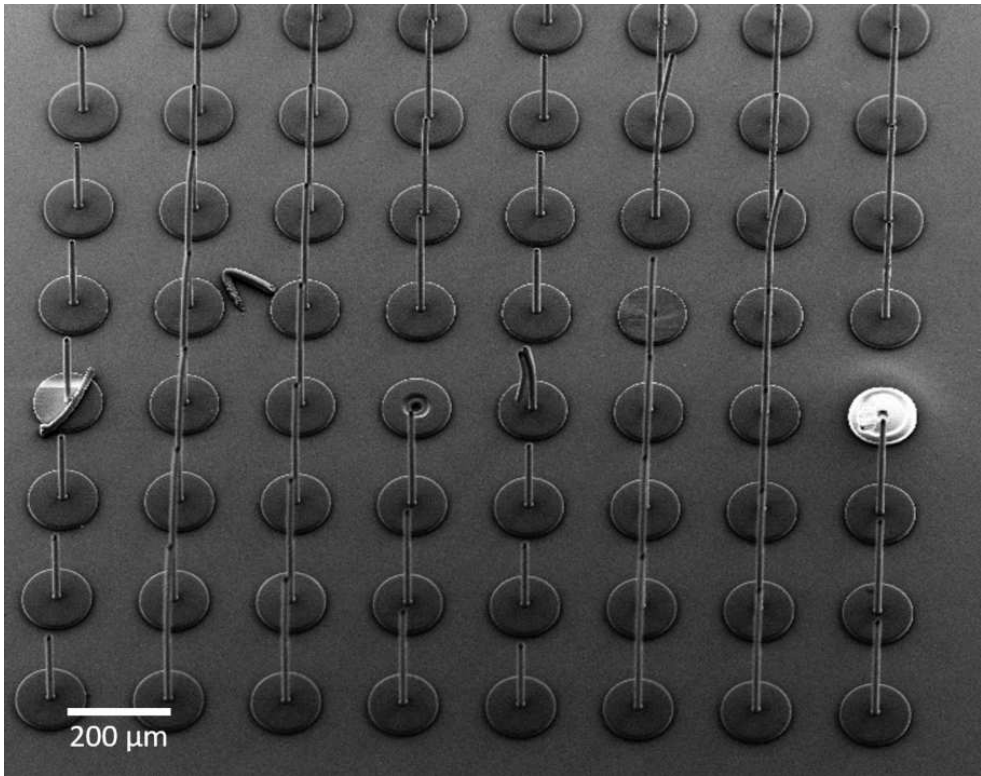


Fig. 46: Scanning electron microscopy image of a 8X8 cylinder arrays with $12\ \mu\text{m}$ outer diameter and $2\ \mu\text{m}$ wall thickness and heights ranging from $200\ \mu\text{m}$ to $500\ \mu\text{m}$.

Only a few cylinders are collapsed after the development which indicates a sufficient stability of the cylinder dimensions. Nevertheless, an optimization of the geometry will lead to a further increase in stability in the future. Possible optimizations are discussed in the following.

A way to increase the geometry dependent bending stiffness of the high aspect ratio cylinders is to use a cone shape structure with thicker diameters at the bottom and thinner diameter at the top. With this approach it is possible to keep the insertion cross section relatively small while at the same time increase the mechanical stability of the cylinders. In general the bigger the cone shape structure the higher the stability but on the other side the higher the insertion cross section. A comparison between cylinders with a smaller cone shape with a diameter of $12\ \mu\text{m}$ at the bottom (left image) and a bigger cone shape with $20\ \mu\text{m}$ diameter at the bottom (right image) is shown in Figure 47.

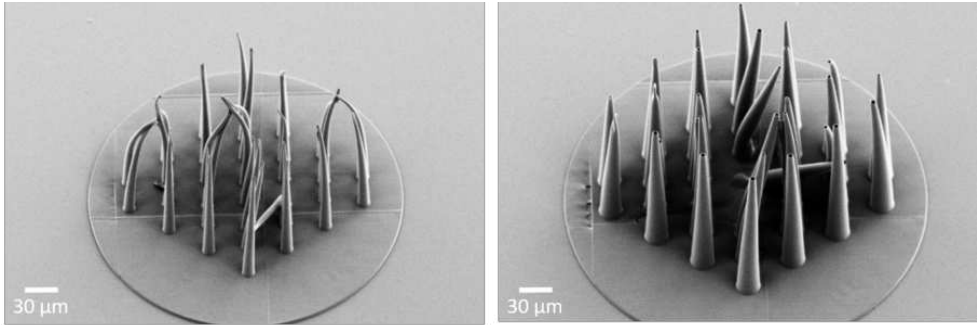


Fig. 47: Scanning electron microscopy image of cone shape cylinder structures with a bottom cone diameter of $12\ \mu\text{m}$ (left) and $20\ \mu\text{m}$ (right). The distance of the cylinders is $25\ \mu\text{m}$ and the height is $150\ \mu\text{m}$.

The cylinders have a height of $150\ \mu\text{m}$ and a distance of $25\ \mu\text{m}$. The dimensions at the top of the cylinders are $2\ \mu\text{m}$ outer diameter and $500\ \text{nm}$ wall thickness. The difference in stability can be clearly seen. Much less cylinders are bended or collapsed using $20\ \mu\text{m}$ diameter at the bottom, although the cylinder dimensions at the top are the same. Especially compared to the cylinders without a coneshape structure the difference is significant. Adding a coneshape structure can thus indeed strongly increase the stability of high aspect ratio cylinders without increasing the insertion cross section too much. To further reduce the insertion cross section another option is to add a cone shape structure which does not continue throughout the whole height of the cylinder but stops at a certain height followed by a constant outer diameter for the remaining height. Besides the cone shape structure another way to increase stability is to add additional wings at the side of each pillar. The design is illustrated in Figure 48.

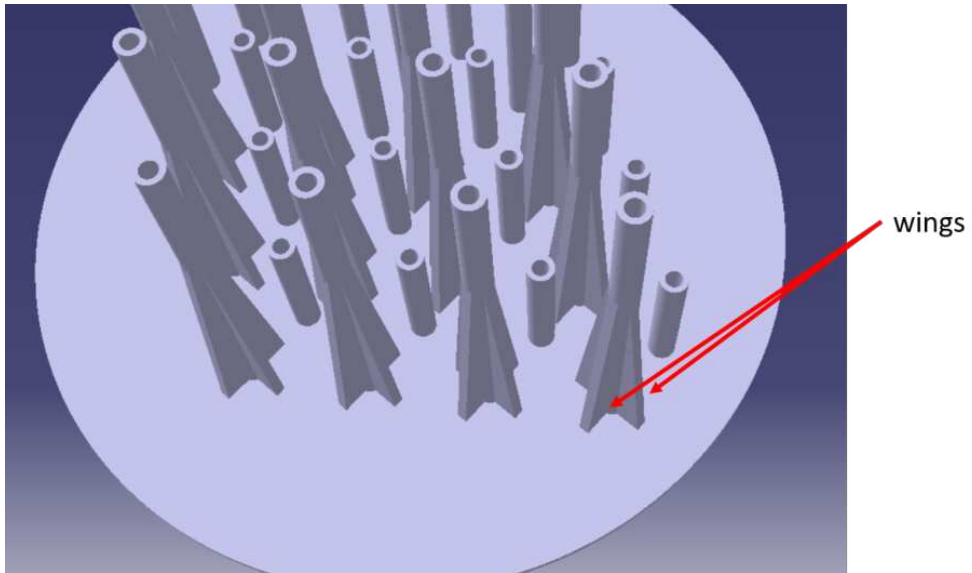


Fig. 48: CAD design of cylinders stabilised by wings to increase the effective bending stiffness.

The wings will lead to a similar stability increase as the coneshape structures but will further reduce the insertion cross section. Size, height and geometry of the wings have nevertheless still to be optimized in the future.

Next to changing the geometries of the cylinders also a change in material properties as well as development process can lead to an increase in cylinder stability and avoid a collapse of the structures. One approach to increase the material mechanical properties is to add an additional UV-exposure step while the structures are still immersed in IPA [17]. This will lead to a further cross-linking of the polymer which increases its Young's modulus.

The use of a CPD as the developing process in contrast can help to reduce the bending phenomena, as it will reduce the capillary forces with slowly exchanging the liquid phase to a gaseous phase [78].

Besides the cylinder stability it is also very important to know how the cylinders behave during tissue insertion. As different kinds of tissues have different mechanical properties different cylinder geometries might be necessary for different tissues. Experiments with phantom tissues like an agarose gel will give a first indication of the penetration behavior for different cylinder geometries in the future. In this regard, adding a tiny tip at the top of the cylinders as an insertion aid might drastically improve the insertion behavior. A

first concept idea of such a structure can be seen in Figure 49.

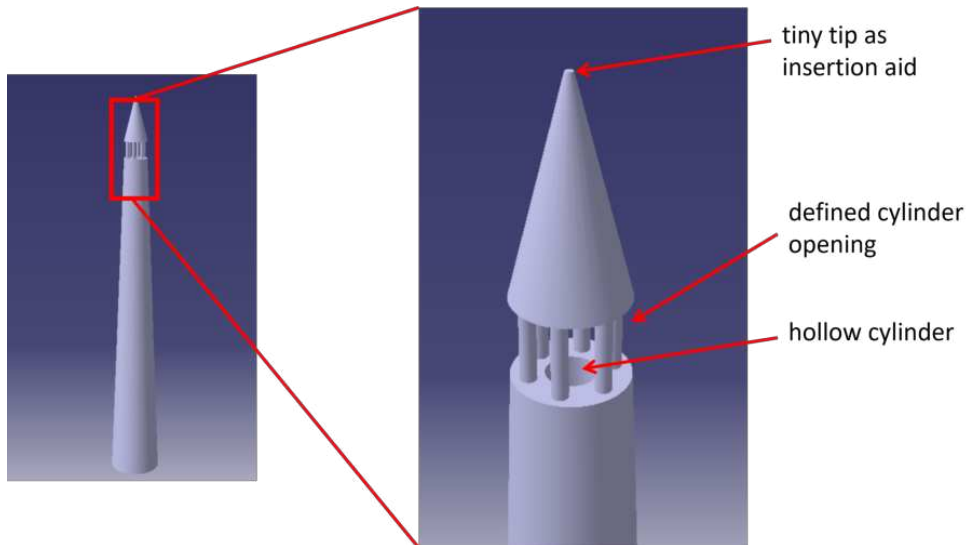


Fig. 49: CAD design of a first concept idea to improve penetration behaviour of high aspect ratio 3D electrodes. The important parts are indicated.

Due to the high resolution properties of the TPP method the tiny tip which acts as insertion aid can be designed and printed with less than $1 \mu m$ diameter. Also the angle of the cone shape tip at the top can be adjusted and optimized. The electrochemical deposition is still done through the hollow cylinder. The connection to the outside is given through the space between the pillars underneath the tip. Height, geometry, thickness etc. of the pillars as well as the opening angle of the cylinder opening can be adjusted. The height along the structure at which the pillars define the cylinder opening can be also varied. In this way printed cylinders with the same total heights but changing cylinder opening height will lead to 3D electrodes with different heights and at the same time improved penetration behavior of the whole implant. Nevertheless it still has to be investigated how the electrochemical deposition works when using the new 3D geometry.

5.2 Towards a 3D MEA device

As a result of the stability tests the further fabrication process has been focused on cylinders of $12 \mu m$ outer diameter and $2 \mu m$ wall thickness. These dimensions are a compromise between stable structures even for higher cylinders (which are necessary to reach a certain depth of the tissue) and high cylinder densities (important to achieve

high density probes) and still achieving a low spatial resolution and small insertion cross sections of the device. For the following fabrication of 3D electrodes several different 2D MEA designs are used.

5.2.1 Stiff Probes

The first MEA design is based on a stiff quartz substrate. SU-8 is used as passivation. The electrodes are arranged in an 8X8 quadratic grid with $200\ \mu\text{m}$ electrode spacing leading to a quadratic sensor area of $1.425\ \text{mm} \times 1.425\ \text{mm}$ as it can be seen in Figure 50.

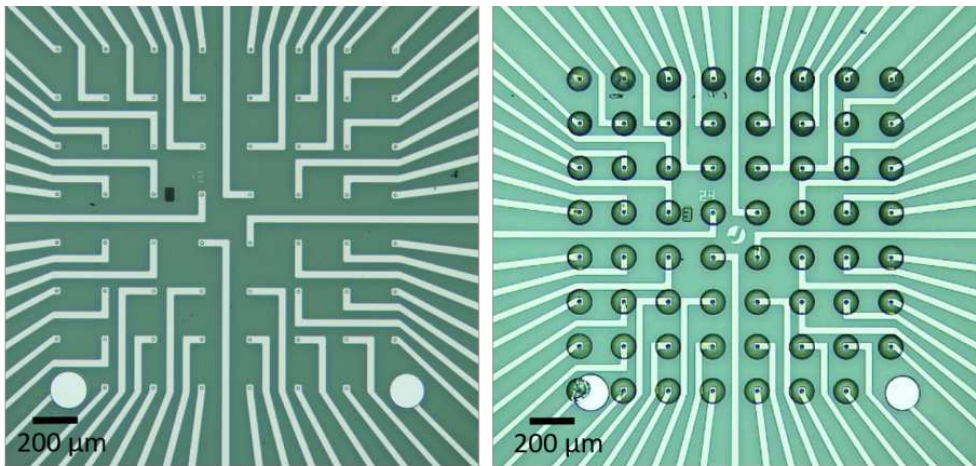


Fig. 50: 2D in vitro layouts. Left: Layout with 64 electrodes arranged in an 8x8 square matrix; right: 3D printed cylinders with different heights around the electrode openings.

The whole process flow can be found in the materials section. Cylinders with different heights are printed around the electrode openings (right image).

5.2.2 Flexible Probes

Next to stiff substrates also flexible substrates with Parylene C as substrate and passivation material is used to fabricate 3D flexible implants. The whole process flow can be found in the materials section. Four different electrode layouts with 16 electrodes and different electrode distances of $106\ \mu\text{m}$, $56\ \mu\text{m}$, $36\ \mu\text{m}$ and $16\ \mu\text{m}$ are used which can be seen in Figure 51.

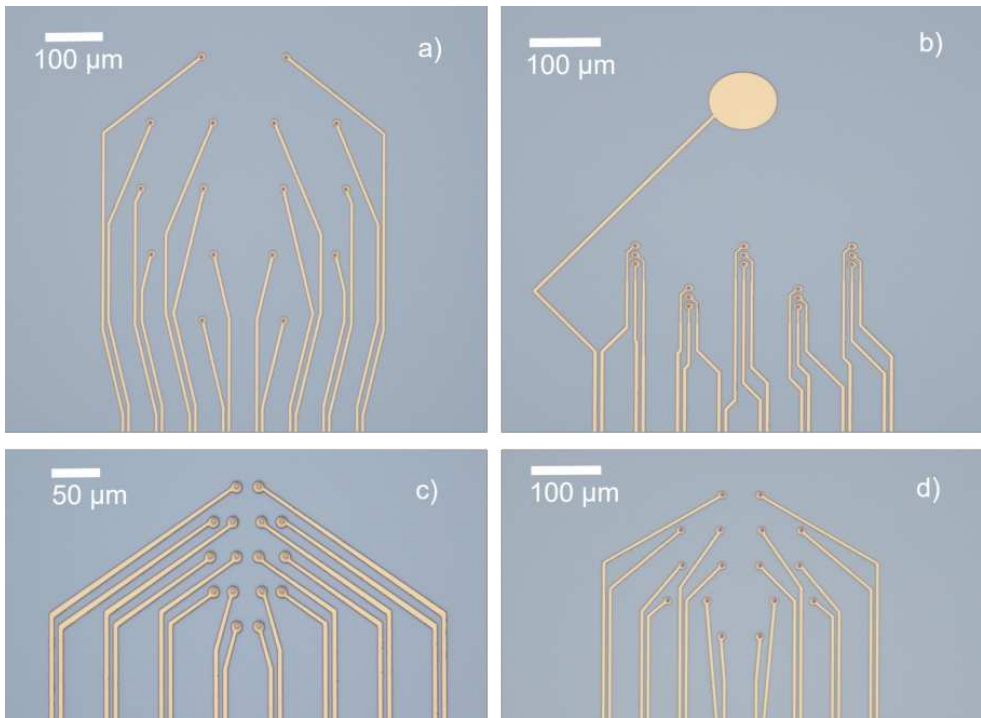


Fig. 51: 2D ex-vivo layouts for flexible implants with electrode distances of $106 \mu m$ (a), $16 \mu m$ (b), $36 \mu m$ (c) and $56 \mu m$ (d).

A special layout which can be seen in Figure 51 b) is called multi-site layout. In this layout three electrodes each are aligned close together with a pitch of only $16 \mu m$ (center to center). Three hollow cylinders with a height difference of only $20 \mu m$ are combined in one structure and printed around the electrodes. This structure simulate a “Michigan”-like array and is used to record the signal from the same active cells but in different depths.

As for the stiff probes, hollow cylinders with different heights are aligned to the electrode layout and printed onto the flexible samples. Figure 52 illustrates design c) with printed cylinders around the electrode openings.

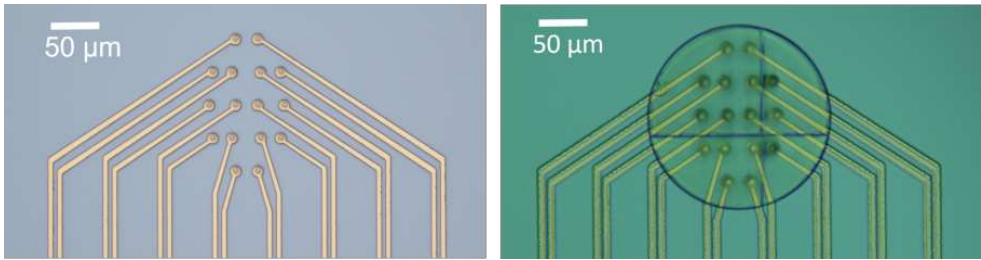


Fig. 52: 2D ex-vivo layout. Left: Layout with 16 electrodes with $36 \mu m$ electrode distance; right: 3D printed cylinders with different heights around the electrode openings (right).

After the printing process the flexible samples are removed from the silicon substrate wafer by adding a drop of water to each sample on the wafer. They are then flip chip bonded onto a printed circuit board (PCB) with connectors for 16 channels. The process is performed on a hot plate at $180^\circ C$. The board is placed onto the hot plate and the low temperature solder alloy Sn42/Bi58 (AMTECH, USA) is applied onto the metal contacts of the board using a syringe. Using tweezers under a microscope, the flexible probes are manually aligned and placed on top of the liquid solder paste bumps, which solidify after removing the probe from the hot plate and cooling it down at room temperature. Finally, the interface between the probe and the electronic board is sealed with a PDMS (mix ratio 1:10) coating cured at $120^\circ C$ for 30 min . Figure 53 shows an example of a chip after microfabrication and packaging.

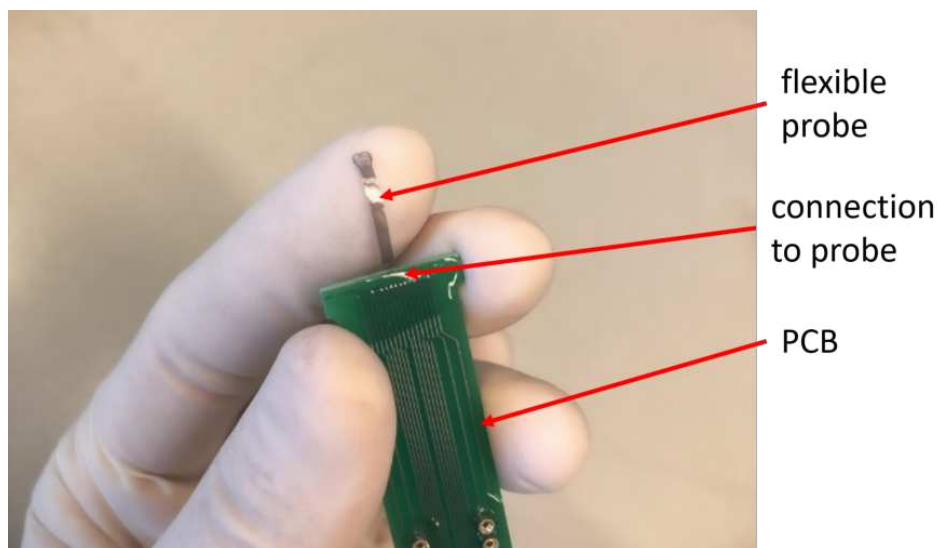


Fig. 53: Image of flexible implant after microfabrication and packaging. The important parts of the implant are indicated.

The use of different layouts and substrate designs of the 2D base MEA shows the flexibility of printing cylinders around the electrode openings. This approach is not restricted to a specific 2D device or layout design. The design and all the structure dimensions in x, y and z can be adapted to the 2D device and its specific application. Cylinders with different and arbitrary heights can be printed within one printing step.

5.2.3 Electrochemical Deposition

5.2.3.1 Gold

To get electrodes with different heights a template-assisted electrochemical deposition step of gold is used. Hereby gold is deposited through the printed hollow cylinders. The cylinders act both as template to direct the deposition as well as passivation of the 3D electrodes which makes this a very easy, flexible and fast 3D MEA fabrication method. For the deposition process a liquid gold bath aqueous solution containing 50 *mM* $AuCl_4$ is used. The standard potential of the electrochemical reaction (Equation (7)) taken from the literature is 0.764 V vs. saturated calomel electrode (SCE) (0.238 V vs. SHE) [52]. Thus, using a silver chloride reference electrode and applying a voltage lower than 0.764 V will favor the reaction's direction towards the solid gold and therefore, gold is being deposited. If a voltage lower than the equilibrium potential of 0.764 V is applied, it is called overpotential. The higher the set overpotential the

faster is the deposition process. In general, there are mainly two limiting factors for an electrochemical deposition process. It can either be charge transfer limited or diffusion limited. For no depletion of gold ions at the metal electrode (usual for small to moderate overpotentials) the growth of solid gold is limited to the charge transfer of the ions through the double layer formed at the electrode-electrolyte interface. In case of high overpotentials the growth is usually limited by the diffusion of the gold ions through the aqueous solution which leads to a depletion of ions at the metal electrode. Those limiting factors and thus the applied overpotential define the morphology of the deposited gold. While a moderate overpotential usually leads to smooth surfaces, a high overpotential results in a dendrite like, coarse growth. To create the 3D electrodes gold is being deposited through high aspect ratio cylinders. Here, the narrow space inside the cylinders limits the volume of gold solution and thus the amount of gold ions close to the electrode surface. Therefore, already for low overpotentials the process is in the diffusion limited stage.

In general, the aim is to fill the cylinders with gold and create a small cap on top of the cylinders. This cap is important to increase the electrode area which is in contact with the tissue and cells. Furthermore, the cap is a 3D electrode environment for the cells which can engulf the cap to establish a tight contact between tissue and electrode similar to e.g. mushroom like 2D+ electrodes [79]. Both properties will increase the SNR during the electrophysiological measurement and the biocompatibility of the device.

Considering previous works [77] for gold deposition a voltage-controlled deposition process with a constant voltage of -1.3 V is used as a first step to fill the cylinders. This rather high overpotential is a compromise between filling the high cylinders in a sufficient amount of time and on the other hand keeping the diffusion limitations to an acceptable value. The measured current during the deposition process is a good indicator for the amount of gold being deposited. The higher the current, the more gold is being deposited. According to Equation (7) 3 electrons are needed to deposit one gold atom. The amount of electrodes per time defines the current. Therefore, the charge (Q) to completely fill the cylinder of a specific height (defined by its volume V_d) can be calculated with the amount of gold atoms N_{Au} which are needed and the molar volume of solid gold ($M_{Au} = 10.21 * 10^{-6}$). The following calculation calculates the theoretical amount of charge necessary to completely fill a cylinder.

$$V_{cl} = \pi * h * r^2 \quad (14)$$

$$n_{Au} = \frac{V_{cl}}{M_{Au}} \quad (15)$$

$$N_{Au} = n_{Au} * N_A \quad (16)$$

$$Q = \frac{N_{Au} * 3}{6.242 * 10^{18}} = I * t \quad (17)$$

In Equation (16) N_A is the avogadro constant and defined as $6.022 * 10^{23}$.

Figure 54 shows an example of a current-time curve for a deposition process through the cylinders. Every single electrode is connected individually to have a better control over the deposition rate for each electrode.

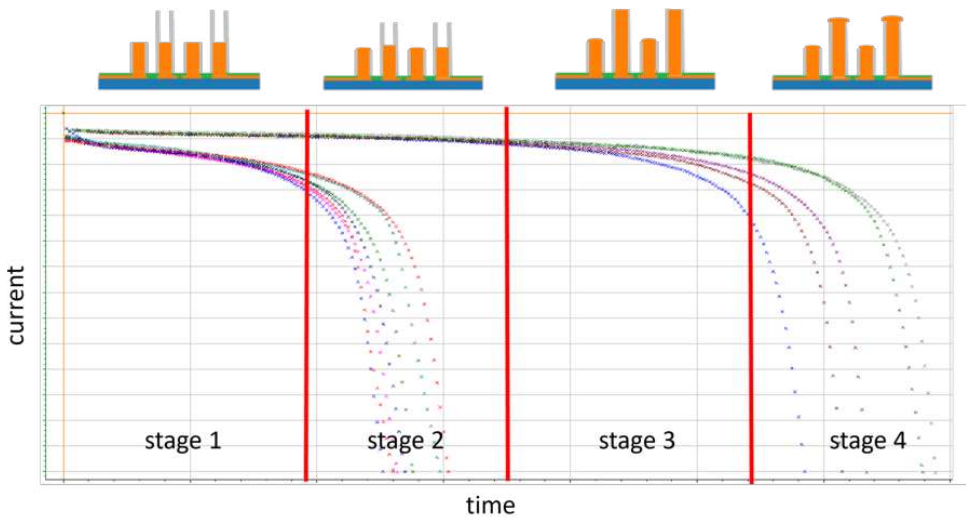


Fig. 54: Schematic view of a current-time curve for an electrochemical deposition process of gold. Four different stages are highlighted with a specific current rate and filling level of different cylinders.

In stage 1 the current is almost constant. During this stage the cylinder is being filled up with gold. As the inner diameter of the cylinders is constant throughout its whole height the amount of gold being deposited is constant. Once the gold reaches the top of the cylinder, the current suddenly raises as seen in step 2 of the graph. To fill

a cylinder in such a way will take around 30 *min* - 40 *min* for 150 μm high cylinders and less time for lower cylinders accordingly. As the gold now reaches 'open spaces' and has contact to the whole bath volume it will start growing in all direction. Because the applied overpotential of -1.3 *V* is quite high the gold will grow fast and in dendrite morphology. This overgrowth can be seen in Figure 55.

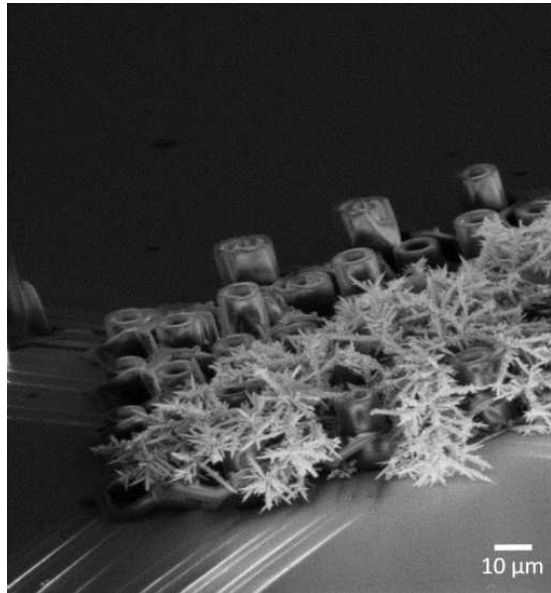


Fig. 55: Scanning electron microscopy image of an dendrite like gold overgrowth which results in a short cut between the single cylinders.

The dendrite like growth has started at one electrode but expanded throughout half of the chip very fast. If this was done for several electrodes they would have not been separated anymore but short cutted. Furthermore, the spatial resolution of each grown 3D electrode is very high in this case. Therefore, it is crucial to control the deposition step in a reliable manner and avoid an overgrowing. One approach to limit the overgrowth is to limit the current. When the current reaches a certain value the deposition process will stop automatically which allows a reliable control. To create a small gold cap on top of the cylinder it is not desirable to have a dendrite like growing as this will automatically lead to an uncontrolled growth of dendrites towards one specific direction rather than to a homogeneous cap. To maintain the advantage of the small size and thus small insertion section of the printed cylinders the grown cap should not be much bigger than the outer diameter of the cylinders. That is why, it is essential to have a good control

over the growth of the cap. To get a sufficient cap size the deposition parameters for creating the cap have to be optimized. Step 3 in Figure 54 illustrates the situation when the deposition at the lower cylinders has been stopped and only the deposition at the higher cylinders continues. In step 4 the gold reaches also the top part of the high cylinders. The difference in amount of flowing current at the beginning in step 1 between lower and higher cylinders is a first indicator for an increase in diffusion limitation for higher cylinders.

Figure 56 shows four cylinders with the same height filled with gold with different cap deposition parameters.

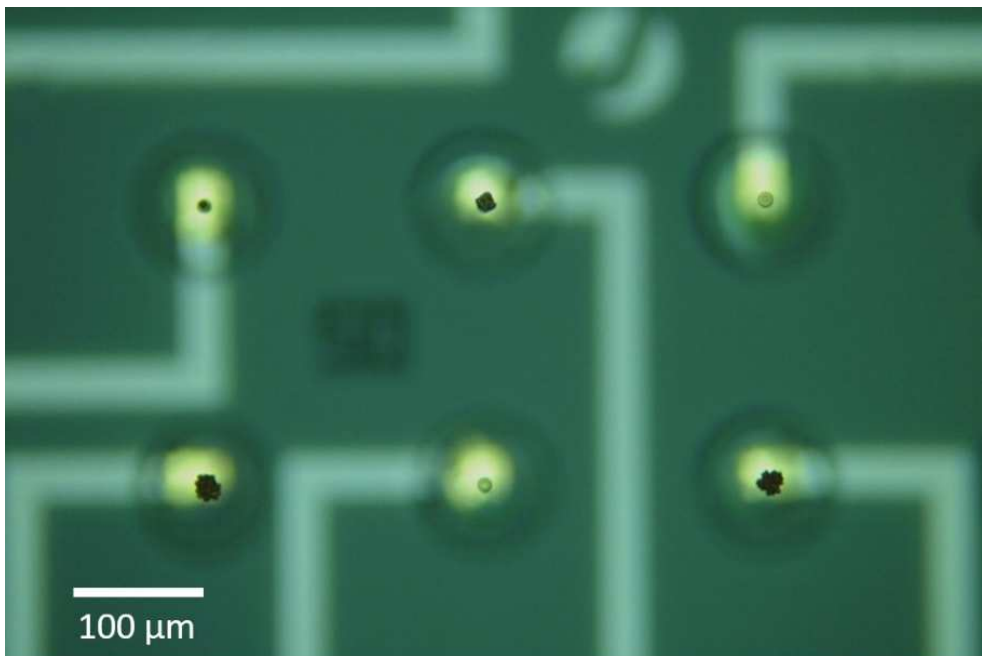


Fig. 56: Light microscopy image of several cylinders with the same height. The different gold cap sizes at the top of 4 cylinders have been achieved with different deposition parameters.

All four cylinders are first filled with gold by applying -1.3 V until -100 nA are reached. No additional deposition step has been applied for cylinder 1 (top left) and thus no cap can be seen as the deposition has been stopped when the gold reached the top of the cylinder. For cylinder 2 (top middle) an additional deposition step has been performed by applying a constant current of -100 nA for 1 min . As it can be seen, the current controlled deposition leads to a homogeneous cap formed at the tip of the cylinder

rather than a dendrite like growth. The cap has roughly the size of the outer diameter of the cylinder. For cylinders 3 and 4 (bottom left and bottom right) the current for the second deposition step was kept to -200 nA for 1 min. As expected more gold has been deposited and the cap size overgrows the outer diameter of the cylinder.

Thus, with an additional current controlled deposition step the cap size can be adjusted to the needs and application. It has to be mentioned that the used deposition parameters were investigated for cylinder outer diameters of $12 \mu\text{m}$ and openings of $8 \mu\text{m}$. If the cylinder dimensions are changed in future also the deposition parameters have to be adjusted according to the new dimensions to create a gold cap with a sufficient height and diameter. Additionally the growth behavior might change for different inner diameters and heights of the cylinders.

To further characterize the deposited gold inside the cylinders and on top of the cylinders SEM investigations are conducted. To be able to get an idea about the gold inside the cylinder a focus ion beam (FIB) is used to cut through it. For that, a filled cylinder is tilted to the side and a cut is applied at different heights of the cylinder which can be seen in Figure 57.

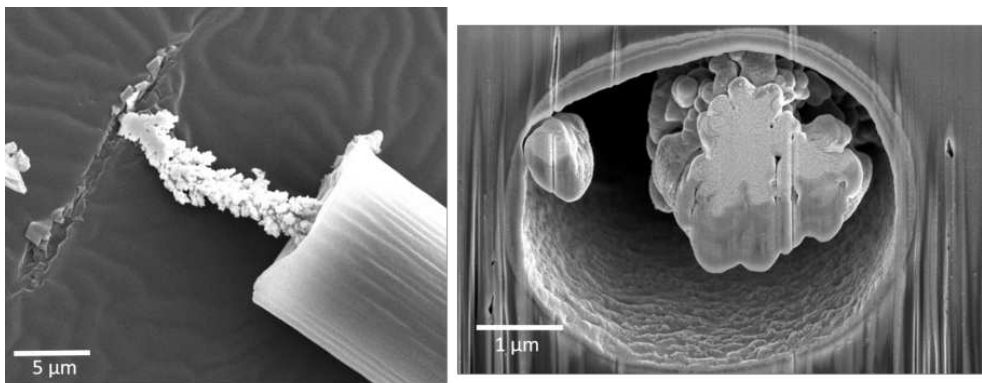


Fig. 57: Left: Scanning electron microscopy image of a filled and tilted cylinder; right: Side view of a FIB cut through a filled and tilted cylinder.

The left SEM image of Figure 57 shows the tilted cylinder. Due to the mechanical force during tilting the gold string has been moved against the cylinder and thus part of it can be seen outside of the cylinder. As expected a dendrite like coarse growth of the gold happens inside the cylinder due to the set high overpotential. Furthermore, the side view of a applied FIB cut (right image) illustrates that the the cylinder is not filled with gold completely but rather only a small string with a diameter of around $2 \mu\text{m}$ to $3 \mu\text{m}$

is grown all the way through the cylinder. The gold string diameter does not change throughout the height of the cylinder. The SEM investigations of the gold string can then be compared to the calculated ones for a given $I-t$ curve of a deposition process. The total amount of charge (Q) which flows during the deposition process is the area under the $I-t$ curve and can be taken from the software. Assuming a homogeneous gold string diameter throughout the whole height and using the calculation which has been shown further above Equation (14) - Equation (17) the estimated string diameter can be calculated and compared to the measured one. Figure 58 shows the calculated gold string diameter values for cylinder heights of $150\ \mu\text{m}$ and $60\ \mu\text{m}$.

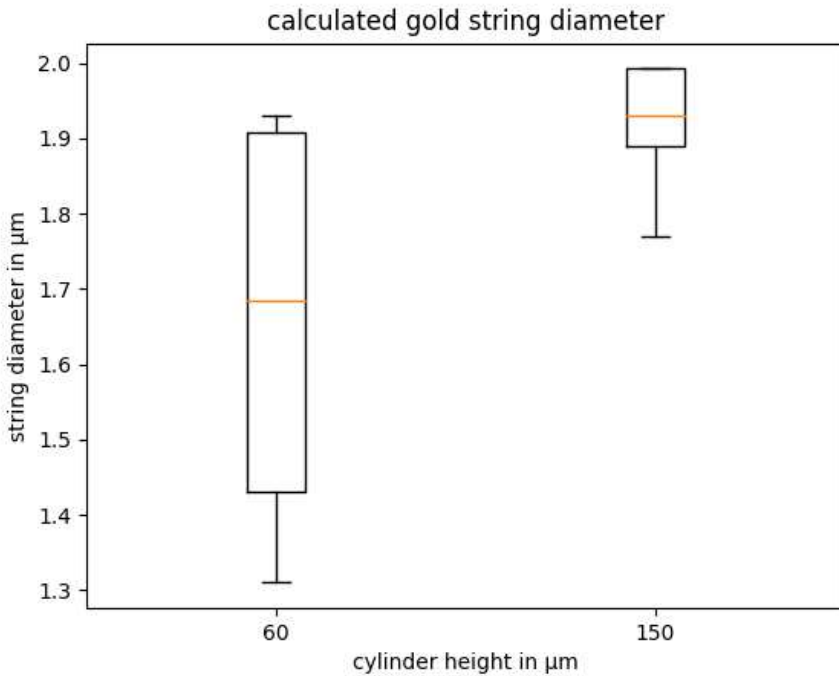


Fig. 58: Analytically calculated gold string diameter for cylinders with $150\ \mu\text{m}$ and $60\ \mu\text{m}$ height.

The calculated string diameter for the $150\ \mu\text{m}$ pillars is in well agreement with the findings during SEM investigations. Considering the fact that the deposition stops at $-100\ \text{nA}$ the string most likely has not yet reached the top of the cylinder. Thus, the height of the string is probably less than $150\ \mu\text{m}$ which will lead to a further increase of the calculated diameter. The same fact is also the reason for the lower string diameter

for the $60\ \mu\text{m}$ high cylinders. As the minimum current of $-100\ \text{nA}$ stays the same for both heights the deposition will stop at the same level below the top of the cylinder. However the percentage of the missing part is higher for the $60\ \mu\text{m}$ cylinder. For example, if the deposition will stop $20\ \mu\text{m}$ below the top of the cylinder the calculated string diameter for the $60\ \mu\text{m}$ pillars will be $2\ \mu\text{m}$ and for the $150\ \mu\text{m}$ pillars $2.1\ \mu\text{m}$.

The gold string acts as the connection between the gold cap on top of the cylinder which is in contact with the tissue and the electrodes of the 2D chip. Thus, further electrical characterizations need to be conducted to ensure the suitability of the small gold string as a proper electrical connection. The gold string in Figure 58 (left) is not broken although the cylinder is tilted to the side which indicates a certain stability of the gold string. In this regard, a stable cylinder will further increase the stability of the gold string as it acts as a protection.

Figure 59 shows a cylinder from the top before and after gold deposition. The small gold cap which is clearly smaller than the outer diameter of the cylinder has been deposited with a second current controlled deposition step with $-100\ \text{nA}$ for $20\ \text{s}$.

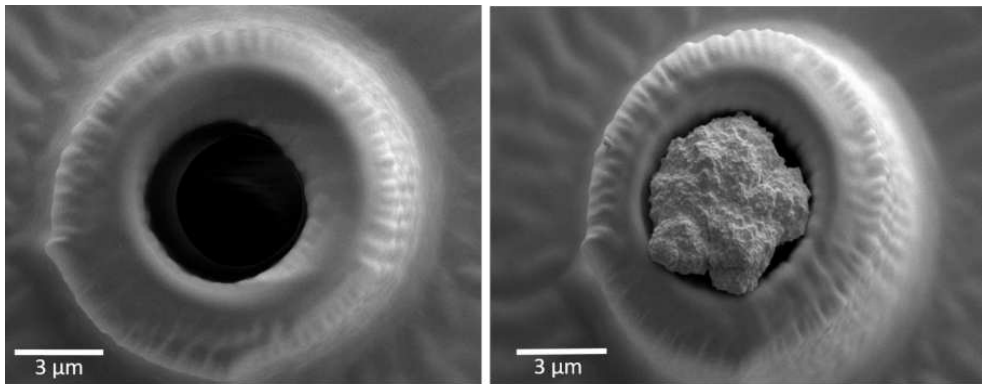


Fig. 59: Scanning electron microscopy top view image of a printed cylinder. Left: Before gold deposition; right: After gold deposition with $-100\ \text{nA}$ for $20\ \text{s}$.

The surface of the gold cap is much smoother than the gold string inside the cylinder, which proves the previous assumption of getting smoother surfaces and controlled depositions when using a current controlled deposition process.

Using the described two stage deposition process it was possible to fill cylinders with up to $150\ \mu\text{m}$ height and $8\ \mu\text{m}$ inner diameter. Figure 60 shows the gold caps on top of $150\ \mu\text{m}$ high stable cylinders using a two deposition process with first applying $-1.3\ \text{V}$ until $-100\ \text{nA}$ is reached followed by applying $-200\ \text{nA}$ for $1\ \text{min}$. This will create gold

caps of around $20\ \mu\text{m}$ diameter.



Fig. 60: Light microscopy image of printed cylinders with $150\ \mu\text{m}$ height. Applying $-200\ \text{nA}$ for $1\ \text{min}$ leads to gold caps of around $20\ \mu\text{m}$ diameter.

In this chapter the template assisted electrodeposition of gold was investigated. Printed hollow cylinders around the electrode openings of a 2D MEA design act like templates to guide the deposition process. To create a suitable 3D electrode a two step deposition process was established. During the first step a high overpotential is used to fill cylinders of different heights. SEM investigations showed that not the whole cylinder is filled with gold but rather a coarse gold string of around $2\ \mu\text{m}$ to $3\ \mu\text{m}$ is being deposited. This is the result of a diffusion limited growth. Calculations considering the total amount of charge during the deposition process match with the SEM findings. To avoid an overgrowth of the cylinder the deposition stops automatically when a minimum current of $-100\ \text{nA}$ is reached. During a second deposition step the current is kept constant at a specific value for a certain amount of time. Therefore, a stable, smooth and controllable

gold cap is grown at the top of the cylinder. Nevertheless, due to the high overpotential of the first deposition step the growth through the cylinders is inhomogeneous and slightly different for all electrodes. That is why also the size and geometry of the caps differ from electrode to electrode even if the deposition parameters remain the same. Further optimization can be done to increase the diameter and homogeneity (along the height of the cylinder as well as between the cylinders) of the string in the future. The diameter and homogeneity of the string is mainly determined by the diffusion limited growth process. Thus, decreasing the overpotential, or using a pulsed method with pulses of certain potential and time followed by a time step without applying a potential to let ions diffuse, may increase the string diameter. Also applying an AC potential might lead to a smoother and thicker string. But it also has to be mentioned that those techniques will definitely lead to significant higher deposition times and might not be suitable considering even higher cylinders in the future. Another way to fasten diffusion kinetics is to increase the temperature and stir the medium while deposition. The use of a higher concentrated gold bath solution will increase the amount of gold ions per volume and also might lead to an improved cylinder filling behavior in the future.

5.2.3.2 PEDOT:PSS

Electrophysiological signals from tissues (brain slice, retina etc.) are usually quite low (only several tenth of μV). Therefore, the noise of the electrodes of the measuring device has to be very low as well to achieve an appropriate SNR. The lower the impedance the lower is the noise and the better is the performance of the electrodes. Thus, to lower the impedance of the 3D electrodes, PEDOT:PSS is additionally deposited onto the gold. This will decrease the impedance by at least one order of magnitude. Suitable deposition parameters have to be found so that the impedance drops significantly and at the same time the cap size is not getting significant bigger, as this will reduce the spatial resolution of the electrodes and increase the insertion cross section of the device. PEDOT:PSS is deposited using an EDOT:PSS solution. Applying a potential to the EDOT:PSS solution triggers the polymerization of the EDOT and thus conductive PEDOT:PSS is being deposited. Based on previous work [80] a constant potential technique (chronoamperometry) is used for the first deposition experiments. A voltage of 1 V is applied for 20 s to deposit PEDOT:PSS on the gold cap. Figure 61 shows a successful PEDOT:PSS deposition.

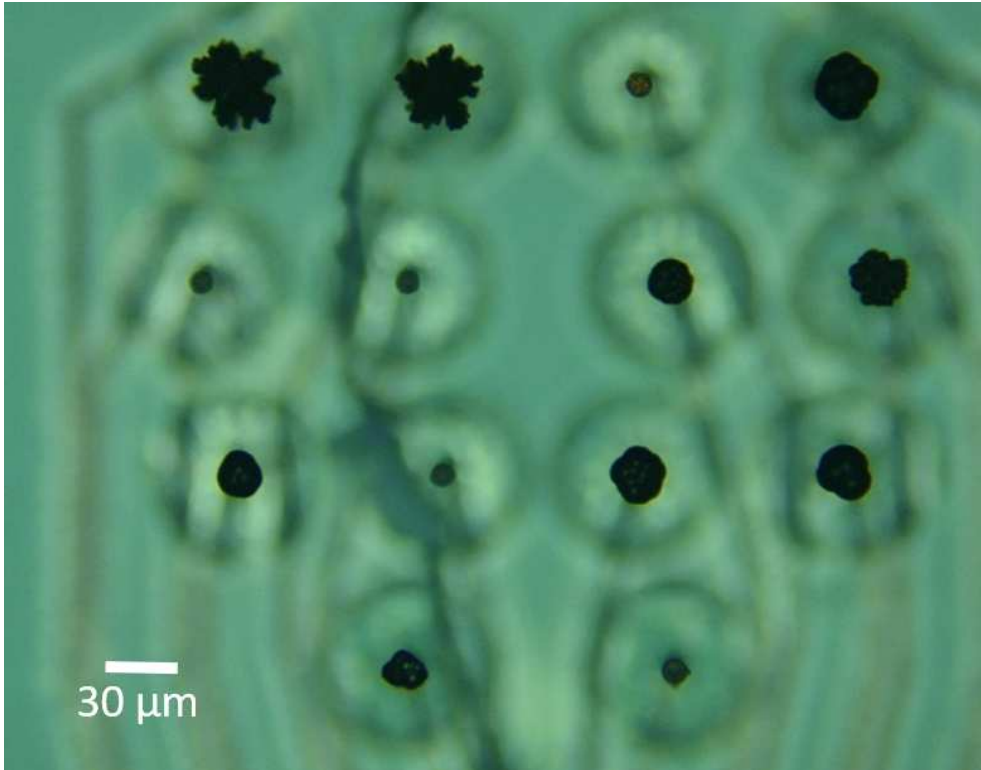


Fig. 61: Light microscopy image of printed cylinders with the same height. The dark caps at the top of each cylinder indicate a successful PEDOT:PSS deposition process.

The change in color (PEDOT:PSS appears dark blue) indicates a successful deposition for most of the electrodes. However, the deposited amount and shape of PEDOT:PSS varies strongly from electrode to electrode. Some of the PEDOT:PSS caps have a nice round shape while others are more rough and dendrite like. In general, the size of all caps are too big and they overgrow the cylinder quite a lot. As the PEDOT:PSS grows on top of the gold cap the deposition strongly depends on the morphology of the gold. A rough or even dendrite shape gold cap will lead to inhomogeneously distributed potential fields when applying a voltage which lead to inhomogeneous growth of the PEDOT:PSS (e.g. the deposition on a dendrite like morphology results in a dendrite like growth). Therefore, it is very important to have a precise control over the deposition process.

Similar to the gold deposition process also for the PEDOT:PSS deposition it is hard to control the growth using a constant voltage pulse. Previous work [81] claims a uniform

and precisely controllable PEDOT:PSS deposition with using CV instead of constant potential techniques. Therefore, a CV technique is used to improve the PEDOT:PSS deposition. The initial voltage is set to 0 V the final voltage is set to 1 V and the scan rate is $0.1 \frac{V}{s}$. The deposition can be hereby precisely controlled via changing the number of cycles. One cycle is defined as the scan from 0 V to 1 V and back to 0 V. To avoid much overgrowing the number of cycles is kept to only 2 at a time. After checking the electrodes with a microscope another 2 cycles are applied to only those electrodes at which not much PEDOT:PSS has been deposited during the first cycles. In such a way, the total amount of cycles can vary from electrode to electrode between 2 and 10 cycles depending on the cap size which want to be achieved. The amount of PEDOT:PSS being deposited during one cycle linearly depends on the amount of flowing current and thus the current is a good first indicator for the cap size. For each additional cycle the current increases. The increase in current happens due to the growing cap size during each cycle and thus increasing electrode area. Thus, each additional cycle will lead to an increase in growth of the cap. Figure 62 shows three cylinders of different heights which are filled with gold using a two step process and deposited with PEDOT:PSS after 5 cycles of the CV technique.

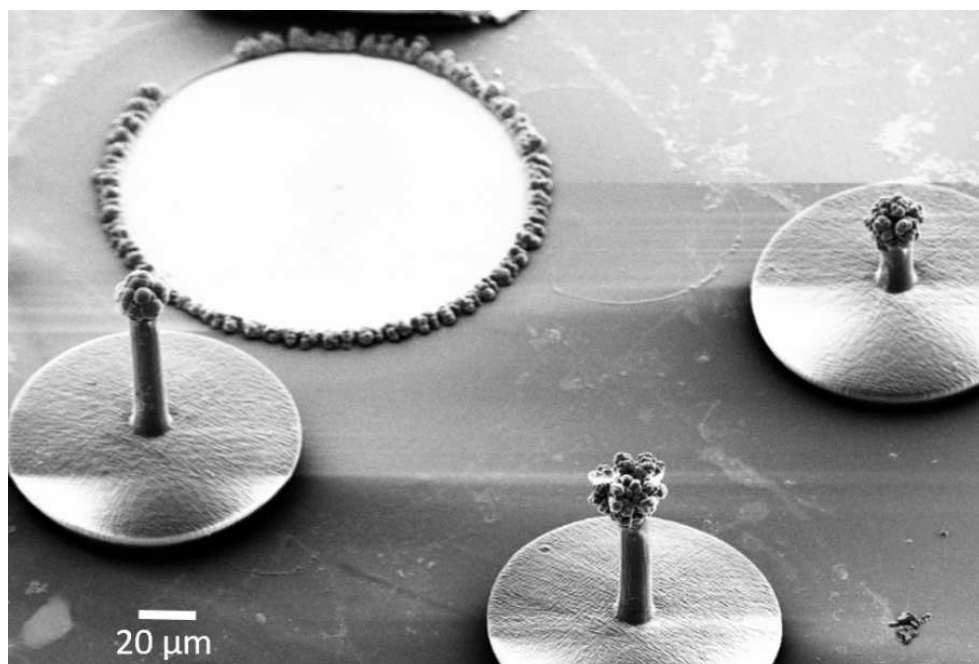


Fig. 62: Scanning electron microscopy image of printed cylinders with different heights with deposited PEDOT:PSS caps after 5 cycles at the top of each cylinder. The big electrode at the back of the image is the reference electrode of the 2D MEA chip.

Due to the additional deposition of PEDOT:PSS the gold cap does not have to be big anymore. Therefore, for the second gold deposition step -100 nA was applied only for 20 s to create a smooth gold surface. The caps achieved after 5 cycles roughly have a diameter of $20\text{ }\mu\text{m}$. Compared to the caps achieved using the chronoamperometry technique the cap size distribution and morphology is much more homogeneous. Figure 63 shows the difference between a grown gold cap and a PEDOT:PSS cap.

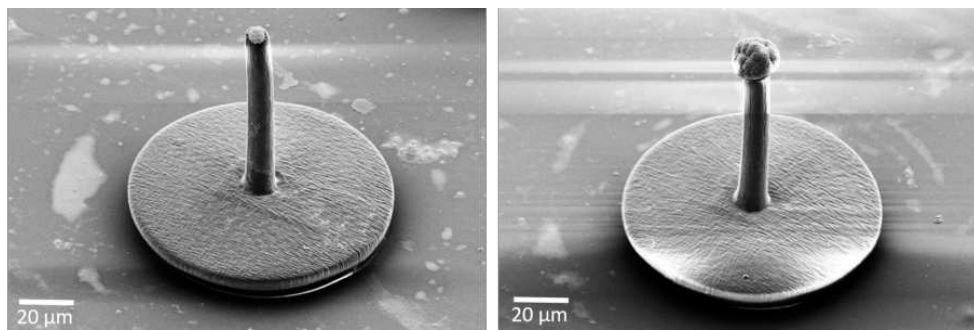


Fig. 63: Scanning electron microscopy image of printed cylinders. Left: Before PEDOT:PSS deposition; right: After PEDOT:PSS deposition.

The cylinder with $100\ \mu\text{m}$ height in the left image is only filled with gold ($-100\ \text{nA}$ for $20\ \text{s}$). At the right image a round PEDOT:PSS cap is added on top.

As mentioned before, the amount of deposited PEDOT:PSS can be precisely controlled with varying the amount of applied cycles during the CV process. While the PEDOT:PSS cap seen in Figure 63 with a size of around $20\ \mu\text{m}$ is deposited after 5 cycles the PEDOT:PSS caps which can be seen in Figure 64 are deposited with applying only 2 cycles.

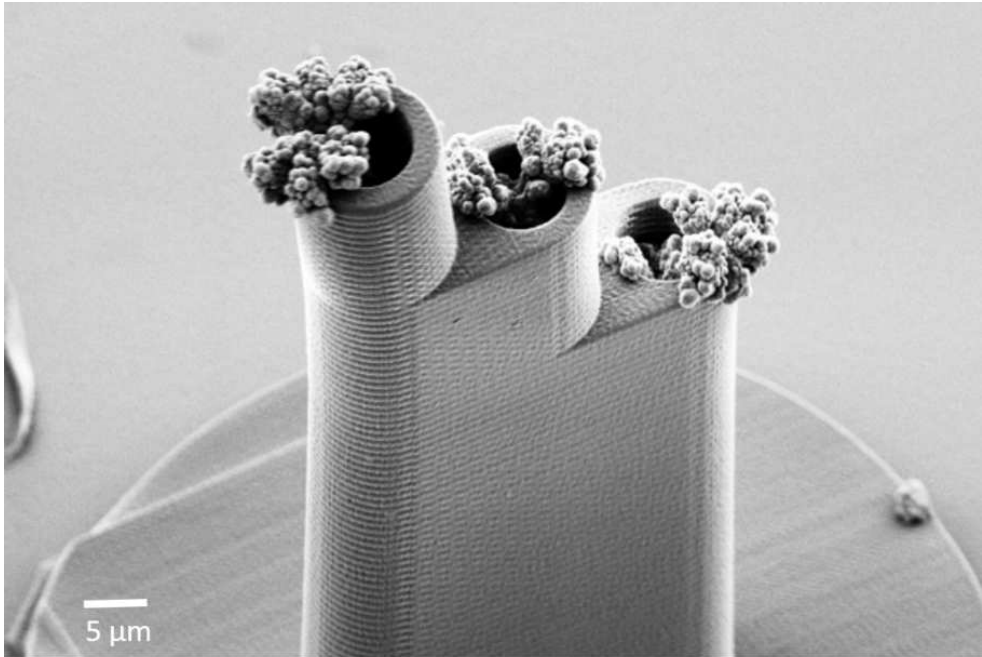


Fig. 64: Scanning electron microscopy image of printed cylinders on a multi-site layout. PEDOT:PSS caps are deposited on top of the cylinders with using 2 cycles of the CV technique.

In the shown multi-site layout (described further above) the electrodes are close together and the cylinders only differ in height by $20\ \mu\text{m}$. Therefore, to not get a short cut between the electrodes the PEDOT:PSS caps have to be small. But at the same time the electrical properties of the electrodes should be sufficient to measure physiological signals from tissue. PEDOT:PSS is not deposited as smooth as for the 5 cycles. A longer PEDOT:PSS depositions seems to create bigger but also smoother cap surfaces. For short PEDOT:PSS depositions in future a slightly longer second gold deposition step to create a bigger smooth gold cap might improve the PEDOT:PSS morphology in this sense.

An electrodeposition step with using an EDOT:PSS solution was introduced to coat the 3D electrodes with PEDOT:PSS to improve their electrical properties. A CV process was found to be suitable to precisely control the growth of the PEDOT:PSS leading to smooth PEDOT:PSS caps. With varying the amount of cycles during the process the size can be adjusted to the electrode design and the application. With adjusting the gold

and PEDOT:PSS deposition parameters it is possible to obtain a certain cap material combination. Especially it is either possible to coat a big gold cap with only a thin layer of PEDOT:PSS or to only create a very small gold cap and add a big PEDOT:PSS cap on top. Both examples will have different electrical properties and mechanical stabilities. A more uniform gold deposition process will unify the PEDOT:PSS deposition. In the future, an optimization of the whole deposition process to optimize homogeneity as well as stability and electrical performance of the 3D electrodes has to be done. The whole deposition process is of course not limited to the use of the described materials like gold and PEDOT:PSS. Also other materials like platinum or IrOx could be used. A complete filling of the whole cylinder only with PEDOT:PSS is another possibility.

5.2.4 Electrochemical Performance

To characterize the electrical performance of the electrodeposited 3D electrodes EIS measurements are conducted. The impedance is measured in a three electrode set up, with an Ag/AgCl reference electrode and a Platinum counter electrode in Phosphate-buffered saline (PBS) which has similar properties than the electrolyte in the human body. To get an idea whether the 3D printing process of the cylinders has an influence on the electrical properties first of all the impedance of the same chip is measured before and after the 3D print. Figure 65 shows no difference in impedance before and after the print.

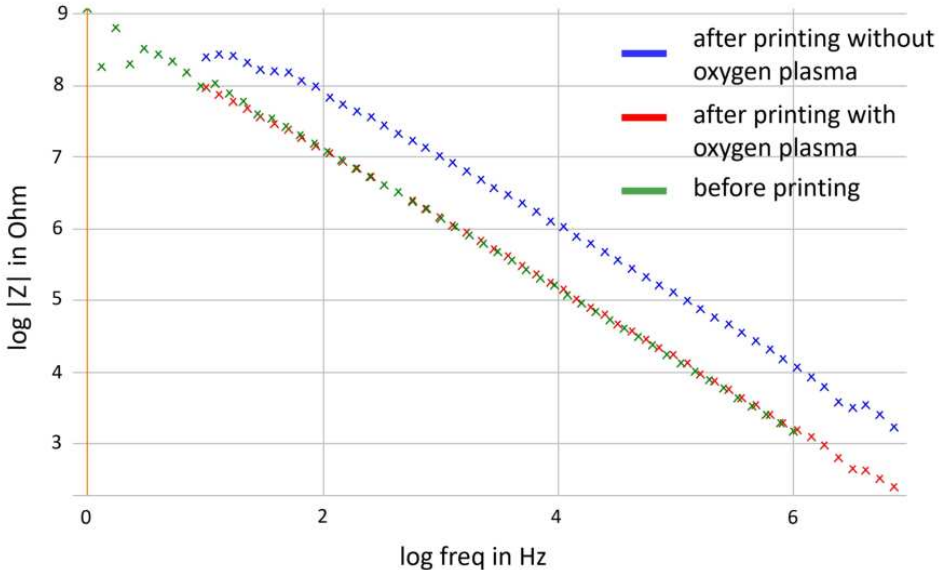


Fig. 65: EIS curve of electrodes before and after 3D printing as well as before and after an oxygen plasma treatment.

As expected the printing process itself has no influence on the electrical properties. The impedance is slightly above 1 MOhm at 1 kHz (a frequency relevant for electrophysiological measurements) which is consistent with previous findings for electrode openings of $10 \text{ }\mu\text{m}$ [22]. As the printed polymer is very hydrophobic it has to be treated with an oxygen plasma step to activate the surface. Only then the electrolyte PBS will enter the hollow cylinders and is in contact with the gold surface at the electrode opening. Without the PBS being in contact with the gold electrode there is no electrical connection and thus the resistance (and therefore the impedance) shows high impedance values for all measured frequencies. As expected the phase shift shown in Figure 66 shows a capacitive behavior (phase shift of -90 degrees) of the electrode-electrolyte interface in the measured frequency regime.

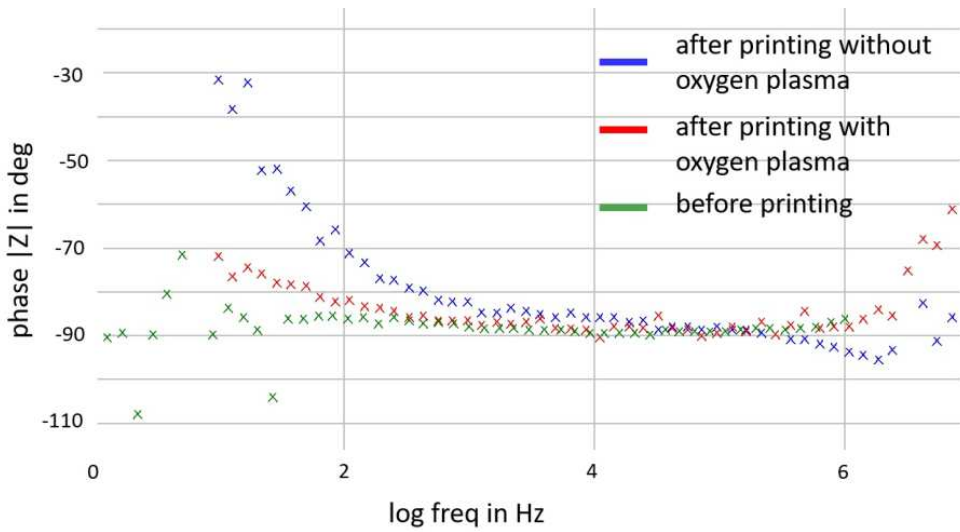


Fig. 66: Phase shift curve of electrodes before and after 3D printing as well as before and after oxygen plasma treatment.

In general, the impedance of the electrode is mainly determined by the electrode-electrolyte contact area. The higher this contact area, the lower the impedance because the capacity of the double layer increases. As analyzed in the previous chapter the size of the 3D electrode strongly depends on the used deposition parameters. Thus, the impedance will mainly depend on the deposition parameters. The following chapter will analyze this influence in detail. First of all the influence of the gold deposition parameters is investigated. For that, Figure 67 illustrates the difference in impedance at 1 kHz for two different gold deposition processes.



Fig. 67: Difference in impedance at 1 kHz for gold 3D electrodes fabricated with applying -100 nA for 20 s and -200 nA for 1 min as second deposition step.

For both electrodes first of all a first deposition step with applying -1.3 V until the current reaches -100 nA is used. For the fabrication of the first electrode -100 nA is applied for 20 s as a second deposition step. The resulting impedance value is slightly higher compared to the 2D 10 μm electrode opening. The reason for that can be seen in Figure 59. Those deposition parameters do not create a real 3D gold cap, where the gold overgrows the cylinder height. The gold just barely reaches the top of the cylinder and thus rather form a 2D electrode with a diameter of 6 μm - 8 μm (the cylinder opening) which is smaller than the 10 μm electrode opening at the bottom and thus the impedance at 1 kHz is higher than 1 $M\Omega$. For the second electrode the second deposition step has been changed to a constant current of -200 nA for 1 min . As shown in the previous chapter this will create a real 3D cap with a diameter of around 20 μm on top of the cylinder and thus to a significant drop of impedance as expected. With controlling the gold deposition parameters, the impedance can thus be precisely adjusted to the needs via the gold cap size.

As mentioned before, measured electrical signals in tissues ex-vivo and in-vivo are

fairly small, therefore to improve the electrical properties of the electrodes an additional PEDOT:PSS deposition is used. This will decrease the impedance of around one order of magnitude [55]. Figure 68 visualizes the difference between 3D electrodes after a gold deposition (left image) and an additional PEDOT:PSS deposition (right image).

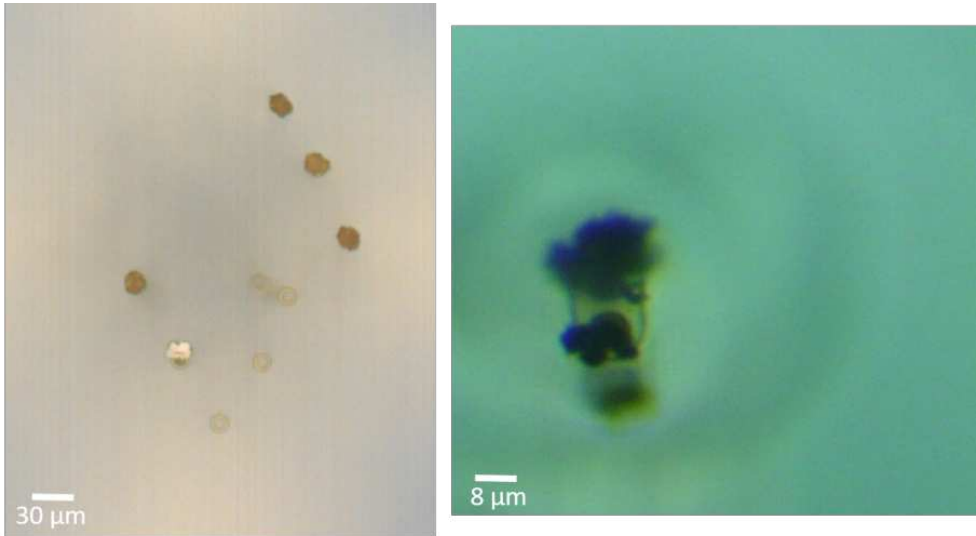


Fig. 68: Light microscopy image of printed cylinders. Left: After gold deposition; right: After additional PEDOT:PSS deposition.

Gold is deposited for $-1.3 V$ until $-100 nA$ is reached and then the current is fixed to $-200 nA$ for $1 min$ (left image) and $-100 nA$ for $20 s$ (right image). Additional PEDOT:PSS is deposited for 2 cycles to the electrodes in the right image. This results in gold cap sizes of around $20 \mu m$ and PEDOT:PSS cap sizes of around $8 \mu m$. Figure 69 compares the impedance values of both 3D electrodes.

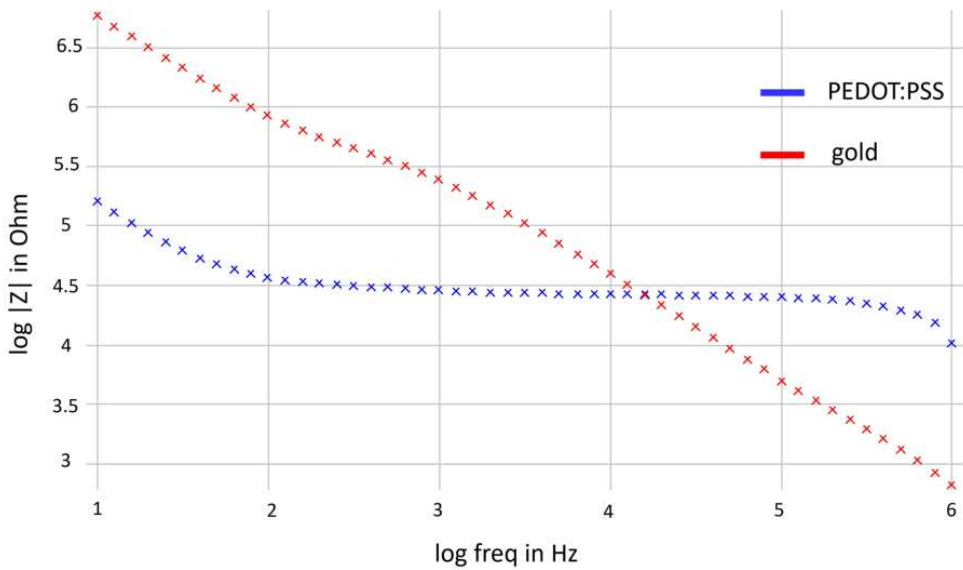


Fig. 69: Comparison of EIS measurements of 3D electrodes deposited with gold and PEDOT:PSS.

Although the cap size and thus the electrode areas is smaller for the PEDOT:PSS electrode it shows a lower impedance of one order of magnitude at 1 kHz . The impedance value of the PEDOT:PSS 3D electrodes between 100 Hz and 100 kHz is around 30 $kOhm$ which fits well with the literature [81]. Also the impedance values of less than 300 $kOhm$ at 1 kHz for the 20 μm 3D gold cap is comparable to previous findings [82].

The phase shift graphs which can be seen in Figure 70 for both 3D electrodes show a deviation from the clear capacitive behaviour which can be observed for 2D gold electrodes. Especially the PEDOT:PSS 3D electrode show a very low phase shift of only -10 degrees between 1 kHz and 100 kHz which indicates a resistive behaviour. The reason for the resistive behaviour is the ionic conductivity of PEDOT:PSS and coincides well with findings in the literature [83][84].

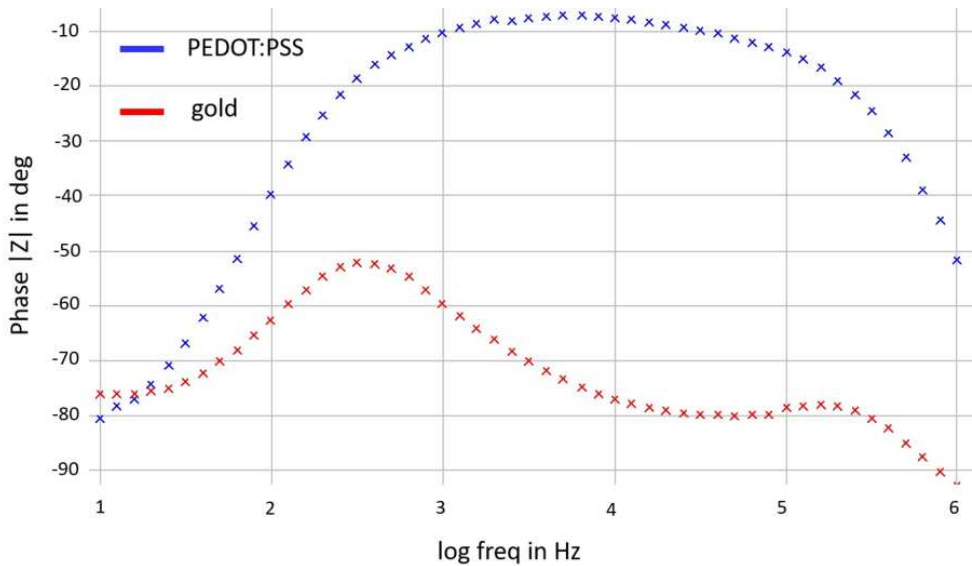


Fig. 70: Comparison of the phase shift measurements of 3D electrodes deposited with gold and PEDOT:PSS.

Using the same idea as for the gold electrodes it is possible to adjust the impedance of the PEDOT:PSS electrodes with changing the deposition parameters, e.g. the number of cycles during CV deposition. Higher numbers of cycles which are applied during the deposition will lead to bigger PEDOT:PSS caps and thus expected lower impedances.

Figure 71 compares the impedances after different number of cycles.

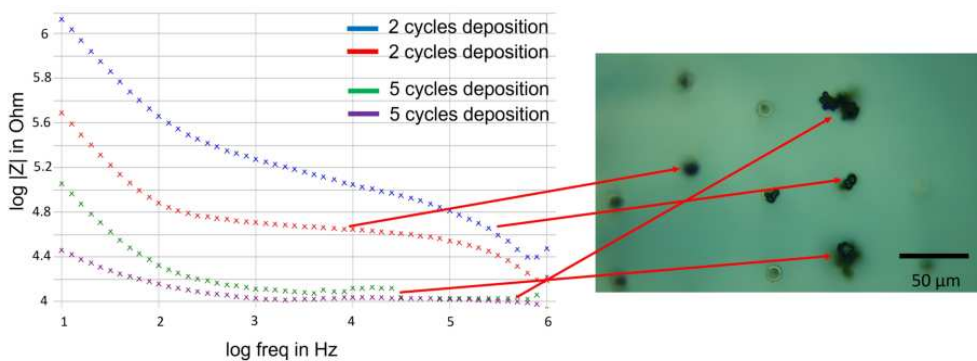


Fig. 71: Left: Comparison of EIS measurements of PEDOT:PSS coated 3D electrodes deposited with different cycle numbers; right: The light microscopy image shows the corresponding cap sizes after deposition.

A big difference in impedance of up to one order of magnitude at 1 kHz can be seen between the illustrated electrodes. The 2 electrodes with the lowest impedance of

about $10\text{ k}\Omega$ at 1 kHz are deposited with PEDOT:PSS for 5 cycles. As for the gold deposition process the amount of current which flows during the deposition process is a first indicator on how much PEDOT:PSS is deposited. The CV curves of the two low-impedance electrodes can be seen in Figure 72.

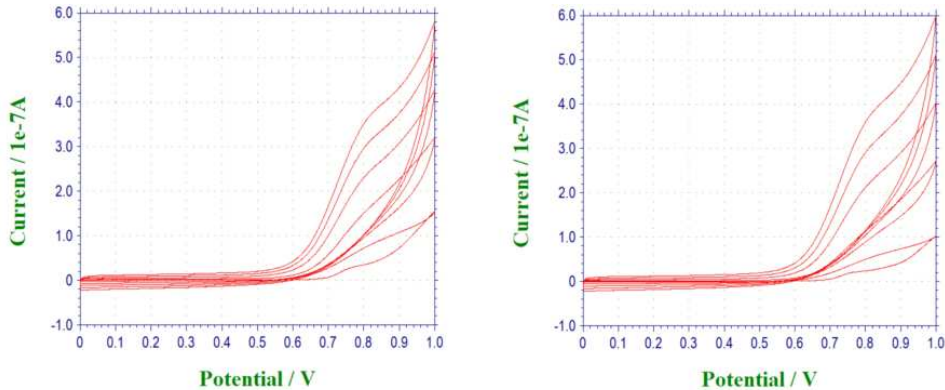


Fig. 72: Current-time curves of a 5 cycle deposition process of PEDOT:PSS. In both electrodes almost the same amount of current flows.

As the amount of current for both electrodes is nearly identical a low impedance difference between them is expected. In contrast the two electrodes with higher impedances show difference impedance values although they both were deposited with 2 cycles. Figure 73 shows their deposition curves.

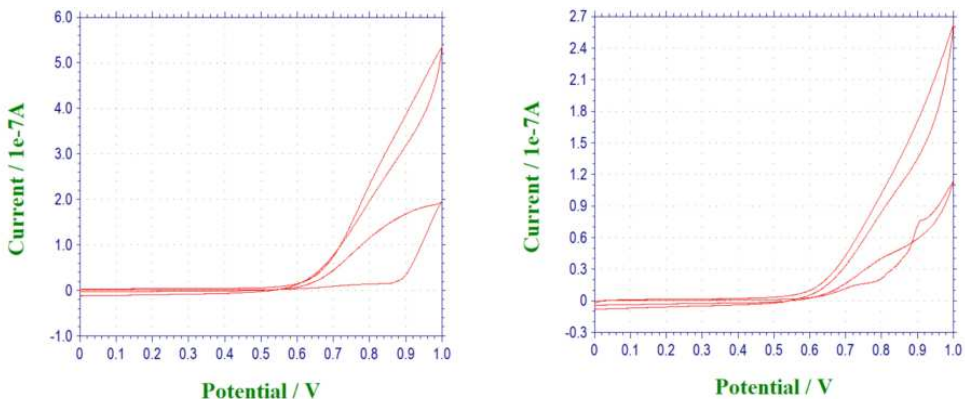


Fig. 73: Current-time curves of a 2 cycle deposition process of PEDOT:PSS. In both electrodes different amounts of current flows.

During the deposition of the left electrode double the amount of current flows compared to the right electrode. This difference clearly reflects the difference in the impedance

values. As expected the electrode with lower current and thus less PEDOT:PSS shows a higher impedance. The light microscope image in Figure 71 also illustrates this behavior. The PEDOT:PSS caps which are deposited with applying 5 cycles are much bigger. To get a deeper inside about the correlation between the number of deposited cycles and the resulting impedance value Figure 74 illustrates the impedance difference at 1 kHz for different numbers of deposited cycles.

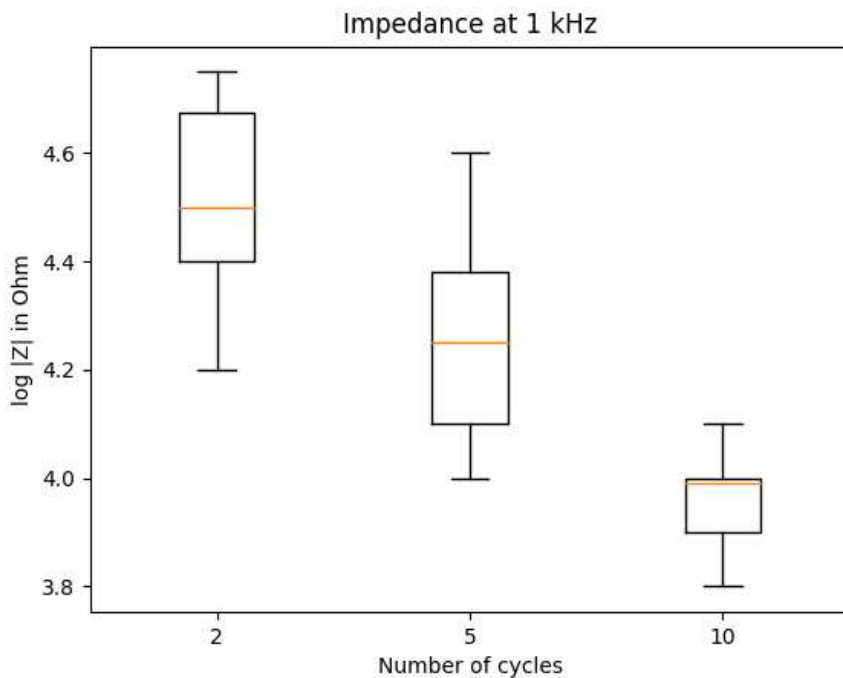


Fig. 74: Comparison of impedance at 1 kHz for 3D electrodes coated with PEDOT:PSS using 2, 5 and 10 cycles.

Although the impedance values varies significantly within the same cycle number, a clear trend can be seen. More cycles will lead to more deposited PEDOT:PSS which reduces the impedance. For 10 cycles the impedance drops below 10 $kOhm$ but on the other side results in large PEDOT:PSS caps which will reduce the spatial resolution of the electrode as well as increase its insertion cross sections. Furthermore, stability issues with big PEDOT:PSS caps are discussed further down.

As a result it can be said that varying the number of deposited cycles for PEDOT:PSS has a huge impact on the impedance of the device which can be expected as with each

cycle number the size of the PEDOT:PSS cap increases and thus the impedance which drops with increased electrode surface is reduced. The size of the PEDOT:PSS cap slightly differs with constant cycle number due to the inhomogeneous gold deposition process. This difference can be already seen during the deposition process when looking at the amount of current. The higher the current (and thus the charge) the higher the amount of PDOT:PSS being deposited.

To sum up, the electrical properties of different 3D electrodes could be successfully characterized using impedance spectroscopy methods. The 3D printing process itself does not have any influence of the electrical properties of the 2D chip. With varying the gold deposition process it is possible to adjust the electrical properties of the 3D electrode. While a short second deposition step after filling up the cylinder will lead to rather high impedance values, longer deposition will lead to bigger cap sizes and thus lower impedance values as expected. To further improve the electrical properties of the 3D electrodes an additional PEDOT:PSS deposition step is applied. Again, the impedance values can be adjusted with varying the deposition process for PEDOT:PSS. A deposition of PEDOT:PSS leads to a drop in impedance of more than one order of magnitude as expected. Nevertheless, the cap size and geometry of the PEDOT:PSS also strongly depends on the initial gold cap geometry. Therefore, an optimization of the combined deposition process will lead to more homogeneous cap geometries and thus even more predictable impedance values.

5.3 Ex-vivo Experiments

After fabricating and characterizing the 3D electrodes as a next step electrophysiological measurements are conducted. To demonstrate the flexibility of the shown 3D electrode fabrication process the measurements are conducted with both stiff and flexible 2D MEA substrates with different designs which have been explained further above. Ex-vivo experiments with rat retina tissue as well as human brain slices shall show the suitability of the 3D electrodes to electrically characterize 3D neuronal tissue.

5.3.1 Flexible Implants

For the implantation of the flexible implants into the tissue a top-down approach has been chosen. Figure 75 illustrates the experimental set up.

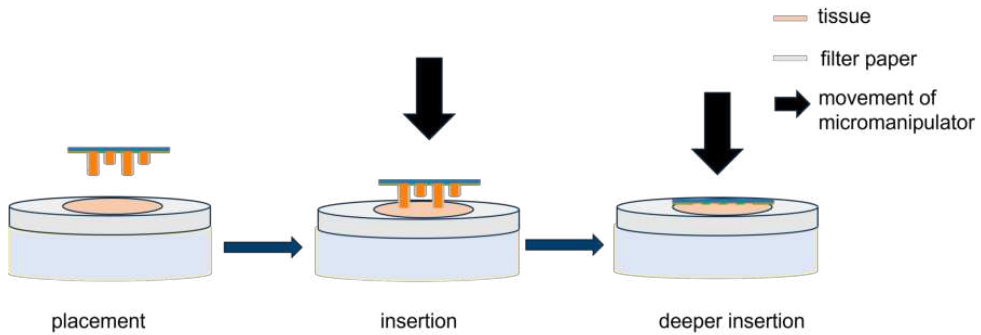


Fig. 75: Illustration of the experimental set up for the top-down approach of flexible implants.

To simulate a proper insertion process the 3D implants are mounted onto a micromanipulator and connected to the Multi Channel Systems headstage. The tissue is prepared and fixed onto a filter paper with a hole in the middle. The tissue is then placed underneath the implant inside a medium bath. With driving down the micromanipulator the implant is lowered towards the tissue. Once the lower side of the implant reaches the tissue with further driving down the micromanipulator the implants starts to bend which leads to a penetration of the 3D electrodes into the tissue. With adjusting the z position of the micromanipulator in the micrometer range the insertion of the 3D electrodes can be precisely controlled. In this way the penetration depths of the 3D electrodes can be adjusted in the micrometer range up to the point where the implant is completely flattened onto the tissue and thus the electrodes are completely inside the tissue. Extracting the electrodes from the tissue works exactly the opposite way with driving the z stage of the micromanipulator away from the tissue. As only the ganglion cells are firing action potentials which can be recorded with the 3D electrodes, the tissue is placed onto the filter paper with the ganglion cell layer (GCL) facing upwards. Figure 76 shows a light microscope image of the set up.

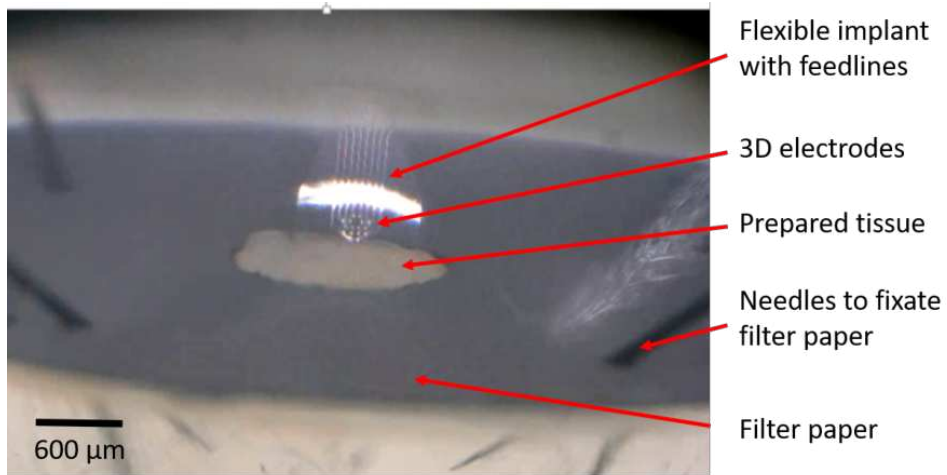


Fig. 76: Light microscope image of the top-down insertion of a flexible implant. The important parts are indicated.

The implant is driven down towards the tissue with coarser steps of $100 \mu\text{m}$ until the highest electrodes start to record cell activities indicating that they have reached the GCL. From this point on the implant is driven downwards with finer steps of only $50 \mu\text{m}$ with a speed of $60 \frac{\mu\text{m}}{\text{s}}$ to monitor the change in signal amplitude and frequency of the electrodes. Steps of $50 \mu\text{m}$ are applied until the implant is flattened onto the tissue and all electrodes penetrate the tissue.

5.3.1.1 Ex-vivo Rat Retina

Figure 77 highlights a monitoring of signals from explanted wildtype rats' retina at different depths inside the tissue.

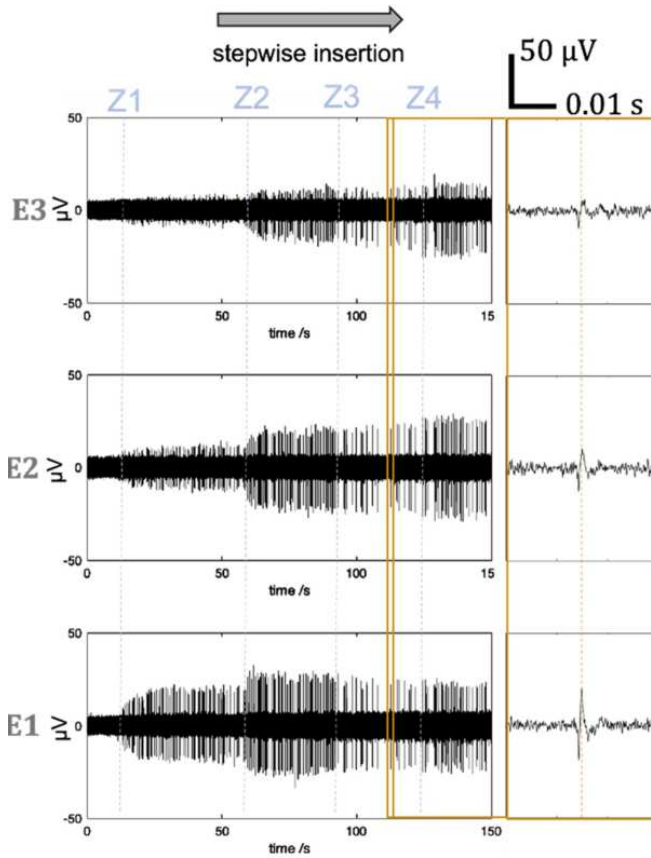


Fig. 77: Recording of spontaneous activity from extracted rat retina tissue with using the multi-site layout at different insertion depths. Due to the short distance of the electrodes they measure the signals from the same cells. The signal changes with stepwise insertion (Z).

The multi-site electrode design is used where the electrodes have heights of $40\ \mu\text{m}$, $60\ \mu\text{m}$ and $80\ \mu\text{m}$. As in this design the electrodes are close together (only $16\ \mu\text{m}$ in x,y direction and $20\ \mu\text{m}$ in z direction) it is possible to measure the same active cell(s) with all three electrodes. This idea will get especially important for future human trials. The retina of patients with degenerative diseases like retinitis pigmentosa or age-related macular degeneration is subjected to a local pathophysiological remodeling of the retinal network after photoreceptor degeneration [85]. Therefore, the multi-site electrode design can then be used to find the most-promising spot (certain tissue depth within the same neural column) for recording and electrical stimulation to be able to tailor the electrode design and position so that they meet the specific requirements for

each individual patient.

In general, action potentials within the retina are only generated by the ganglion cells and thus can be only measured inside the ganglion cell layer and the nerve fiber layer on top. Signals are recorded in all three electrodes. The recorded firing rate in all three electrodes is the same. Furthermore, the AP are being record exactly at the same time for all three electrodes. Both phenomena confirm the expectation that the the same cell(s) are being measured due to the close distance between each electrode. The amplitude however increases during the insertion process and is the highest for the high electrode. The closer the active cell is to the recording electrode the higher is the signal amplitude as the signal decreases in intensity while traveling through the tissue. In this regard the active cell is closer to electrode E1 which has a height of $80\ \mu\text{m}$ and thus sits deeper inside the GCL. The change in signal amplitude during insertion proves the successful penetration of the electrodes into the tissue. It is thus possible to record signals in different depths of the 3D tissue. As the GCL and the nerve fiber layer (NFL) on top have a thickness of around $70\ \mu\text{m}$ [76] it is not expected that even the highest cylinders ($80\ \mu\text{m}$ height) will reach the inner plexiform layer (IPL) underneath the GCL even at complete insertion. And therefore, even at complete insertion signals can be recorded with the highest electrode. For future experiments, higher cylinders can be used for the retina recordings to penetrate through the GCL and reach even layers underneath. In this case the electrodes which penetrate through the GCL will not record any signal anymore [33].

In addition, light stimulation experiments are done to measure the light response of the ganglion cells to check the vitality of the tissue during intraretinal recordings. For that, the retina first rests for about $5\ \text{min}$ in darkness. It then is illuminated with light pulses of $500\ \text{ms}$ every $15\ \text{s}$ to measure the response. As explained in the fundamentals ON-center ganglion cells show an increase in firing intensity during the stimulus whereas OFF-center ganglion cells show an increase in firing intensity after the light stimulus. Figure 78 visualizes the measured response of one electrode inside the retina tissue.

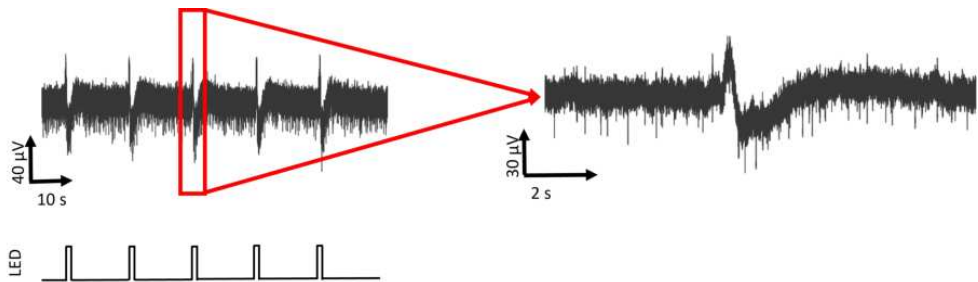


Fig. 78: Recording of cell activities during light stimulation of extracted rat retina tissue.

Light-induced artifacts during each light pulse can be seen. However there is no clear increase in spike intensity during and after the light response and thus the recorded cell could not be stimulated by the light pulses. The measured response of another electrode of the same sample at another position inside the retina tissue can be seen in Figure 79.

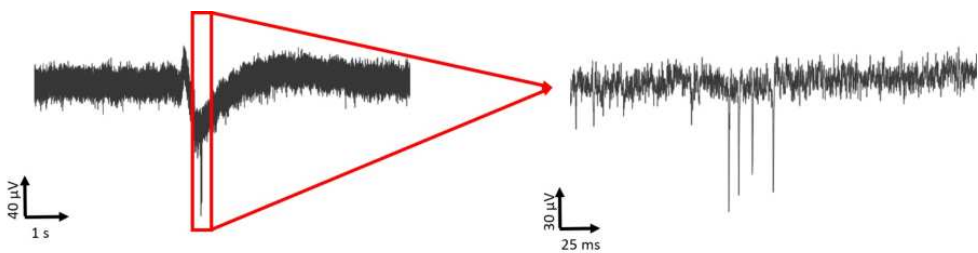


Fig. 79: Recording of light stimulated cells inside an extracted rat retina tissue.

While before and after the light response no spiking activity can be seen there is a clear short burst of spikes right after the light pulse. Apparently, the cells close to this electrode only show activity directly after the light stimulus and thus are OFF-center ganglion cells.

To be sure, that the recorded electrical activities come from active cells within the tissue Figure 80 demonstrates the recording while the flexible implant is moved out of the tissue.

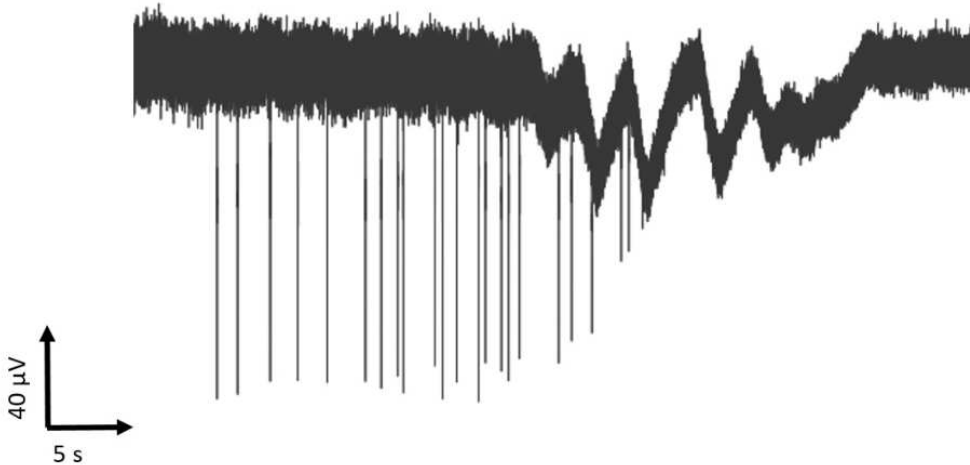


Fig. 80: Recording of spontaneous cell activity from extracted rat retina tissue during the extraction of the implant.

As long as the 3D electrode is still inside the tissue spikes can be recorded. Once the electrode moves out of the retina the spikes disappear. Shortly before the electrode is completely moved out a decrease in spike amplitude can be observed. This is expected as the electrode moves away from the active cell(s) inside the tissue. Like what has been shown further above with the multi-site electrodes.

In general, it was possible to record neuronal signal with a SNR up to 4 and a peak to peak amplitude up to $150 \mu V$. SNRs and action potential amplitudes coincide with findings in the literature for retinal implants with PEDOT:PSS electrodes [33].

5.3.1.2 Human Brain Slice

Next to ex-vivo rat retina experiments also human brain slice experiments are conducted. The brain slices are prepared by the Uniklinik RWTH and have a thickness of around $300 \mu m$. The insertion is done exactly the same way as for the retina experiments with driving down the implant into the brain slice. Figure 81 shows the recording of action potentials in different depths of the tissue.

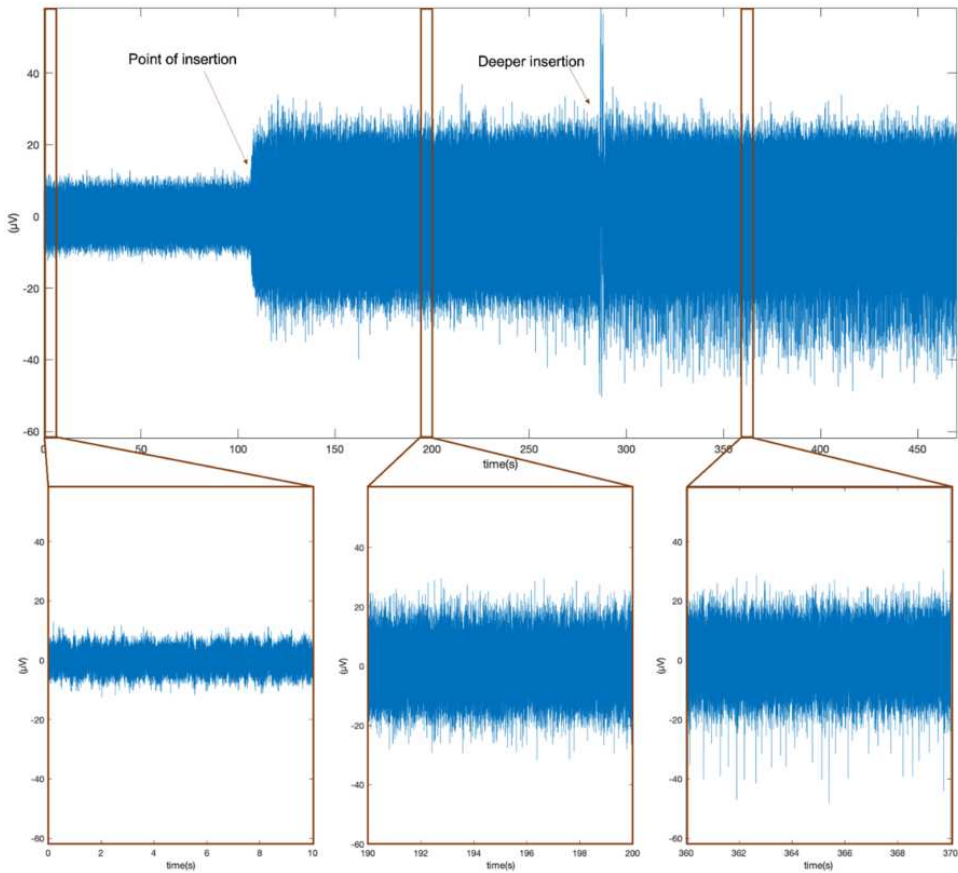


Fig. 81: Recording of spontaneous activity from human brain slices in different depths. Before the point of insertion, no signals can be recorded.

At the beginning of the recording the 3D electrodes are still outside of the tissue and thus no tissue activity can be seen. With further driving down the micromanipulator the electrodes start to penetrate into the tissue (point of insertion). This can be seen with an increase in noise level due to the increase in tissue impedance. Already some small amplitude spike activities can be recorded. The amplitude of the spikes increases with driving the electrodes deeper into the tissue (deeper insertion) as the electrodes get closer to active cells. In this way amplitudes up to $50 \mu V$ could be recorded from human brain slices at different depths of the tissue. Nevertheless, only few and small signals could be recorded and thus, for a deeper analysis of the suitability of the 3D electrodes to measure signals in human brain slices more experiments need to be conducted in

the future.

Using flexible 3D implants it was possible to record spontaneous and light stimulated cell activities from human brain slices as well as retina tissue ex-vivo. The 3D implant was driven into the tissue using a micromanipulator. This way the 3D cylinders could easily penetrate the tissue. Even after multiple insertions the tissue was still active and not destroyed. Especially the multi-site design demonstrated the ability to record signals in different depth of the tissue up to 120 μm . More experiments have to be conducted in the future for a deeper analysis of network behavior in different depths as well as tissue stimulation. Furthermore, the electrode distance (for insertion stability as well as signal recording), electrode heights as well as cylinder dimensions (diameters) have to be optimized. As different tissue has different properties all the electrode dimensions have to and can easily be adjusted to the specific application. In addition, a deeper electrical analysis (e.g. CSC) of the 3D PEDOT:PSS electrodes has to be conducted to test their suitability for electrical stimulation of the tissue.

5.3.2 Ex-vivo Rat Retina with Stiff Probes

Next to the recordings of flexible samples also stiff 3D MEAs can be used to record ex-vivo tissue. Cylinders with 12 μm outer diameter, 2 μm wall thickness and 40 μm – 110 μm height are printed around the electrodes. The cylinders are filled with gold and the 3D electrodes are coated with PEDOT:PSS to increase the electrical performance. In contrast to the experiments with flexible probes where they are driven into the prepared tissue from the top, in the case of stiff MEA samples the tissue is placed on top of the 3D electrodes and pushed into the 3D electrodes with using weights and a micro needle which is connected to a micromanipulator (bottom-up approach). The 3D MEA is connected to a BioMAS headstage which is explained in the materials section. Figure 82 illustrates the experimental set up.

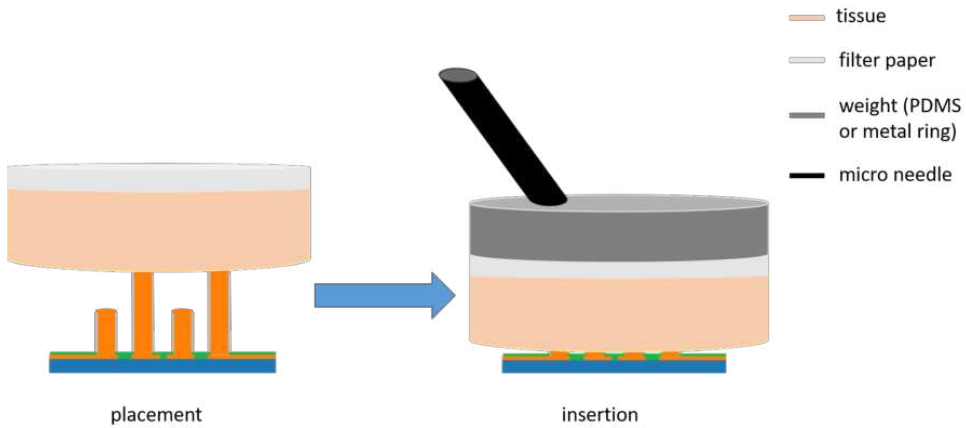


Fig. 82: Illustration of the experimental set up for the bottom-up approach of stiff probes.

In practice, it is much harder for the 3D electrodes to penetrate into the tissue with the bottom-up approach than it was with the flexible approach where the electrodes were actively forced to penetrate the tissue with driving the probe down. The retina tissue is very light and flows away as soon as the medium is added. Therefore, to improve the penetration of the 3D electrodes the extracted rat retina tissue is placed on a filter paper and then on top of the 3D electrodes (with the filter paper pointing upwards) in a dry condition to avoid floating of the tissue. Before adding the medium a small PDMS or metal ring is placed onto the filter paper to ensure enough pressure for penetration. Finally the medium is added with the idea that once the 3D electrodes have been penetrated the tissue they will fix the tissue. Finally, additional pressure is applied using a micro needle which is fixed to a micromanipulator and driven onto the filter paper. In this way it was possible to record signals from extracted rat retina tissue which is shown in Figure 83.

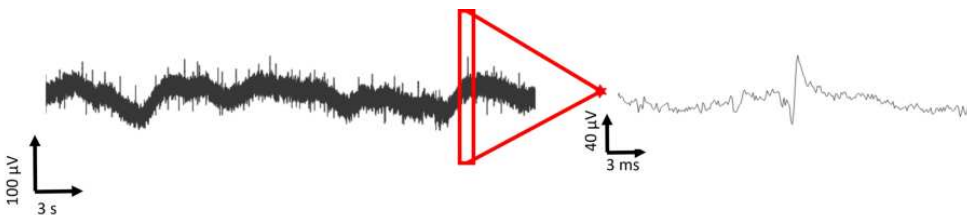


Fig. 83: Recordings of spontaneous cell activity within an extracted rat retina tissue after placing the tissue on top of the 3D MEA.

Spikes can be seen throughout the whole recording. A zoom into one of the spikes shows

the typical neuronal action potential shape. The SNR of the retina tissue recordings is quite low, only 2. As the signals have a reasonable peak to peak amplitude of around $60 \mu V$ the problem is the high background noise (around $30 \mu V$) which may come from a bad cell-tissue coupling.

Again, light stimulation responses are recorded as it can be seen in Figure 84 . Like before, short light flashes of 500 ms are provided by an LED every 15 s .

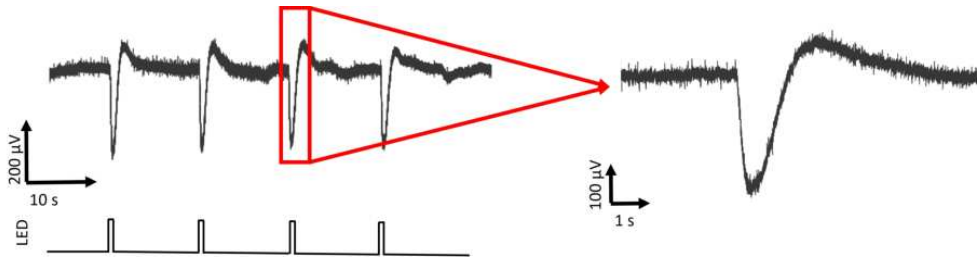


Fig. 84: Recording of light stimulated cells inside an extracted rat retina tissue with stiff probes.

As for the retina recordings with flexible probes the light artefacts can be clearly seen. Each light artefact corresponds to one light stimulus. Spike activity is recorded before during and after the light response. Nevertheless, a significant change in spike amplitude or frequency cannot be observed. Figure 85 illustrates two recorded spikes during the light response of the tissue. The shape of the spikes shows the typical AP shape. Nevertheless, due to the low SNR of only 2 it is hard to say whether cells are being stimulated by the light. At least no clear response of the cells can be observed.

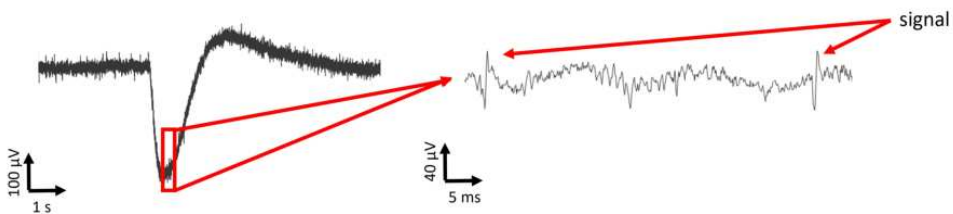


Fig. 85: Recording of AP shape signals during the light stimulation of the rat retina tissue.

As the SNR is very low it is unclear whether the electrodes properly penetrate into the tissue. With the used tissue preparation and placement it is furthermore not possible to actively change the z position of the cylinders inside the tissue in a controlled manner. For future experiments the penetration of the 3D electrodes into the tissue has to be

optimized with adjusting the preparation and placement of the tissue onto the sample. The mechanical force has to be balanced to ensure sufficient penetration but at the same time not destroying the cylinders and the tissue. After optimization of the experimental set up human brain slice experiments with stiff 3D probes can be conducted as well. Furthermore, as for the flexible implants, the electrode pitch, cylinder dimensions as well as electrode heights have to be optimized to get stable recordings of the tissue in multiple depths.

5.4 Stability of PEDOT:PSS

One general challenge occurred during the ex-vivo measurements. If the PEDOT:PSS caps of the 3D electrodes are too big they break during the insertion into the tissue due to the mechanical forces. The big caps are not stable enough and break at the mechanical weakest point. This point is the connection of the small gold string and the cap which reaches out of the cylinder. While the string is protected by the cylinder the cap experiences the mechanical forces during insertion. Figure 86 compares the impedance of PEDOT:PSS electrodes before and after insertion into the tissue.

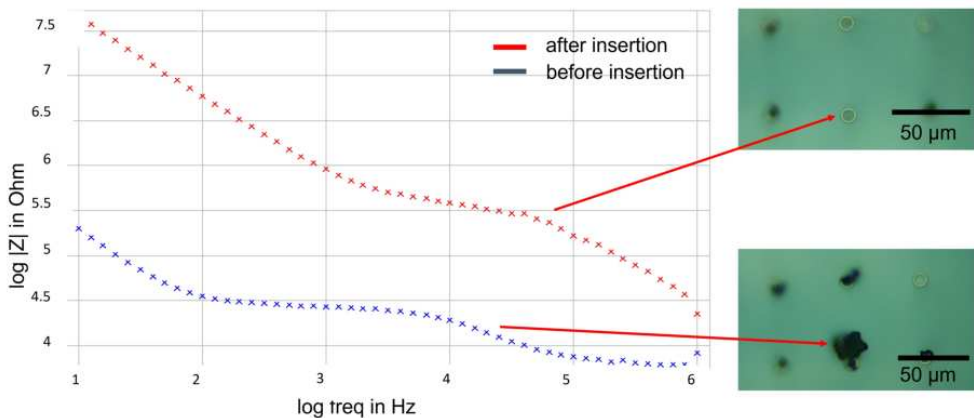


Fig. 86: Left: EIS measurements of 3D electrodes before and after tissue insertion; right: Light microscopy image of the PEDOT:PSS caps on top of the cylinders before and after insertion.

As it can be seen, the impedance increase after the insertion experiments which is an indicator of broken PEDOT:PSS caps. The corresponding light microscopy image shows the comparison of the cap before and after tissue insertion. Before insertion the PEDOT:PSS cap had a diameter of around 20 μm which fits well to the low impedance

of around $50\text{ k}\Omega$ at 1 kHz . During the insertion the mechanical forces broke the PEDOT:PSS cap. The impedance rises to $1\text{ M}\Omega$ which corresponds to the impedance value before PEDOT:PSS deposition. In principle, with a redeposition step a PEDOT:PSS cap can be regrown which will lead to an improve in electrical properties again. Nevertheless, this can lead to inhomogeneous growth. Figure 87 shows a top and side view of a multi-site electrode design after tissue insertion.

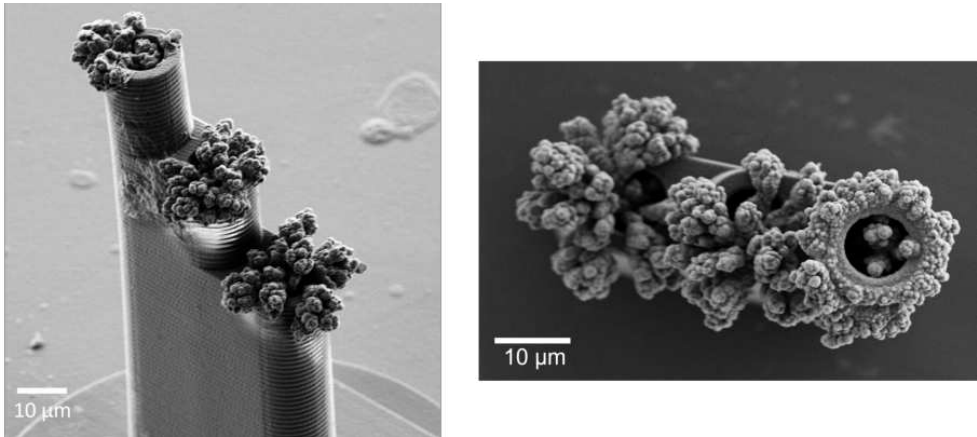


Fig. 87: Scanning electron microscopy image of the multi-site layout after tissue insertion. Left: Before redeposition of PEDOT:PSS; right: After redeposition of PEDOT:PSS.

Only the top electrode has been inserted into the tissue. While the PEDOT:PSS cap of the two lower electrodes are not destroyed the cap of the high electrode is broken. Therefore, a redeposition of PEDOT:PSS has been conducted. Nevertheless, it looks like the PEDOT:PSS mainly grows to the side of the cylinder which leads to shortcuts with the neighboring electrodes. During insertion the cap is too unstable and broke inhomogeneously and thus some PEDOT:PSS remains at the side walls of the cylinder. Therefore, when applying the redeposition step, instead of growing homogeneously and forming a cap, the growth will continue only at the remaining PEDOT:PSS towards the side of the cylinder. As it is not possible to obtain a controlled cap geometry a redeposition step should be avoided. In contrast to the large PEDOT:PSS caps, the 3D printed cylinders are stable also after several (more than 10) tissue insertions. To optimize the deposition process, next to the impedance also the mechanical stability of the PEDOT:PSS and the gold cap against tissue insertion needs to be taken into account for future experiments. Optimal deposition parameters to achieve specific

cap sizes and geometries which lead to suitable impedance values and mechanical stabilities have to be found. Furthermore, more experiments have to be conducted to investigate the long-term stability of the PEDOT:PSS caps and the 3D printed structure for experiments in freely behaving animals.

6 Investigating 3D Neuronal Networks

The first chapter of this work dealt with 3D scaffold systems to achieve controlled 3D neuronal networks. These networks were investigated using microscopy methods. In the second part a new fabrication approach for 3D electrodes has been introduced. With these electrodes it is possible to measure electrical signals from biological 3D tissue from retina and brain ex-vivo. The aim of the last chapter is to combine both methods to be able to electrically investigate a controlled 3D in-vitro neuronal network.

6.1 Scaffold System

As both structures, the cages and the hollow cylinders for the 3D electrodes, are being printed with the two photon polymerization 3D printer it is straight forward to combine both structures. For that the hollow cylinders are introduced to the cage structures as it can be seen in Figure 88.

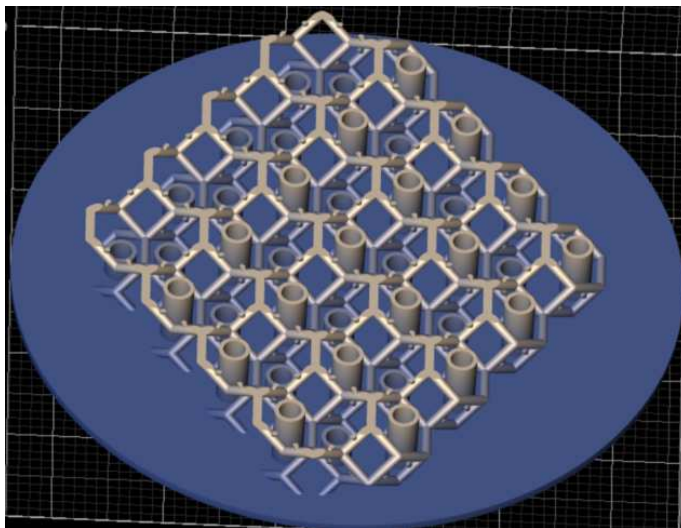


Fig. 88: CAD design of the 3D cage-like scaffolds with integrated 3D cylinders.

The cage barriers between the single cages are removed and the hollow cylinders are added. Their heights match with the height of each cage, so that one hollow cylinder is assigned to one cage. Figure 89 illustrates the approach.

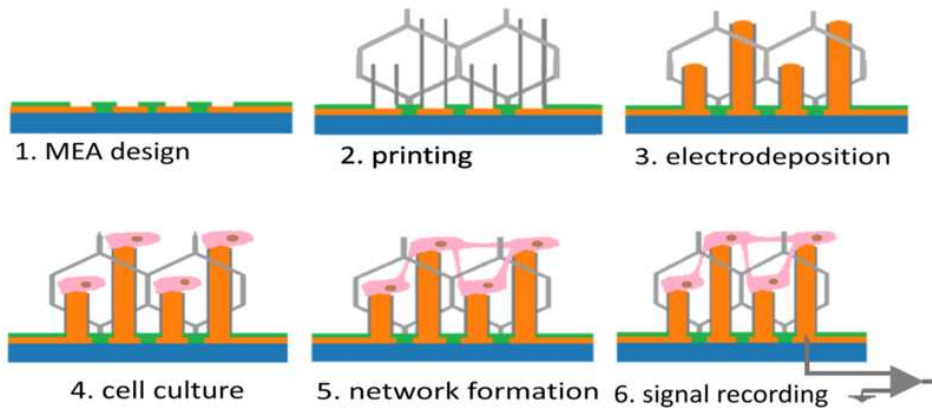


Fig. 89: Schematic approach of integrating 3D electrodes to the scaffold system to record electrical signals of 3D in-vitro neuronal systems.

Compared to Chapter 5 where only steps 1 to 3 were relevant (followed by step 6), steps 4 and 5 have to be added like it has been done also in Chapter 4. After electrodeposition the neurons are cultured into the scaffold and form the network. After 14 DIV spontaneous activities from the in-vitro network can be recorded (89 step 6). To record neural activities it is important that at least some cell bodies and/or dendrites will grow on top of the electrodes as it is illustrated in step 4 of Figure 89. The hollow cylinders with different heights as well as the scaffold which height is adapted to the height of the cylinders are printed together in one print step (89 step 2). The followed gold electrodeposition fills the cylinders with gold and creates 3D electrodes as it has been done in Chapter 5 (89 step 3). Neurons are then seeded onto the 3D structure and grow on the electrodes (89 step 4 and 5). The scaffold around the electrodes shall support the growth of a 3D network which then can be characterized with the electrodes. A stacking process like it has been demonstrated in Figure 4. is not necessary anymore. Thus, the guiding rod which is used for stacking can be removed from the design. In general, the more electrodes are added in each cage either the distance of the cylinders and thus the electrode density has to be decreased (challenging 2D MEA fabrication) or the dimensions of the cages have to be increased. For a first prove of concept the number of electrodes for each cage are kept to 2 and the dimensions of the cages are kept to $50 \mu\text{m}$ (see Chapter 4). This results in a 2D MEA design seen in Figure 90 with 32 electrode openings aligned in a diamond shape matching the cage dimensions.

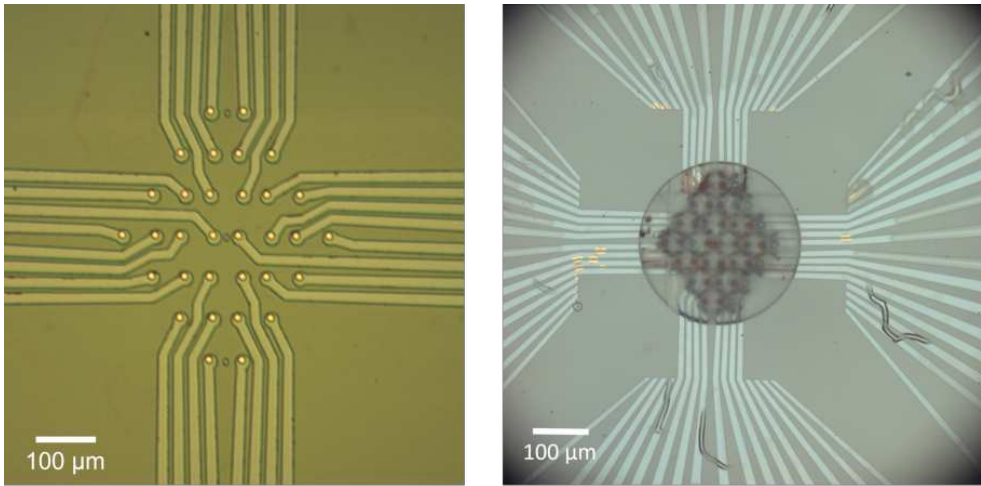


Fig. 90: Light microscopy image of the 2D MEA with 32 electrode openings. Left: Before 3D printing; right: After 3D printing.

The distance of the cylinders is therefore between $20\ \mu\text{m} - 30\ \mu\text{m}$. The height of the cylinders as well as the scaffold is kept to $35\ \mu\text{m}$ for each cage layer but can be easily adapted in the future. Two cage layers are used for the following investigations and thus the heights of the cylinders are $35\ \mu\text{m}$ and $70\ \mu\text{m}$. The outer diameter of the cylinders is $12\ \mu\text{m}$ and the opening is $8\ \mu\text{m}$. These dimensions are already investigated in Chapter 5 and fit quite well to the cylinder dimensions.

The cages and cylinders are being printed with a 63X objective and the polymer IP-L 780 (NanoScribe GmbH, Germany). The optimal printing parameters were found in Chapter 4 and Chapter 5 for the cages and cylinders, respectively. The hatching distance is kept to $200\ \text{nm}$ and the slicing distance is $300\ \text{nm}$. As passivation layer for the 2D MEA, $2\ \mu\text{m}$ SU-8 is used which proved its suitability for having a strong adhesion between the print and the 2D MEA. The right image in Figure 90 shows a stable printed structure on top of the new 2D MEA layout. The thin $3\ \mu\text{m}$ base plate to enhance the adhesion for the gold deposition step is also used this time. Only half of the 64 feedlines reach into the chip center and have openings in the passivation. For a future optimization and improvement of the design it is possible to also introduce the remaining 32 electrodes into the cage structure.

First of all, fluorescent microscopy experiments are done to investigate the influence of the added cylinders in the cage design to the neuronal cell growth and network formation. Furthermore, it has to be verified whether the neurons will grow on top of the

electrodes which is essential for signal recording. Therefore, closed cylinders are added to the cage design to simulate a filled cylinder after gold deposition. Like in Chapter 4 the membrane labeling dye Cell Mask deep red is used to stain the neurons. To improve the contrast the autofluorescent properties of IP-L 780 is used to visualize the scaffold in green. To investigate the influence of the scaffold around the cylinders two samples are prepared and seeded with neurons. For the first sample the scaffold does not reach the higher cylinders but only the lower cylinders. For the second sample the scaffold has been printed all around the lower and higher cylinders. The two samples are treated with oxygen plasma coated with Poly-L-Lysine and seeded with neurons. After 7 DIV the network formation is completed and the dye is applied. With focusing the objective at different height levels inside the printed structure the influence of the scaffold as supporting structure can be clearly seen. In Figure 91 at the left image, the focus is set to the sample surface where the neuronal network has been grown underneath the printed structure not following any pattern. Moving the focus upwards to the lower cylinders the network growth changes and clearly follows the edges of the cage scaffold. A few cell bodies sit on top of the cylinders.

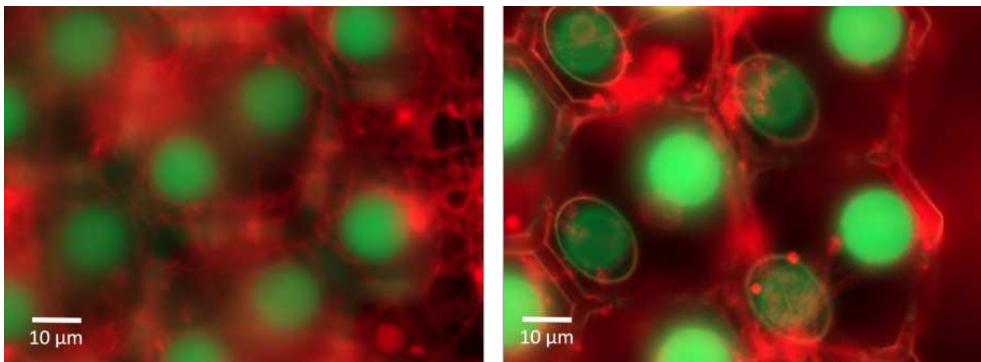


Fig. 91: Fluorescent microscopy image of a 3D in-vitro neuronal network inside a printed cage scaffold system. Left: The focus is set to the substrate surface; right: The focus is set to the height of the lower cylinders.

To get a better idea of how the scaffold system supports the network formation Figure 92 shows the difference of cell network behaviour between samples with different scaffold height.

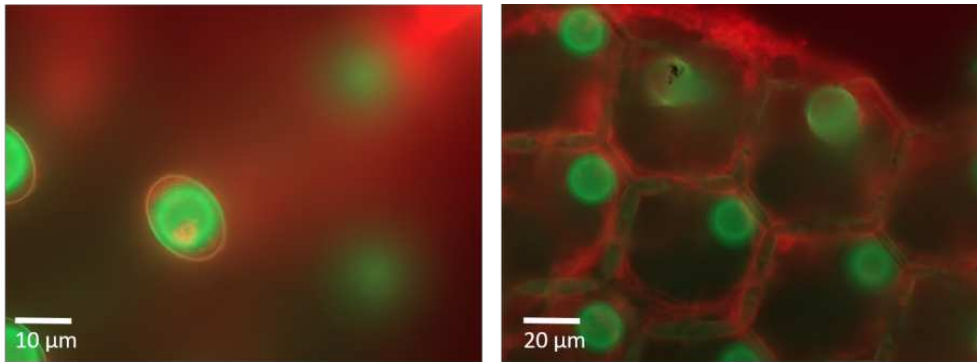


Fig. 92: Fluorescent microscopy image of a 3D in-vitro neuronal network inside a printed cage scaffold system. Left: The scaffold is not printed all the way up to the high cylinders; right: The scaffold is printed all the way up to the high cylinders.

In the left image the scaffold does not reach the high cylinders of $70\ \mu\text{m}$ height. One cell body sits on top of one cylinder. But besides that, no network can be seen. No connection between the neurons are established due to the lack of a scaffold. There is thus no supporting and guiding structure. The neuron on top of the cylinder cannot connect to anything and thus will die. The right image shows the situation at sample 2 where the scaffold does reach up to the higher cylinders. A network clearly has been established also in $70\ \mu\text{m}$ height and follows the cage edges.

As a result it can be said that the scaffold supports the establishing and growth of a 3D network. The axons and dendrites grow along the edges of the cages which leads to a controlled network formation. The formation can be manipulated and controlled with changing the design of the scaffold. Nevertheless, one main challenge remains. Only few neurons grow on top of the cylinders. Due to the higher surface of the side walls and cage edges compared to the top surface of the cylinder most of the cells rather grow on the cylinder sidewalls or at the cage edges. Figure 93 shows a fluorescent investigation with the dye SiR-actin (Spirochrome AG, Switzerland). This dye is based on the fluorophore silicon rhodamine (SiR). It allows the labelling of F-actin in the living cells with high specificity and low background leading to a higher contrast than what is achieved for Cell Mask deep red. In this case the axons and dendrites can be investigated more in detail. Hollow cylinders without any scaffold are printed and seeded with neurons.

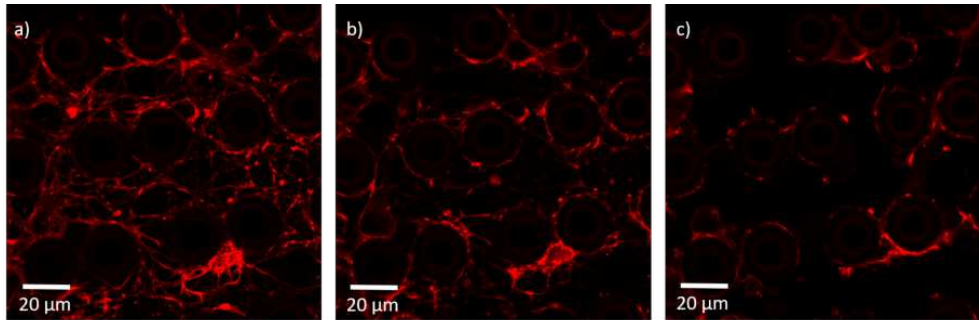


Fig. 93: Fluorescent microscopy image of a neuronal network around printed cylinders labeled with SiR-actin. The focus is set to the substrate surface (a) and $6\ \mu\text{m}$ (b) as well as $10\ \mu\text{m}$ (c) away from the substrate.

From left to right the focus is changed from the substrate surface (a) to $6\ \mu\text{m}$ height (b) to $10\ \mu\text{m}$ height (c). At the substrate surface the network is formed. Cell bodies sit in close proximity to the cylinder walls and dendrites grow all around. As expected and already shown in previous experiments with increasing distance from the substrate surface less dendrites can be seen between the cylinders due to the lack of a scaffold structure. Due to the cage design the distance between the cylinders differs. More connections can be seen between cylinders which are closer to each other. The dendrites grow along the sidewalls of the cylinders. Only a few dendrites overcome the short distance between neighbouring cylinders and form connections. At a height of $10\ \mu\text{m}$ already almost no network can be seen. Neurons which sit at the sidewalls of the cylinders above $10\ \mu\text{m}$ or even at the top of the cylinders cannot form connections between the neurons at different cylinders without the support of a scaffold. Fluorescent investigations clearly show the need of a scaffold to support the formation of a proper 3D network. The sidewalls of the cylinders are used by the neurons and the dendrites as additional support structures but they are not enough to form connections between the cylinders. Therefore, it is very important to add the cages in between the cylinders.

To get an even better understanding on the interaction between the printed structure and the neurons SEM investigations are conducted. To prepare the cells for the electron microscope they first have to be fixed on the sample. For that glutaraldehyde is used. The whole sample preparations step can be seen in the materials and method section. A CPD process allows for exchanging the liquid phase to a gas phase without destroying the cells. Figure 94 shows a top view of a scaffold system with cells around and inside the scaffold. Many cell bodies can be seen in close proximity to the scaffold system.

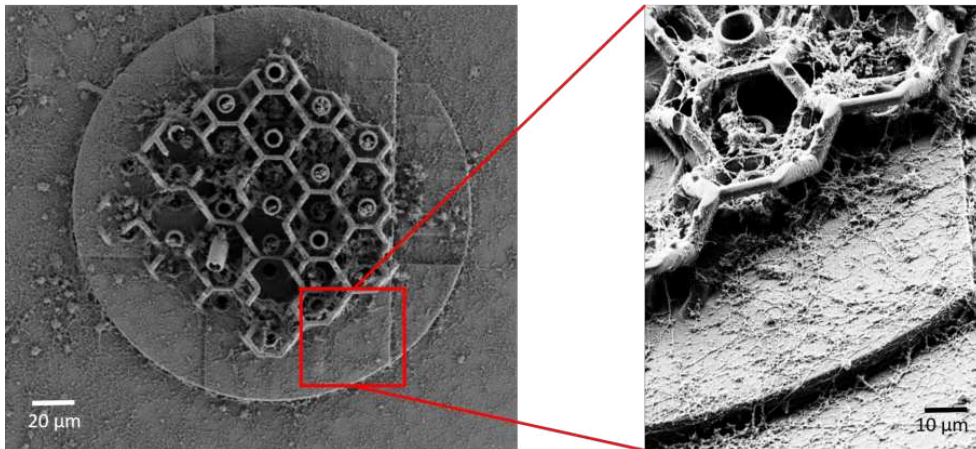


Fig. 94: Scanning electron microscopy top view image of fixed neurons inside a printed 3D scaffold with integrated filled cylinders.

A zoomed in image shows the biocompatibility of the scaffold system. As it already has been demonstrated in Chapter 4 the scaffold material IP-L 780 is biocompatible and does not show any toxic effect after 14 DIV. The neurons have established their network. Small dendrites connect to the cell bodies. The image shows two transitions. At the first interface between the glass substrate and the 3 μm thick base plate no negative effect of the base plate can be observed. The dendrites easily overcome the height difference and grow back and forth between the base plate and the glass substrate. The same situation can be observed when the dendrites are close to the scaffold structure. Several connections between neurons sitting on the the base plate and inside the scaffold have been established. Next to the biocompatibility also the suitability of the scaffold to support the 3D growth can be further investigated. For that, a zoomed in top view can be seen in Figure 95.

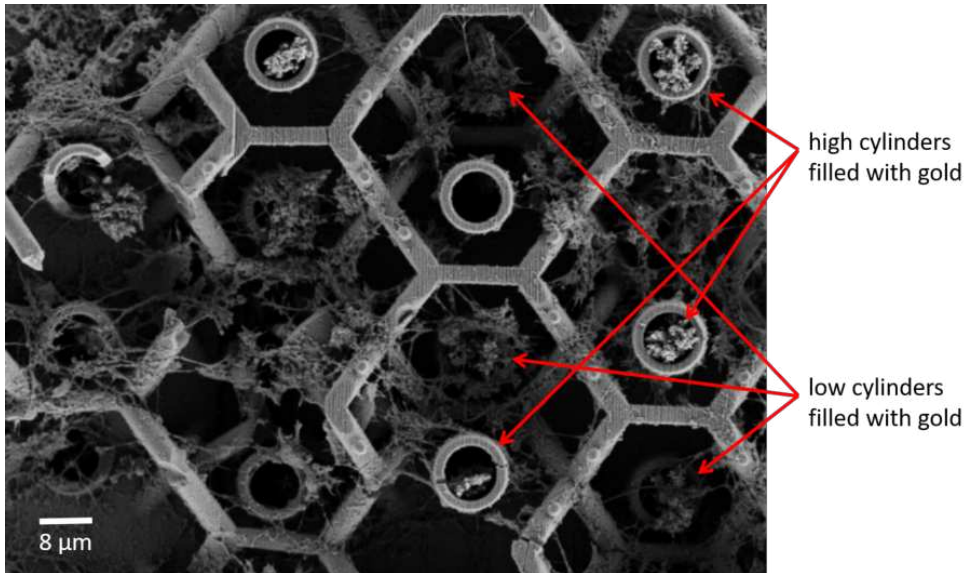


Fig. 95: Scanning electron microscopy top view image of fixed neurons inside a printed 3D scaffold with integrated filled cylinders.

Two main conclusion can be drawn. First of all, the SEM image confirms the results of the fluorescence investigation that the neurons use the scaffold to establish their network. While some dendrites also can overcome short distances without supporting structure, e.g. between the cylinders and the surrounded scaffold, they mainly grow along the cage edges and nicely form a 3D network throughout the whole height of the scaffold. Secondly, a difference between the interaction of cells with low cylinders and high cylinders can be observed. While the low cylinders strongly interact with the cells almost no neurons or dendrites grow at the higher cylinders. To get a better idea of the situation, Figure 96 illustrates a tilted view with a low cylinder in the back and a high cylinder in the front. Both cylinder are filled with gold.

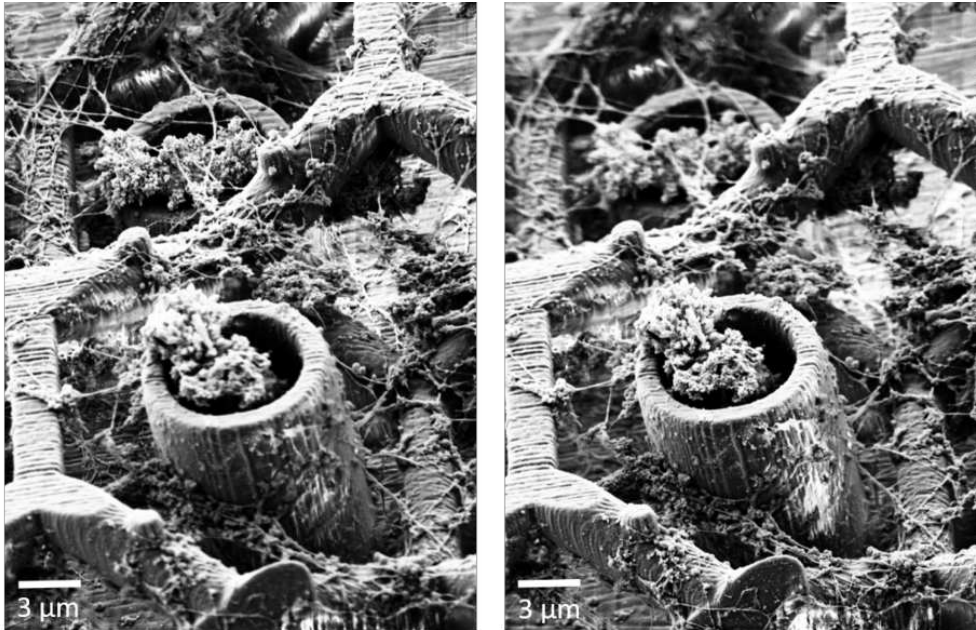


Fig. 96: Scanning electron microscopy side view image of the interaction between the neurons and two cylinders with different heights within the 3D scaffold.

Although no cell body sits on the back electrode dendrites grow on top and strongly interact with the gold. In contrast, there is no interaction between the gold of the high front electrode and the neurons. Dendrites clearly use the side wall of the cylinder as supporting structure and also grow along the sidewall but do not reach the gold at the top. It seems, that the dendrites only grow up to a certain height (slightly below the cylinder tip) and then continue to grow along the cage edges. This confirms the findings of the fluorescent investigations. Apparently the neurons have too less supporting structure surrounding the tip of the high cylinders. There is supporting structure all around the low cylinders which seems to be preferable for a proper 3D network growth. To improve the interaction with the gold of the high cylinders and therefore being able to record signals with them it is necessary to add supporting structure even further above the high cylinders so that dendrites will reach the gold at the top. Additionally, the SEM investigations confirm the challenge of neuronal bodies only growing at the sidewalls or at the cage edges. The free standing cylinders do not have structures in close proximity where the cell bodies can sit after cell seeding. Therefore, adjusting the geometry, e.g. adding a thin plate to increase the material surface around the electrodes, of the

structure can lead to an improvement, as this way the probability of having cell bodies close to the electrodes increases. A similar approach is to increase the wall thickness of the cylinders or to add some bridges between the cylinders and the cage edges to improve the guiding of dendrites and axons from cage edges to the cylinders.

6.2 Electrochemical Deposition of Gold

To deposit gold the cylinders are printed around the electrodes of the 2D diamond shape MEA which design has been explained further above. The gold deposition is done the same way as in Chapter 5 introduced. As in-vitro action potentials of primary cortical neurons are usually higher than for tissues an additional PEDOT:PSS step is not performed for this application. Therefore, during the second deposition step a constant current of -200 nA is applied for 1 min to create gold caps with around $20 \text{ }\mu\text{m}$ as investigated in Chapter 5 and as it can be seen in Figure 97. It shows the cage structure with filled cylinders and the corresponding impedance values. The cap sizes slightly differ from electrode to electrode. The reason has been investigated and explained in Chapter 5.

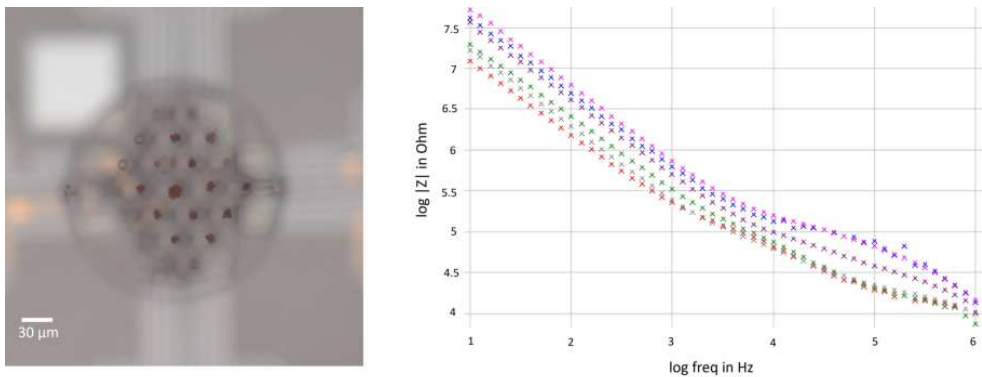


Fig. 97: Characterization of 3D electrodes within a scaffold system. Left: Light microscopy image of gold filled cylinders; right: EIS curves of the corresponding 3D electrodes.

The variation in cap size can be also seen in the impedance plots. The bigger the gold cap the lower the impedance. Nevertheless, even the smallest caps show impedance values below 1 MOhm at 1 kHz which is suitable to measure in-vitro signals.

6.3 Primary Cortical Embryonic Rat Neurons

The fabricated 3D device with 32 electrodes (diamond shape) and a SU-8 passivation are used to conduct in-vitro experiments. For that, primary cortical embryonic rat neurons are cultivated on top of the structure which is coated with Poly-L-Lysine beforehand to improve the interaction with the neurons. To increase the probability of having neuronal cell bodies on top of some electrodes the seeded cell density is chosen to be very high ($4000 \frac{\text{cells}}{\text{mm}}$). After cultivating the neurons for 14 days they form networks and start to release spontaneous activities which are measured by the 3D electrodes. Figure 98 illustrates cultivated neurons on the device after fixation of the cells. The typical neuronal network cannot be seen, as the density is too high.

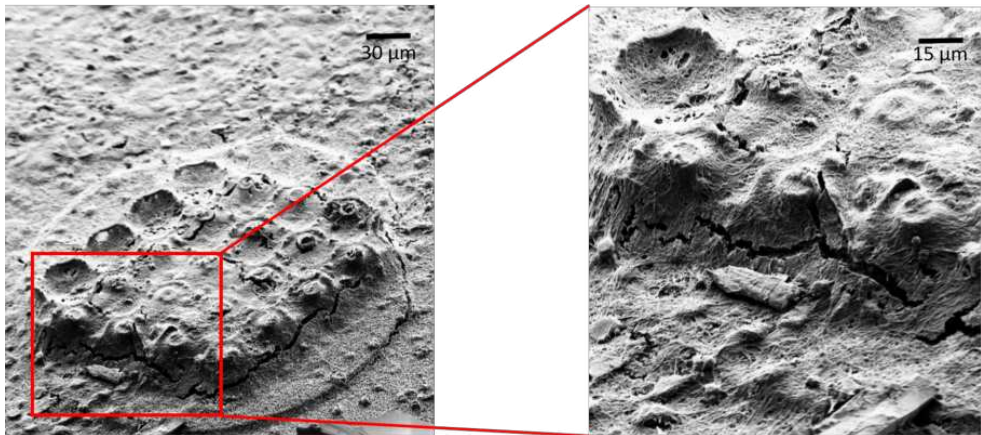


Fig. 98: Scanning electron microscopy image of a high density culture of cortical, embryonic rat neurons on top of a 3D scaffold system.

As expected, the neurons grow in a tissue like manner. The cages and cylinders are completely covered and only can be distinguished by their geometries. No difference can be seen between the coverage of the substrate and the scaffold after 14 DIV. The high cylinders are completely covered by the network which proves the suitability of the high density to record signals also from the high electrodes. During the preparation process mechanical stress is induced into the network due to shrinkage of the cell structures. This stress leads to cracks in the tissue like network at the weakest points. The right image of Figure 98 shows a zoomed in side view of the transition between the base plate and the scaffold. The network grew nicely from the base plate onto the scaffold using the cages as supporting structure. Exactly at the middle between base plate and scaffold big cracks can be seen.

SEM investigations show the suitability in using high density cultures to have cells also on top of the high electrodes. However, this approach can only be used as a prove of concept whether the 3D electrodes are able to measure signals. The advantage of having the cage scaffold around the electrodes to get a controlled network growth is of course not given due to the high density. Therefore, future experiments have to be conducted with cell densities used in Chapter 4 to get only few cells in each cage and thus being able to characterize the controlled network. Optimizations on how to increase the probability to get cells close to the high electrodes have been already discussed further above.

Figure 99 illustrates recorded spontaneous activities within the 3D network.

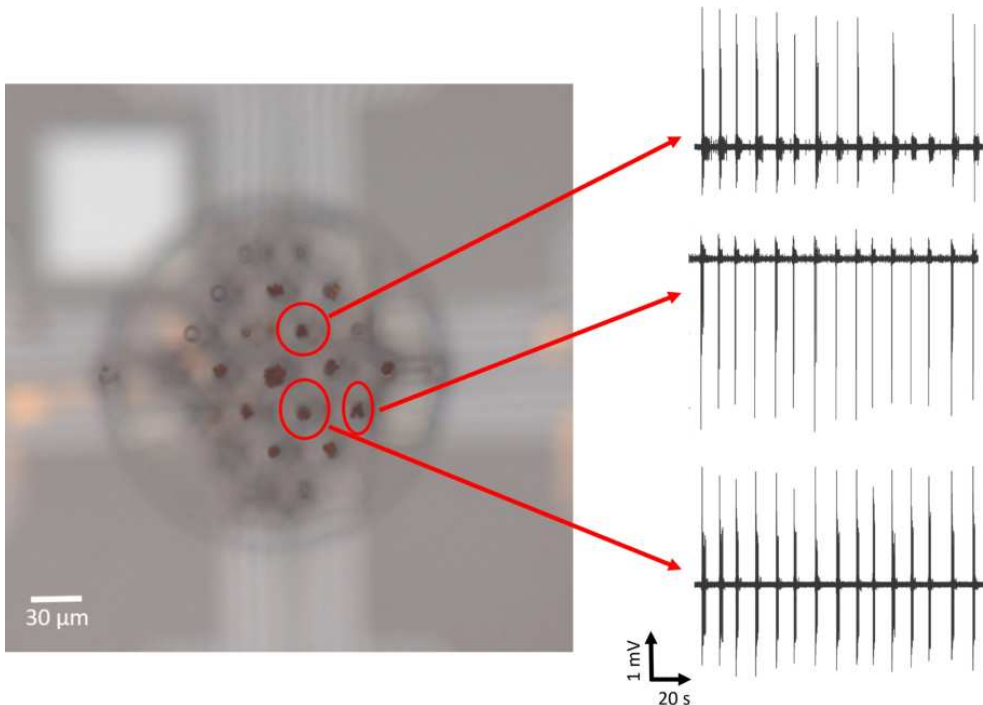


Fig. 99: Recording of spontaneous activities of an in-vitro 3D neuronal network. The light microscope image illustrates the location of each recording within the network.

All three electrodes have a height of $70 \mu m$ and are spatially close together. The recorded amplitudes of APs reach a peak to peak voltage of up to $3.7 mV$ and SNRs of up to 179. The reason for these high signals probably lays in the improved coupling between the rough 3D structures and the neurons which can engulf these 3D gold

caps leading to a tighter sealing. This strong coupling behaviour agrees with findings in the literature for 2D+ electrode shapes like high aspect ratio nano straws [22] and gold mushrooms [51]. The recorded APs appear at the same frequencies for all three electrodes. Due to the high density of neurons it is unlikely to measure single cell activity but rather an overlay of the action potentials of multiple active neurons close to each electrode. Nevertheless, due to the equal frequency of recorded signals for all three electrodes a synchronized network in the measured area is assumed. As it can be seen in Figure 100 all three electrodes record different amplitudes and shapes of the signals ranging from clearly bi-phasic to rather mono-phasic.

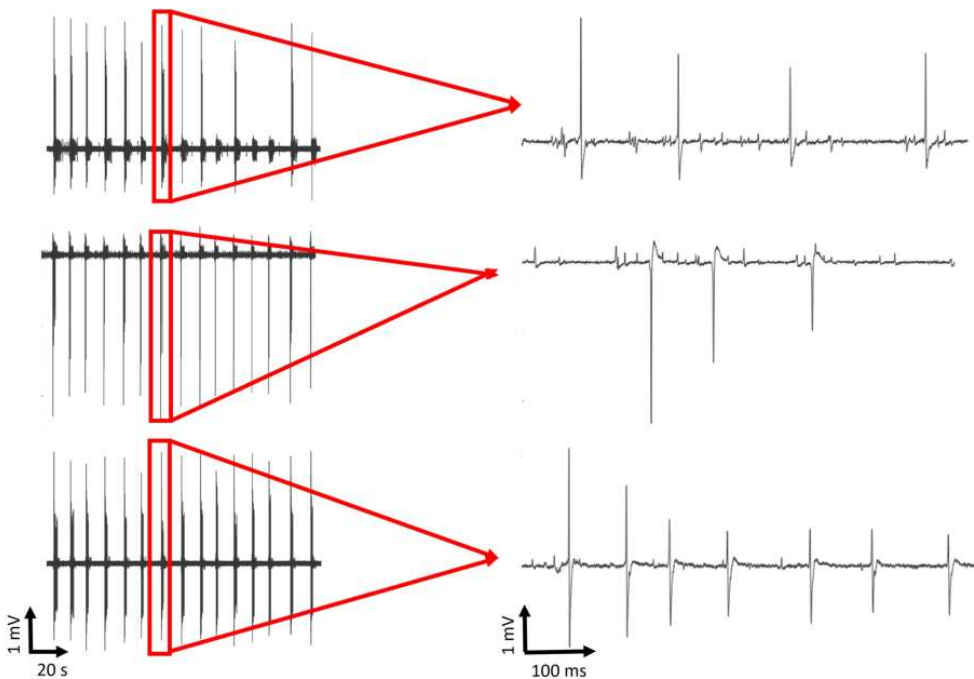


Fig. 100: Recording of spontaneous activities of an in-vitro 3D neuronal network. The recorded signals of all three electrodes differ in amplitude and shape.

Amplitudes and shapes are mainly determined by the electrical properties of the electrodes, the distance between electrode and neuron as well as their coupling behaviour. Inbetween the high amplitude signals also smaller spikes are recorded which come from neurons sitting further away from the recording electrodes. Furthermore, the high signals have a slight time from electrode to electrode of about 10 *ms* to 20 *ms*. This time shift is expected and illustrates the synchronized activity travelling through the network.

In contrast to the fully synchronized network behaviour seen above, Figure 101 illustrates different spiking behaviours of the network.

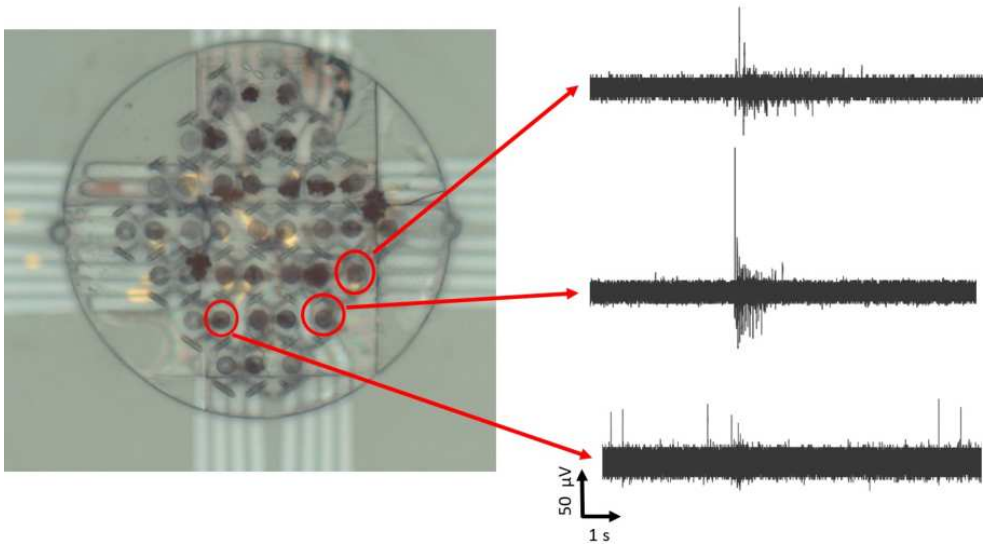


Fig. 101: Recording of spontaneous activities of an in-vitro 3D neuronal network. The light microscope image illustrates the location of each recording within the network.

The two electrodes close to each other have a height of $70 \mu m$. The left electrode has a height of $35 \mu m$ and is further away. The recorded signals show different behaviors. The neurons recorded by the high electrodes show bursting activities with many spikes in a very short time period followed by some time period without any spiking activity. The two electrodes are located close to each other with the same height and thus record the same neurons. The bursts happen at the same time. In contrast the spontaneous activity recorded by the lower electrode appears at completely different time periods and in a more regular basis. Thus, the left electrode measures different neurons which are apparently not directly connected to the ones measured by the two high electrodes. Compared to the ex-vivo experiments with the active insertion of the devices into the tissue, the in-vitro approach with seeding the neurons on top of the structure is less destructive. Therefore, the cage scaffold as well as the gold caps are stable enough to survive the experiment. After a proper cleaning step to ensure a complete removing of the remaining tissue on top of the 3D structure the chips can be reused. Figure 102 shows a sample with the 3D structures after five electrophysiological experiments. The

cage structure as well as the gold caps are stable enough. Also, the impedance values remain the same after proper cleaning.

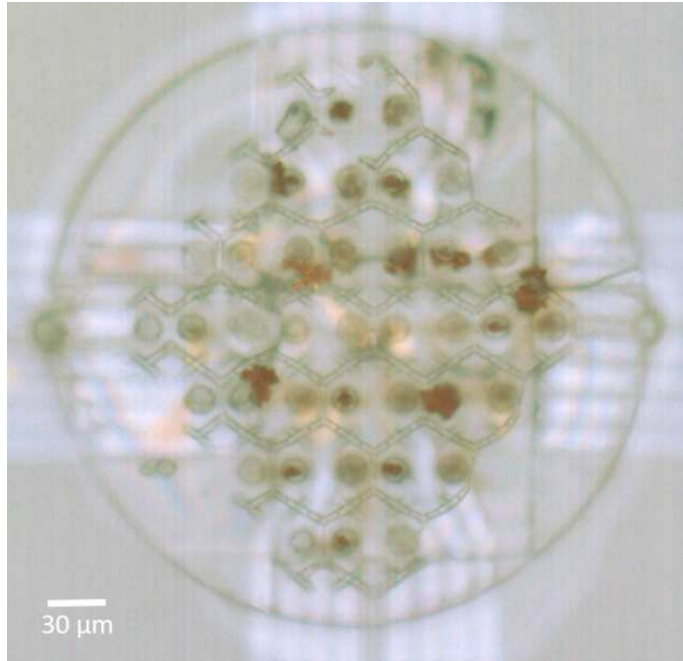


Fig. 102: Light microscopy image of a printed scaffold with integrated filled cylinders after five electrophysiological measurements.

In-vitro spontaneous activities of primary cortical rat neurons could be successfully measured by the fabricated 3D electrodes of $35\ \mu\text{m}$ and $70\ \mu\text{m}$ heights. The cell density was chosen to be very high to increase the probability to get neurons close to the electrodes. The recorded signals have a peak to peak amplitude up to $3.7\ \text{mV}$ and very high SNRs up to 95 which assumingly come from the tight sealing of the 3D electrode and the neurons. Further experiments have to be conducted to characterize this improved coupling. The results can be used to optimize the shape and of the gold cap to even further improve the coupling. To use the advantage of having three dimensional electrodes integrated into a 3D scaffold and thus being able to analyze a controlled 3D neuronal network, for future experiments the cell density needs to be decreased. Investigations in Chapter 4 give a first hint of suitable cell densities to only get one neuron in one cage. In this regard scaffold geometry as well as biological coating optimizations will lead to a controllable 3D network which then can be electrically analyzed to get information like network formation as well as signal propagation in all

three dimensions.

7 Summary and Outlook

In this work a new platform for the investigation of three-dimensional neuronal networks and tissues in-vitro and in-vivo has been introduced. The focus of brain research recently shifts to more complex 3D systems which better reflects the reality than 2D systems. Therefore, new methods to investigate such 3D systems, as for instant organoids and tissues (brain, retina) in all three dimensions are highly desired. In general, 3D networks need scaffold systems as growth support. Soft hydrogel environments are widely used but have the disadvantage of not being able to control and manipulate the network growth. Thus, to have a precise control over the network formation hard scaffolds with feature sizes of less than 1 μm are needed.

Therefore, in the first part of this work high resolution, solid scaffold systems are developed and fabricated with the help of a TPP 3D printer. The biocompatible polymer IP-L 780 (NanoScribe GmbH, Germany) was used as scaffold material. Based on the work of Larramendy et al. [7] cage-like structures are designed and stacked onto each other to precisely confine the location of in-vitro neuronal cell bodies while at the same time allowing for high freedom of 3D network formation. With implementing guiding rods to the design the stacking procedure could be drastically improved which resulted in stable 3D scaffolds with heights up to several 100 μm . Fluorescent as well as SEM investigations demonstrated the suitability of the 3D scaffold system. Cell connections were established by dendrites and axons which grew along the cage edges and thus used the scaffold as growth support. It was possible to achieve healthy and highly controlled neuronal networks in all three dimensions, at least up to 21 DIV.

An optimization of the scaffold geometry as well as scaffold material will further improve the interaction between cells and scaffold in the future. A hybrid composite material system with a stiff, high resolution scaffold and a softer matrix will combine the advantages of high cell viability while at the same time achieving a suitable network manipulation.

To get a better understanding of the investigated 3D neuronal network systems electrical characterizations were conducted in part 2 of this work to supplement the microscopy investigations of part 1. Widely used 2D MEAs have the huge disadvantage of lacking the third dimension, and thus only can monitor surface activities of 3D networks and tissues. Therefore, introducing real three dimensional electrodes which reach different network depths is essential. To address this challenge, the second part of the work introduced a

fully customizable 3D microelectrode platform for signal recording of complex neuronal networks. Hollow cylinders with different geometries were designed and 3D printed with a TPP printer. Those cylinders were used as high aspect ratio templates to direct the electrochemical deposition of gold and PEDOT:PSS fabricating electrodes with heights up to 150 μm . Furthermore, the used polymer IP-L 780 (NanoScribe, Germany) acted as an electrode passivation. The advantage of this fabrication method is the high degree of design freedom of the 3D electrodes which have diameters of less than 10 μm and can adapt to the diverse requirements of different 3D neuronal tissue systems. The templates were printed around the electrode openings of standard 2D MEA devices, and therefore, besides the 3D printing step, no further complex microfabrication steps are needed. To demonstrate the flexibility of the developed 3D electrode platform, several stiff as well as flexible 2D probe designs were used to fabricate different 3D electrode neuronal implants. First of all, the electrochemical deposition process was optimized to fill the template with gold. As SEM investigations illustrated, only a thin gold string with a diameter between 2 μm and 3 μm rather than a complete template filling was achieved. Due to the high aspect ratios of the templates as well as the confined gold bath volume inside the cylinder the deposition process is strongly diffusion limited. To improve the electrical properties of the 3D electrodes PEDOT:PSS was electrodeposited onto the gold to reduce the impedance of at least one order of magnitude. Finally, the stiff and flexible probes were used to successfully record spontaneous as well as light-stimulated cell activities from rat retina as well as human brain slice tissues in different depths. The flexible implants were implanted in a top-down approach where they were actively driven into the tissue from the top with the help of micromanipulators. On the other hand, a bottom-up approach was used for stiff probes. Here, the tissue was placed onto the 3D MEA from the top.

The developed approach allows for fabricating fully customizable 3D microelectrodes to study complex 3D neuronal systems. As the 3D printed cylinders act as templates for the electrodeposition and at the same time passivate the electrodes this approach reduces manufacturing time tremendously compared to other state-of-the-art 3D electrode approaches [39][40]. Furthermore, the developed platform is used to fabricate 3D electrodes with arbitrary heights, less than 10 μm diameter and high aspect ratios (50:1) onto stiff as well as flexible 2D MEA layouts with different designs, demonstrating its outstanding flexibility. Finally, using a combination of the TPP process and polymers with

low Young's modulus, such as PaC and SU-8, allows the fabrication and application of high-density 3D MEAs with significant lower implantation footprint and foreign body reactions compared to other state-of-the-art 3D neuronal probes such as stiff "Utah" arrays. Further experiments have to be conducted in the future to investigate and quantify the long-term stability and foreign body reaction. Furthermore, in-vivo recordings as well as stimulation experiments with the fabricated 3D MEAs should be conducted in the future. For that, a deeper insight on the mechanical properties as well as penetration behaviour of the electrodes is needed. To improve penetration properties insertion aids may be necessary. A possible way has already been shown at the end of Chapter 5 where a tiny tip of less than 1 μm diameter is added to the cylinder design. Furthermore, to be able to address the needs of different applications it will be necessary to increase the heights of the 3D electrodes towards the mm range. For that, a further optimization of the electrochemical process is necessary. Additionally, direct TPP printing of conductive structures might reduce the spatial resolution of the electrodes in the future. As the developed 3D electrode approach can be used with any kind of 2D base MEA probe a combination with high density CMOS based probes in the future will improve the performance of 3D implants. The customizability of the developed platform opens the path for advanced and personalized brain computer interfaces which can be adapted to the specific needs of an application or patient taking a big step towards the clinical translation of such devices.

In the last chapter of the work, the approaches of the first and second part were combined to electrically characterize highly controlled 3D neuronal in-vitro networks. This will result in a better understanding of network formation as well as signal propagation in all three dimensions. The hollow cylinder from part 2 were integrated into the cage scaffold system of part 1 and 3D printed in one printing step. The cylinder templates were filled with gold. Fluorescent as well as SEM investigations showed a successful integration of the cylinders into the surrounding scaffold. To achieve necessary interactions between the gold electrodes at different heights and the in-vitro neuronal network, the presence of the 3D scaffold around the electrodes is crucial. Primary, embryonic, cortical rat neurons were cultivated onto the 3D system and electrophysiological recordings were conducted after 14 DIV. Spontaneous cell activities with exceptionally peak to peak amplitudes of up to 3.7 mV and high SNRs up to 179 were measured with electrodes of different heights.

In the future, a combined platform of 3D scaffolds and electrodes will allow the growth support and precise control of e.g. different organoid or organ on a chip platforms while at the same time allow for deep electrical characterization at any life cycle stage. This results in a better understanding of 3D neuronal in-vitro systems which will lead to better platforms for human disease research as well as to replace in-vivo models for disease treatments.

8 References

1. AZEVEDO, F. A. et al. Equal numbers of neuronal and nonneuronal cells make the human brain an isometrically scaled-up primate brain. *The Journal of Comparative Neurology* [online]. 04/10/2009, **513**(5), pp. 532–541 [visited on 04/24/2023]. Available from DOI: 10.1002/cne.21974.
2. ESCOSURA-MUNIZ, A. de la et al. Alzheimer's disease biomarkers detection in human samples by efficient capturing through porous magnetic microspheres and labelling with electrocatalytic gold nanoparticles. *Biosensors and Bioelectronics* [online]. 05/2015, **67**, pp. 162–169 [visited on 04/24/2023]. Available from DOI: 10.1016/j.bios.2014.07.086.
3. HEMM, S.; WOERDELL, K. Stereotactic implantation of deep brain stimulation electrodes: a review of technical systems, methods and emerging tools. *Medical & Biological Engineering & Computing* [online]. 07/2010, **48**(7), pp. 611–624 [visited on 04/24/2023]. Available from DOI: 10.1007/s11517-010-0633-y.
4. NORMANN, R. et al. Cortical implants for the blind. *IEEE Spectrum* [online]. 05/1996, **33**(5), pp. 54–59 [visited on 04/24/2023]. Available from DOI: 10.1109/6.490057.
5. CARTER, S.-S. D. et al. Three-dimensional neuronal cell culture: in pursuit of novel treatments for neurodegenerative disease. *MRS Communications* [online]. 09/2017, **7**(3), pp. 320–331 [visited on 04/24/2023]. Available from DOI: 10.1557/mrc.2017.96.
6. DERMUTZ, H. et al. Paper-based patterned 3D neural cultures as a tool to study network activity on multielectrode arrays. *RSC Advances* [online]. 2017, **7**(62), pp. 39359–39371 [visited on 04/24/2023]. Available from DOI: 10.1039/C7RA00971B.
7. LARRAMENDY, F. et al. 3D arrays of microcages by two-photon lithography for spatial organization of living cells. *Lab on a Chip* [online]. 2019, **19**(5), pp. 875–884 [visited on 04/17/2023]. Available from DOI: 10.1039/C8LC01240G.
8. HIPPLER, M. et al. 3D Scaffolds to Study Basic Cell Biology. *Advanced Materials* [online]. 06/2019, **31**(26), p. 1808110 [visited on 04/24/2023]. Available from DOI: 10.1002/adma.201808110.

9. LIAO, C.; WUETHRICH, A.; TRAU, M. A material odyssey for 3D nano/microstructures: two photon polymerization based nanolithography in bioapplications. *Applied Materials Today* [online]. 06/2020, **19**, p. 100635 [visited on 04/24/2023]. Available from DOI: 10.1016/j.apmt.2020.100635.
10. HAUPTMANN, N. et al. Biomimetic Designer Scaffolds Made of D,L -Lactide- ϵ -Caprolactone Polymers by 2-Photon Polymerization. *Tissue Engineering Part B: Reviews* [online]. 06/2019, **25**(3), pp. 167–186 [visited on 04/24/2023]. Available from DOI: 10.1089/ten.teb.2018.0284.
11. HOHMANN, J. K.; FREYMANN, G. von. Influence of Direct Laser Written 3D Topographies on Proliferation and Differentiation of Osteoblast-Like Cells: Towards Improved Implant Surfaces. *Advanced Functional Materials* [online]. 11/2014, **24**(42), pp. 6573–6580 [visited on 04/24/2023]. Available from DOI: 10.1002/adfm.201401390.
12. QIAN, X.; SONG, H.; MING, G.-I. Brain organoids: advances, applications and challenges. *Development* [online]. 04/15/2019, **146**(8), dev166074 [visited on 04/24/2023]. Available from DOI: 10.1242/dev.166074.
13. FLIGOR, C. M. et al. Three-Dimensional Retinal Organoids Facilitate the Investigation of Retinal Ganglion Cell Development, Organization and Neurite Outgrowth from Human Pluripotent Stem Cells. *Scientific Reports* [online]. 09/28/2018, **8**(1), p. 14520 [visited on 04/24/2023]. Available from DOI: 10.1038/s41598-018-32871-8.
14. GREINER, A. M.; RICHTER, B.; BASTMEYER, M. Micro-Engineered 3D Scaffolds for Cell Culture Studies: Micro-Engineered 3D Scaffolds. *Macromolecular Bioscience* [online]. 10/2012, **12**(10), pp. 1301–1314 [visited on 04/24/2023]. Available from DOI: 10.1002/mabi.201200132.
15. HARBERTS, J. et al. Toward Brain-on-a-Chip: Human Induced Pluripotent Stem Cell-Derived Guided Neuronal Networks in Tailor-Made 3D Nanoprinted Microscaffolds. *ACS Nano* [online]. 10/27/2020, **14**(10), pp. 13091–13102 [visited on 04/24/2023]. Available from DOI: 10.1021/acsnano.0c04640.
16. OVSIANIKOV, A et al. Laser printing of cells into 3D scaffolds. *Biofabrication* [online]. 03/01/2010, **2**(1), p. 014104 [visited on 04/24/2023]. Available from DOI: 10.1088/1758-5082/2/1/014104.

17. PURTOV, J. et al. Improved development procedure to enhance the stability of microstructures created by two-photon polymerization. *Microelectronic Engineering* [online]. 07/2018, **194**, pp. 45–50 [visited on 04/17/2023]. Available from DOI: 10.1016/j.mee.2018.03.009.
18. SONG, J. et al. From Simple to Architecturally Complex Hydrogel Scaffolds for Cell and Tissue Engineering Applications: Opportunities Presented by Two-Photon Polymerization. *Advanced Healthcare Materials* [online]. 01/2020, **9**(1), p. 1901217 [visited on 04/24/2023]. Available from DOI: 10.1002/adhm.201901217.
19. LEE, K.-S. et al. Advances in 3D nano/microfabrication using two-photon initiated polymerization. *Progress in Polymer Science* [online]. 06/2008, **33**(6), pp. 631–681 [visited on 04/24/2023]. Available from DOI: 10.1016/j.progpolymsci.2008.01.001.
20. RICHTER, B. et al. Guiding Cell Attachment in 3D Microscaffolds Selectively Functionalized with Two Distinct Adhesion Proteins. *Advanced Materials* [online]. 02/2017, **29**(5), p. 1604342 [visited on 04/24/2023]. Available from DOI: 10.1002/adma.201604342.
21. HUANG, Q. et al. Shell microelectrode arrays (MEAs) for brain organoids. *Science Advances* [online]. 08/19/2022, **8**(33), eabq5031 [visited on 04/24/2023]. Available from DOI: 10.1126/sciadv.abq5031.
22. SHOKOOHIMEHR, P. et al. High-Aspect-Ratio Nanoelectrodes Enable Long-Term Recordings of Neuronal Signals with Subthreshold Resolution. *Small* [online]. 06/2022, **18**(22), p. 2200053 [visited on 04/24/2023]. Available from DOI: 10.1002/smll.202200053.
23. LEE, S. H. et al. Scalable Thousand Channel Penetrating Microneedle Arrays on Flex for Multimodal and Large Area Coverage BrainMachine Interfaces. *Advanced Functional Materials* [online]. 06/2022, **32**(25), p. 2112045 [visited on 04/24/2023]. Available from DOI: 10.1002/adfm.202112045.
24. LIU, Y. et al. Soft conductive micropillar electrode arrays for biologically relevant electrophysiological recording. *Proceedings of the National Academy of Sciences* [online]. 11/13/2018, **115**(46), pp. 11718–11723 [visited on 04/24/2023]. Available from DOI: 10.1073/pnas.1810827115.

25. SMIRNOVA, L. et al. Organoid intelligence (OI): the new frontier in biocomputing and intelligence-in-a-dish. *Frontiers in Science* [online]. 02/28/2023, **1**, p. 1017235 [visited on 04/24/2023]. Available from DOI: 10.3389/fsci.2023.1017235.
26. WANG, Y. et al. Implantable intracortical microelectrodes: reviewing the present with a focus on the future. *Microsystems & Nanoengineering* [online]. 01/05/2023, **9**(1), p. 7 [visited on 04/24/2023]. Available from DOI: 10.1038/s41378-022-00451-6.
27. JUN, J. J. et al. Fully integrated silicon probes for high-density recording of neural activity. *Nature* [online]. 11/09/2017, **551**(7679), pp. 232–236 [visited on 04/24/2023]. Available from DOI: 10.1038/nature24636.
28. BARRESE, J. C. et al. Failure mode analysis of silicon-based intracortical microelectrode arrays in non-human primates. *Journal of Neural Engineering* [online]. 12/01/2013, **10**(6), p. 066014 [visited on 04/24/2023]. Available from DOI: 10.1088/1741-2560/10/6/066014.
29. CAMPBELL, P. K. et al. A chronic intracortical electrode array: preliminary results. *Journal of Biomedical Materials Research*. 08/1989, **23**(A2 Suppl), pp. 245–259.
30. WISE, K. D.; ANGELL, J. B.; STARR, A. An Integrated-Circuit Approach to Extracellular Microelectrodes. *IEEE Transactions on Biomedical Engineering* [online]. 07/1970, **BME-17**(3), pp. 238–247 [visited on 04/24/2023]. Available from DOI: 10.1109/TBME.1970.4502738.
31. BARZ, F et al. Versatile, modular 3D microelectrode arrays for neuronal ensemble recordings: from design to fabrication, assembly, and functional validation in non-human primates. *Journal of Neural Engineering* [online]. 06/01/2017, **14**(3), p. 036010 [visited on 04/24/2023]. Available from DOI: 10.1088/1741-2552/aa5a90.
32. SHIN, H. et al. 3D high-density microelectrode array with optical stimulation and drug delivery for investigating neural circuit dynamics. *Nature Communications* [online]. 01/21/2021, **12**(1), p. 492 [visited on 04/24/2023]. Available from DOI: 10.1038/s41467-020-20763-3.
33. RINCON MONTES, V. et al. Toward a Bidirectional Communication Between Retinal Cells and a Prosthetic Device - A Proof of Concept. *Frontiers in Neuro-*

- science* [online]. 04/30/2019, **13**, p. 367 [visited on 04/24/2023]. Available from DOI: 10.3389/fnins.2019.00367.
34. ZHAO, Z. et al. Parallel, minimally-invasive implantation of ultra-flexible neural electrode arrays. *Journal of Neural Engineering* [online]. 06/01/2019, **16**(3), p. 035001 [visited on 04/24/2023]. Available from DOI: 10.1088/1741-2552/ab05b6.
 35. GROB, L. et al. Inkjet-Printed and Electroplated 3D Electrodes for Recording Extracellular Signals in Cell Culture. *Sensors* [online]. 06/09/2021, **21**(12), p. 3981 [visited on 04/24/2023]. Available from DOI: 10.3390/s21123981.
 36. SALEH, M. S. et al. CMU Array: A 3D nanoprinted, fully customizable high-density microelectrode array platform. *Science Advances* [online]. 10/07/2022, **8**(40), eabj4853 [visited on 04/24/2023]. Available from DOI: 10.1126/sciadv.abj4853.
 37. FEINER, R. et al. Engineered hybrid cardiac patches with multifunctional electronics for online monitoring and regulation of tissue function. *Nature Materials* [online]. 06/2016, **15**(6), pp. 679–685 [visited on 04/24/2023]. Available from DOI: 10.1038/nmat4590.
 38. SOSCIA, D. A. et al. A flexible 3-dimensional microelectrode array for *in vitro* brain models. *Lab on a Chip* [online]. 2020, **20**(5), pp. 901–911 [visited on 04/24/2023]. Available from DOI: 10.1039/C9LC01148J.
 39. BROWN, M. A. et al. *Direct laser writing of 3D electrodes on flexible substrates* [online]. 2022-06-09. [visited on 04/24/2023]. preprint. Bioengineering. Available from DOI: 10.1101/2022.06.07.495165.
 40. KURSELIS, K. et al. 3D fabrication of all-polymer conductive microstructures by two photon polymerization. *Optics Express* [online]. 12/16/2013, **21**(25), p. 31029 [visited on 04/24/2023]. Available from DOI: 10.1364/OE.21.031029.
 41. SHAPIRA, A.; DVIR, T. 3D Tissue and Organ Printing - Hope and Reality. *Advanced Science* [online]. 05/2021, **8**(10), p. 2003751 [visited on 04/24/2023]. Available from DOI: 10.1002/advs.202003751.
 42. JAISWAL, A. et al. Two decades of two-photon lithography: Materials science perspective for additive manufacturing of 2D/3D nano-microstructures. *iScience* [online]. 04/2023, **26**(4), p. 106374 [visited on 04/24/2023]. Available from DOI: 10.1016/j.isci.2023.106374.

43. OFFENHAUESSER, A. *Lecture Biophysics I* [University Lecture]. 2020.
44. O'HALLORAN, S. et al. Two-Photon Polymerization: Fundamentals, Materials, and Chemical Modification Strategies. *Advanced Science* [online]. 03/2023, **10**(7), p. 2204072 [visited on 04/24/2023]. Available from DOI: 10.1002/advs.202204072.
45. WALLER, E.; FREYMANN, G. von. Spatio-Temporal Proximity Characteristics in 3D μ -Printing via Multi-Photon Absorption. *Polymers* [online]. 08/10/2016, **8**(8), p. 297 [visited on 04/24/2023]. Available from DOI: 10.3390/polym8080297.
46. JING, X. et al. Two-photon polymerization for 3D biomedical scaffolds: Overview and updates. *Frontiers in Bioengineering and Biotechnology* [online]. 08/22/2022, **10**, p. 994355 [visited on 04/24/2023]. Available from DOI: 10.3389/fbioe.2022.994355.
47. JIPA, F. et al. Femtosecond Laser Lithography in Organic and Non-Organic Materials. In: HOSAKA, S. (ed.). *Updates in Advanced Lithography* [online]. InTech, 07/03/2013 [visited on 04/24/2023]. ISBN 978-953-51-1175-7. Available from DOI: 10.5772/56579.
48. MORTIMER, C. E.; MUELLER, U. *Chemie: das Basiswissen der Chemie*. **13., vollstaendig bearbeitete Auflage**. Stuttgart New York: Georg Thieme Verlag, 2020. ISBN 978-3-13-242275-9 978-3-13-242274-2. Available from DOI: 10.1055/b-006-163279.
49. BARD, A. J.; FAULKNER, L. R.; WHITE, H. S. *Electrochemical methods: fundamentals and applications*. **Third edition**. Hoboken, NJ: Wiley, 2022. ISBN 978-1-119-33406-4.
50. PAUNOVIC, M.; SCHLESINGER, M. *Fundamentals of electrochemical deposition*. **2nd ed**. Hoboken, N.J: Wiley-Interscience, 2006. The Electrochemical Society series. ISBN 978-0-471-71221-3. OCLC: ocm62742655.
51. WEIDLICH, S. *Nanoscale 3D structures towards improved cell-chip coupling on microelectrode arrays*. 2017.
52. HARIRI, M. B.; DOLATI, A.; MOAKHAR, R. S. The Potentiostatic Electrodeposition of Gold Nanowire/Nanotube in $HAuCl_4$ Solutions Based on the Model of Recessed Cylindrical Ultramicroelectrode Array. *Journal of The Electrochemical*

- Society* [online]. 2013, **160**(6), pp. D279–D288 [visited on 04/17/2023]. Available from DOI: 10.1149/2.141306jes.
53. RIVNAY, J.; OWENS, R. M.; MALLIARAS, G. G. The Rise of Organic Bioelectronics. *Chemistry of Materials* [online]. 01/14/2014, **26**(1), pp. 679–685 [visited on 04/24/2023]. Available from DOI: 10.1021/cm4022003.
54. MORVANT, M. C.; REYNOLDS, J. R. In situ conductivity studies of poly(3,4-ethylenedioxythiophene). *Synthetic Metals* [online]. 01/1998, **92**(1), pp. 57–61 [visited on 04/24/2023]. Available from DOI: 10.1016/S0379-6779(98)80023-4.
55. LUDWIG, K. A. et al. Poly(3,4-ethylenedioxythiophene) (PEDOT) polymer coatings facilitate smaller neural recording electrodes. *Journal of Neural Engineering* [online]. 02/01/2011, **8**(1), p. 014001 [visited on 04/24/2023]. Available from DOI: 10.1088/1741-2560/8/1/014001.
56. PROCTOR, C. M.; RIVNAY, J.; MALLIARAS, G. G. Understanding volumetric capacitance in conducting polymers. *Journal of Polymer Science Part B: Polymer Physics* [online]. 08/2016, **54**(15), pp. 1433–1436 [visited on 04/24/2023]. Available from DOI: 10.1002/polb.24038.
57. CUI, X.; MARTIN, D. C. Electrochemical deposition and characterization of poly(3,4-ethylenedioxythiophene) on neural microelectrode arrays. *Sensors and Actuators B: Chemical* [online]. 03/2003, **89**(1), pp. 92–102 [visited on 04/24/2023]. Available from DOI: 10.1016/S0925-4005(02)00448-3.
58. PLATKIEWICZ, J.; BRETTE, R. A Threshold Equation for Action Potential Initiation. *PLoS Computational Biology* [online]. 07/08/2010, **6**(7), e1000850 [visited on 04/24/2023]. Available from DOI: 10.1371/journal.pcbi.1000850.
59. LEWEN, J. *Quantification and improvement of the electric coupling between electrogenic cells and microelectrode arrays by nanocavities and nanostructures* [online]. 2020. [visited on 04/24/2023]. Available from DOI: 10.18154/RWTH-2020-11697. PhD thesis. RWTH Aachen University. Artwork Size: pages 1 Online-Ressource (iii, 115 Seiten) : Illustrationen, Diagramme Pages: pages 1 Online-Ressource (iii, 115 Seiten) : Illustrationen, Diagramme Publication Title: Dissertation Volume: RWTH Aachen University.

-
60. HE, B. (ed.). *Neural engineering*. Third edition. Cham: Springer, 2020. ISBN 978-3-030-43395-6 978-3-030-43394-9. Available from DOI: 10.1007/978-3-030-43395-6.
61. POZNANSKI, R. R. Book Review: "Theoretical Neuroscience: Computational and Mathematical Modeling of Neural Systems", P. Dayan and L. F. Abbott, eds., (2001). *Journal of Integrative Neuroscience* [online]. 09/2006, **05**(3), pp. 489–491 [visited on 04/24/2023]. Available from DOI: 10.1142/S0219635206001197.
62. NAKAMURA, M. et al. Outer Helmholtz Plane of the Electrical Double Layer Formed at the Solid Electrode-Liquid Interface. *ChemPhysChem* [online]. 06/06/2011, **12**(8), pp. 1430–1434 [visited on 04/24/2023]. Available from DOI: 10.1002/cphc.201100011.
63. RINCON MONTES, V. *Development, characterization, and application of intraretinal implants*. **RWTH Aachen University** [online]. In collab. with OFFENHAEUSSER, A.; INGEBRANDT, S.; FITTER, J. RWTH Aachen University, 2021 [visited on 04/24/2023]. Available from DOI: 10.18154/RWTH-2021-06382. Artwork Size: pages 1 Online-Ressource : Illustrationen, Diagramme Pages: pages 1 Online-Ressource : Illustrationen, Diagramme Publication Title: Dissertation.
64. SPIRA, M. E.; HAI, A. Multi-electrode array technologies for neuroscience and cardiology. *Nature Nanotechnology* [online]. 02/2013, **8**(2), pp. 83–94 [visited on 04/24/2023]. Available from DOI: 10.1038/nnano.2012.265.
65. SCHMICKLER, W.; SANTOS, E. *Interfacial electrochemistry*. **2nd ed.** Heidelberg ; New York: Springer, 2010. ISBN 978-3-642-04936-1. OCLC: ocn455830945.
66. GARDNER, E. D. *Fundamentals of Neurology*. 1947.
67. KOLB, B.; GIBB, R.; ROBINSON, T. E. Brain Plasticity and Behavior. *Current Directions in Psychological Science* [online]. 02/2003, **12**(1), pp. 1–5 [visited on 04/24/2023]. Available from DOI: 10.1111/1467-8721.01210.
68. LONDON, A.; BENHAR, I.; SCHWARTZ, M. The retina as a window to the brain - from eye research to CNS disorders. *Nature Reviews Neurology* [online]. 01/2013, **9**(1), pp. 44–53 [visited on 04/24/2023]. Available from DOI: 10.1038/nrneurol.2012.227.

69. NEUROSCIENCE, F. O. *VISION: THE RETINA* [online]. 2023. [visited on 05/11/2023]. Available from: <https://openbooks.lib.msu.edu/neuroscience/chapter/vision-the-retina/>.
70. TRONCOSO, X. G.; MACKNIK, S. L.; MARTINEZ-CONDE, S. Vision's First Steps: Anatomy, Physiology, and Perception in the Retina, Lateral Geniculate Nucleus, and Early Visual Cortical Areas. In: DAGNELIE, G. (ed.). *Visual Prosthetics* [online]. Boston, MA: Springer US, 2011, pp. 23–57 [visited on 04/24/2023]. ISBN 978-1-4419-0753-0 978-1-4419-0754-7. Available from DOI: 10.1007/978-1-4419-0754-7_2.
71. SZOSTAK, K. M.; GRAND, L.; CONSTANDINOU, T. G. Neural Interfaces for Intracortical Recording: Requirements, Fabrication Methods, and Characteristics. *Frontiers in Neuroscience* [online]. 12/07/2017, **11**, p. 665 [visited on 04/24/2023]. Available from DOI: 10.3389/fnins.2017.00665.
72. AYTON, L. N. et al. An update on retinal prostheses. *Clinical Neurophysiology* [online]. 06/2020, **131**(6), pp. 1383–1398 [visited on 04/24/2023]. Available from DOI: 10.1016/j.clinph.2019.11.029.
73. NANOSCRIBE GMBH, G. *NanoGuide* [online]. 2023. [visited on 05/11/2023]. Available from: <https://support.nanoscribe.com/hc/en-gb/articles/360001755654-IP-L>.
74. GUSNARD, D.; KIRSCHNER, R. H. Cell and organelle shrinkage during preparation for scanning electron microscopy: effects of fixation, dehydration and critical point drying. *Journal of Microscopy* [online]. 05/1977, **110**(1), pp. 51–57 [visited on 04/24/2023]. Available from DOI: 10.1111/j.1365-2818.1977.tb00012.x.
75. XU, H. et al. Acute *in vivo* testing of a conformal polymer microelectrode array for multi-region hippocampal recordings. *Journal of Neural Engineering* [online]. 02/01/2018, **15**(1), p. 016017 [visited on 04/24/2023]. Available from DOI: 10.1088/1741-2552/aa9451.
76. DIJK, H. W. van et al. Decreased Retinal Ganglion Cell Layer Thickness in Patients with Type 1 Diabetes. *Investigative Ophthalmology & Visual Science* [online]. 07/01/2010, **51**(7), p. 3660 [visited on 04/24/2023]. Available from DOI: 10.1167/iovs.09-5041.

77. PRINZ, G. *Fabrication of Integrated Gold Microelectrodes in 3D Scaffolds by Electrodeposition*. 2021.
78. PLEEGING, R. et al. Polymer nano manufacturing of a biomimicking surface for kidney stone crystallization studies. *Micro and Nano Engineering* [online]. 11/2021, **13**, p. 100094 [visited on 04/17/2023]. Available from DOI: 10.1016/j.mne.2021.100094.
79. WEIDLICH, S. et al. MEAs and 3D nanoelectrodes: electrodeposition as tool for a precisely controlled nanofabrication. *Nanotechnology* [online]. 03/03/2017, **28**(9), p. 095302 [visited on 04/24/2023]. Available from DOI: 10.1088/1361-6528/aa57b5.
80. SRIKANTHARAJAH, K. *Development, characterization, and application of compliant intracortical implants*. **RWTH Aachen University** [online]. In collab. with OFFENHAEUSSER, A.; INGEBRANDT, S. RWTH Aachen University, 2021 [visited on 04/24/2023]. Available from DOI: 10.18154/RWTH-2021-11377.
81. RUGGIERO, A. et al. Two-photon polymerization lithography enabling the fabrication of PEDOT:PSS 3D structures for bioelectronic applications. *Chemical Communications* [online]. 2022, **58**(70), pp. 9790–9793 [visited on 04/17/2023]. Available from DOI: 10.1039/D2CC03152C.
82. KUSKO, M. et al. Design, Fabrication and Characterization of a Low-Impedance 3D Electrode Array System for Neuro-Electrophysiology. *Sensors* [online]. 12/03/2012, **12**(12), pp. 16571–16590 [visited on 04/24/2023]. Available from DOI: 10.3390/s121216571.
83. WANG, A. et al. Impedance Characterization and Modeling of Subcellular to Micro-sized Electrodes with Varying Materials and PEDOT:PSS Coating for Bioelectrical Interfaces. *ACS Applied Electronic Materials* [online]. 12/28/2021, **3**(12), pp. 5226–5239 [visited on 04/17/2023]. Available from DOI: 10.1021/acsaelm.1c00687.
84. STAVRINIDOU, E. et al. A physical interpretation of impedance at conducting polymer/electrolyte junctions. *AIP Advances* [online]. 01/2014, **4**(1), p. 017127 [visited on 04/24/2023]. Available from DOI: 10.1063/1.4863297.
85. DENLINGER, B. et al. Local photoreceptor degeneration causes local pathophysiological remodeling of retinal neurons. *JCI Insight* [online]. 01/30/2020, **5**(2), e132114 [visited on 05/16/2023]. Available from DOI: 10.1172/jci.insight.132114.

List of Figures

Fig. 1	Structure of the work. Part 1 illustrates the workflow for 3D scaffold system. Part 2 shows the new platform for real three-dimensional electrodes. Finally, part 3 combines part 1 and 2 with integrating 3D electrodes into the scaffold system.	5
Fig. 2	Theory of one photon and two photon absorption process. The fluorescence indicates the high resolution of the two-photon process [43].	8
Fig. 3	Illustration of voxels being printed next to each other to realize the 3D geometry [18].	11
Fig. 4	Illustration of the electrical circuit of a three electrode arrangement [51].	14
Fig. 5	Illustration of a typical action potential stimulus. Important parts are indicated [59].	19
Fig. 6	Schematic of a neuron. Important parts of the cell are indicated [61].	20
Fig. 7	Illustration of a typical interface between the electrode and the electrolyte. Important parts are indicated [51].	22
Fig. 8	Illustration of the electrical equivalent circuit at the interface between cell and electrode. The simplified Randles Cell model is applied [63].	23
Fig. 9	Overall structure of the eye. The retina consists of several layers with different cell types [69].	27
Fig. 10	Schematic of a typical 2D multi electrode chip with electrode openings in the center of the chip [51].	30
Fig. 11	Approach to create 3D neuronal networks with the help of a printed stiff scaffold. a) Liquid droplet of photopolymer IP-L 780 on a glass substrate. b) Printed cage geometry after development of the structure. c) Coat polymer with Poly-L-Lysine and define seeding volume.d) Seed primary cortical rat neurons onto the printed geometry. e) Stack cages onto each other to create third dimension.	42
Fig. 12	CAD design of a single cage. Illustration of the difference in Type A and Type B designs.	42

Fig. 13	Illustration of the sliced and hatched scaffold design in DeScribe (NanoScribe GmbH, Germany).	43
Fig. 14	Difference between a hatching angle of 0 degree (left) and 90 degrees (right). Especially round structures are printed more homogeneously with a hatching angle of 90 degrees.	44
Fig. 15	Light microscopy pictures of printed cage scaffolds in a 4X4 diamond shape array. Too less laser power leads to unstable small features.	45
Fig. 16	Light microscopy pictures of a stable 4X4 cage array (left). Zoomed in picture of stable smallest features (right).	45
Fig. 17	SEM picture of a printed cage scaffold. The single steps at the surface of the cage edges due to hatching and slicing can be seen.	46
Fig. 18	CAD design of 4X4 cage array including the carrying system and alignment blocks.	48
Fig. 19	Carrying procedure using the carrying system and a thin glass pipette. Left: Focus is set to the substrate surface; right: Focus is set to the lifted up cage array.	48
Fig. 20	Stacking process in water. Due to the hydrophobic nature of the polymer air bubbles are trapped underneath the cage array and hinder the stacking procedure.	49
Fig. 21	CAD design of the a 4X4 cage array with integrated guiding rods to improve the stack stability.	50
Fig. 22	CAD design of the upper 4X4 cage arrays with adjusted alignment blocks. The designed holes are bigger at the bottom (right image) and match with the guiding rod diameter at the top (left image).	51
Fig. 23	Light microscope image of a stable and perfect aligned final stack of 5 cage layers. Left: Focus is set to the alignment blocks of the upper most cage array; right: Focus is set to the top of the guiding rod.	51
Fig. 24	Left: Light microscopy picture of an 4X4 cage array surrounded by neurons; right: Light microscopy picture of a removed 4X4 cage array after cell seeding.	54

Fig. 25	Light microscopy image of a stacking procedure with cells. Cells and remaining tissue sticking to the guiding rods and carrying system prevent a stable stacking process.	55
Fig. 26	Light microscopy image of a detached and tiled stack. Again cells sticking to the guiding rods prevent the upper array from sliding down the rod	56
Fig. 27	Left: Light microscopy image of the stacking procedure with the use of a microtweezer; right: Light microscopy side view of a three layer stack.	57
Fig. 28	Light microscopy image of a released grabbed alignment block due to too high adhesion of the cage array to the substrate.	58
Fig. 29	Light microscopy image of a successful stack of 3 cage layers with cells.	59
Fig. 30	Fluorescent microscopy image of a 2 layer stack with the membrane labeling dye Dil. Left: Focus is set to the substrate surface; right: Focus is set to the second cage array.	60
Fig. 31	Fluorescent microscopy image of a 2 layer stack. Left: Membrane labeling dye Dil; right: Membrane labeling dye Cell Mask deep red.	61
Fig. 32	High resolution fluorescent microscopy image of a 2 layer stack with the membrane labeling dye Cell Mask deep red. Cell bodies as well as cell connections via axons and dendrites are indicated.	61
Fig. 33	Scanning electron microscopy image of a two layer stack. Cell bodies inside the cages are indicated.	63
Fig. 34	Scanning electron microscopy image of cell bodies and their connections at two different positions of the cage stack.	63
Fig. 35	Schematic of the concept for introducing high aspect ration 3D microelectrodes.	65
Fig. 36	CAD design of the hollow cylinders which act as templates for the electrochemical deposition. Important structure dimensions are indicated.	66
Fig. 37	Scanning electron microscopy top view images of hollow cylinders. Left: Printed with a 25X objective; right: Printed with a 63X objective.	67

Fig. 38	Scanning electron microscopy top view images of hollow cylinders printed with the 25X objective. Left: 12 μm outer diameter; right: 20 μm outer diameter.	68
Fig. 39	Light microscopy image of hollow cylinders printed with low degree of polymerization and thus leading to structural deformation. . . .	69
Fig. 40	Scanning electron microscopy images of cylinders with too low adhesion to the substrate. Gold grows not only inside the template but also underneath [77].	70
Fig. 41	Light microscopy image of hollow cylinders printed around the electrode openings of a 2D MEA. Gold caps at the top indicate a successful deposition through the cylinders.	72
Fig. 42	Scanning electron microscopy image of a 2D MEA after gold electrodeposition. Big gold clumps grew through pinholes in the passivation.	73
Fig. 43	Scanning electron microscopy image of high aspect ratio cylinders which collapsed during the development process.	75
Fig. 44	Scanning electron microscopy image of cylinders with 500 μm height, 200 μm spacing and different outer diameters as well as wall thicknesses. The first number represents the outer diameter and the second number the wall thickness in μm	76
Fig. 45	Scanning electron microscopy images illustrating the challenge of misalignment due to block splitting in z direction. Left: side view; right: top view.	77
Fig. 46	Scanning electron microscopy image of a 8X8 cylinder arrays with 12 μm outer diameter and 2 μm wall thickness and heights ranging from 200 μm to 500 μm	78
Fig. 47	Scanning electron microscopy image of cone shape cylinder structures with a bottom cone diameter of 12 μm (left) and 20 μm (right). The distance of the cylinders is 25 μm and the height is 150 μm . . .	79
Fig. 48	CAD design of cylinders stabilised by wings to increase the effective bending stiffness.	80
Fig. 49	CAD design of a first concept idea to improve penetration behaviour of high aspect ratio 3D electrodes. The important parts are indicated.	81

Fig. 50	2D in vitro layouts. Left: Layout with 64 electrodes arranged in an 8x8 square matrix; right: 3D printed cylinders with different heights around the electrode openings.	82
Fig. 51	2D ex-vivo layouts for flexible implants with electrode distances of 106 μm (a), 16 μm (b), 36 μm (c) and 56 μm (d).	83
Fig. 52	2D ex-vivo layout. Left: Layout with 16 electrodes with 36 μm electrode distance; right: 3D printed cylinders with different heights around the electrode openings (right).	84
Fig. 53	Image of flexible implant after microfabrication and packaging. The important parts of the implant are indicated.	85
Fig. 54	Schematic view of a current-time curve for an electrochemical deposition process of gold. Four different stages are highlighted with a specific current rate and filling level of different cylinders.	87
Fig. 55	Scanning electron microscopy image of a dendrite like gold overgrowth which results in a short cut between the single cylinders.	88
Fig. 56	Light microscopy image of several cylinders with the same height. The different gold cap sizes at the top of 4 cylinders have been achieved with different deposition parameters.	89
Fig. 57	Left: Scanning electron microscopy image of a filled and tilted cylinder; right: Side view of a FIB cut through a filled and tilted cylinder.	90
Fig. 58	Analytically calculated gold string diameter for cylinders with 150 μm and 60 μm height.	91
Fig. 59	Scanning electron microscopy top view image of a printed cylinder. Left: Before gold deposition; right: After gold deposition with -100 nA for 20 s	92
Fig. 60	Light microscopy image of printed cylinders with 150 μm height. Applying -200 nA for 1 min leads to gold caps of around 20 μm diameter.	93
Fig. 61	Light microscopy image of printed cylinders with the same height. The dark caps at the top of each cylinder indicate a successful PEDOT:PSS deposition process.	95

Fig. 62	Scanning electron microscopy image of printed cylinders with different heights with deposited PEDOT:PSS caps after 5 cycles at the top of each cylinder. The big electrode at the back of the image is the reference electrode of the 2D MEA chip.	97
Fig. 63	Scanning electron microscopy image of printed cylinders. Left: Before PEDOT:PSS deposition; right: After PEDOT:PSS deposition.	98
Fig. 64	Scanning electron microscopy image of printed cylinders on a multi-site layout. PEDOT:PSS caps are deposited on top of the cylinders with using 2 cycles of the CV technique.	99
Fig. 65	EIS curve of electrodes before and after 3D printing as well as before and after an oxygen plasma treatment.	101
Fig. 66	Phase shift curve of electrodes before and after 3D printing as well as before and after oxygen plasma treatment.	102
Fig. 67	Difference in impedance at 1 kHz for gold 3D electrodes fabricated with applying -100 nA for 20 s and -200 nA for 1 min as second deposition step.	103
Fig. 68	Light microscopy image of printed cylinders. Left: After gold deposition; right: After additional PEDOT:PSS deposition.	104
Fig. 69	Comparison of EIS measurements of 3D electrodes deposited with gold and PEDOT:PSS.	105
Fig. 70	Comparison of the phase shift measurements of 3D electrodes deposited with gold and PEDOT:PSS.	106
Fig. 71	Left: Comparison of EIS measurements of PEDOT:PSS coated 3D electrodes deposited with different cycle numbers; right: The light microscopy image shows the corresponding cap sizes after deposition.	106
Fig. 72	Current-time curves of a 5 cycle deposition process of PEDOT:PSS. In both electrodes almost the same amount of current flows.	107
Fig. 73	Current-time curves of a 2 cycle deposition process of PEDOT:PSS. In both electrodes different amounts of current flows.	107
Fig. 74	Comparison of impedance at 1 kHz for 3D electrodes coated with PEDOT:PSS using 2, 5 and 10 cycles.	108

Fig. 75	Illustration of the experimental set up for the top-down approach of flexible implants.	110
Fig. 76	Light microscope image of the top-down insertion of a flexible implant. The important parts are indicated.	111
Fig. 77	Recording of spontaneous activity from extracted rat retina tissue with using the multi-site layout at different insertion depths. Due to the short distance of the electrodes they measure the signals from the same cells. The signal changes with stepwise insertion (Z). . .	112
Fig. 78	Recording of cell activities during light stimulation of extracted rat retina tissue.	114
Fig. 79	Recording of light stimulated cells inside an extracted rat retina tissue.	114
Fig. 80	Recording of spontaneous cell activity from extracted rat retina tissue during the extraction of the implant.	115
Fig. 81	Recording of spontaneous activity from human brain slices in different depths. Before the point of insertion, no signals can be recorded.	116
Fig. 82	Illustration of the experimental set up for the bottom-up approach of stiff probes.	118
Fig. 83	Recordings of spontaneous cell activity within an extracted rat retina tissue after placing the tissue on top of the 3D MEA.	118
Fig. 84	Recording of light stimulated cells inside an extracted rat retina tissue with stiff probes.	119
Fig. 85	Recording of AP shape signals during the light stimulation of the rat retina tissue.	119
Fig. 86	Left: EIS measurements of 3D electrodes before and after tissue insertion; right: Light microscopy image of the PEDOT:PSS caps on top of the cylinders before and after insertion.	120
Fig. 87	Scanning electron microscopy image of the multi-site layout after tissue insertion. Left: Before redeposition of PEDOT:PSS; right: After redeposition of PEDOT:PSS.	121
Fig. 88	CAD design of the 3D cage-like scaffolds with integrated 3D cylinders.	123

Fig. 89	Schematic approach of integrating 3D electrodes to the scaffold system to record electrical signals of 3D in-vitro neuronal systems.	124
Fig. 90	Light microscopy image of the 2D MEA with 32 electrode openings. Left: Before 3D printing; right: After 3D printing.	125
Fig. 91	Fluorescent microscopy image of a 3D in-vitro neuronal network inside a printed cage scaffold system. Left: The focus is set to the substrate surface; right: The focus is set to the height of the lower cylinders.	126
Fig. 92	Fluorescent microscopy image of a 3D in-vitro neuronal network inside a printed cage scaffold system. Left: The scaffold is not printed all the way up to the high cylinders; right: The scaffold is printed all the way up to the high cylinders.	127
Fig. 93	Fluorescent microscopy image of a neuronal network around printed cylinders labeled with SiR-actin. The focus is set to the substrate surface (a) and 6 μm (b) as well as 10 μm (c) away from the substrate.	128
Fig. 94	Scanning electron microscopy top view image of fixed neurons inside a printed 3D scaffold with integrated filled cylinders.	129
Fig. 95	Scanning electron microscopy top view image of fixed neurons inside a printed 3D scaffold with integrated filled cylinders.	130
Fig. 96	Scanning electron microscopy side view image of the interaction between the neurons and two cylinders with different heights within the 3D scaffold.	131
Fig. 97	Characterization of 3D electrodes within a scaffold system. Left: Light microscopy image of gold filled cylinders; right: EIS curves of the corresponding 3D electrodes.	132
Fig. 98	Scanning electron microscopy image of a high density culture of cortical, embryonic rat neurons on top of a 3D scaffold system. . .	133
Fig. 99	Recording of spontaneous activities of an in-vitro 3D neuronal network. The light microscope image illustrates the location of each recording within the network.	134

Fig. 100	Recording of spontaneous activities of an in-vitro 3D neuronal network. The recorded signals of all three electrodes differ in amplitude and shape.	135
Fig. 101	Recording of spontaneous activities of an in-vitro 3D neuronal network. The light microscope image illustrates the location of each recording within the network.	136
Fig. 102	Light microscopy image of a printed scaffold with integrated filled cylinders after five electrophysiological measurements.	137

Acknowledgements

I would like to thank my family, my friends and all the colleagues at the IBI-3 institute for their help and support during my research and writing process. In particular I would like to thank the following people.

First of all a big thanks to **Prof. Dr. Offenhäusser** for giving me the opportunity to write my PhD in such a great institute. Your great supervision, constant support, and very helpful scientific and non-scientific discussions helped me a lot to successfully conduct my PhD. It was a pleasure for me how you always have tried to encourage us to work together as a team, in science as well as social life.

Thank you, **Prof. Dr. Fitter**, for accepting to be the second examiner of my work.

A huge thanks to **Marie** for your constant support. It was a great pleasure working with you. I hope you had as much fun as I had whenever we did an experiment together (successfully as always!).

I also would like to thank **Regina** for your fabrication support as well as the very helpful discussions we had. Your microfabrication expertise helped me a lot.

Johannes, thank you very much for your very useful support in CATIA especially at the beginning of my work.

Huge thanks also to **Vanessa** and **Dirk** for helping me to overcome all the biological as well as chemical challenges during my PhD. I really enjoyed the interdisciplinary atmosphere in the institute and it helped me a lot to have such huge knowledge in biology and chemistry around.

Thank you, **Tina** for your amazing character, your support with everything and your good mood. Please stay as you are so that everyone in the institute can benefit from you.

I also would like to thank the in-vivo group, **Viviana**, **Lina**, **Simon** for supporting me with all the animal experiments.

I would like to thank the all the HNF staff, for keeping the Clean Room organized. In particular, I would like to thank **Sven** for your great help with the NanoScribe.

Furthermore, thank you, **Elke** and **Elmar** for your support with the SEM and the FIB cuts and all the useful input.

I would like to thank **Michael** and **Marko** for your constant advises regarding microfabrication challenges. You saved me a lot of time.

I would like to thank **Susanne** for all the organisational stuff regarding the institute.

I would like to thank all the electronic workshop for your technical support and especially for your fast responses.

Gregor and **Amine** it was an honor for me being your supervisor. I have learned a lot from you.

Thanks to **Viviana** for being the best neighbour in the world and giving me a ride to the FZJ whenever I needed it.

Big thanks also to you **Bohdan**. The football games we played together were always a lot of fun.

Marie, Viviana, Pegah, Bohdan, Lina, Colin, Justus, Alwin, Bogdana, Mateo, Erkan and all the IBI-3 members, it was such a great pleasure to work and socialize with you. I will never forget the huge fun we had together during all our nice activities.

Thanks to all my friends. I always enjoy the time with you. Huge thanks also to my **Parents** and **Brothers** for the support during my whole live so far. Without you I would not be where I am today.

Thanks to you, **Nora**, for being always by my side and supporting me unquestioningly. Thanks for everything!!

Band / Volume 89

Controlling the electrical properties of oxide heterointerfaces through their interface chemistry

M.-A. Rose (2022), vi, 162 pp

ISBN: 978-3-95806-667-0

Band / Volume 90

Modeling and Suppressing Unwanted Parasitic Interactions in Superconducting Circuits

X. Xu (2022), 123, XVIII pp

ISBN: 978-3-95806-671

Band / Volume 91

Activating molecular magnetism by controlled on-surface coordination.

Cojocariu (2022), xi, 169 pp

ISBN: 978-3-95806-674-8

Band / Volume 92

Computational study of structural and optical properties of two-dimensional transition-metal dichalcogenides with implanted defects

S. H. Rost (2023), xviii, 198 pp

ISBN: 978-3-95806-682-3

Band / Volume 93

DC and RF characterization of bulk CMOS and FD-SOI devices at cryogenic temperatures with respect to quantum computing applications

A. Artanov (2023), xv, 80, xvii-lviii pp

ISBN: 978-3-95806-687-8

Band / Volume 94

HAXPES study of interface and bulk chemistry of ferroelectric HfO₂ capacitors

T. Szyjka (2023), viii, 120 pp

ISBN: 978-3-95806-692-2

Band / Volume 95

A brain inspired sequence learning algorithm and foundations of a memristive hardware implementation

Y. Bouhadjar (2023), xii, 149 pp

ISBN: 978-3-95806-693-9

Band / Volume 96

Characterization and modeling of primate cortical anatomy and activity

A. Morales-Gregorio (2023), ca. 260 pp.

ISBN: 978-3-95806-698-4

Band / Volume 97

Hafnium oxide based memristive devices as functional elements of neuromorphic circuits

F. J. Cüppers (2023), vi, ii, 214 pp

ISBN: 978-3-95806-702-8

Band / Volume 98

Simulation and theory of large - scale cortical networks

A. van Meegen (2023), ca. 250 pp

ISBN: 978-3-95806-708-0

Band / Volume 99

Structure of two-dimensional multilayers and topological superconductors: surfactant mediated growth, intercalation, and doping

Y.-R. Lin (2023), x, 111 pp

ISBN: 978-3-95806-716-5

Band / Volume 100

Frequency mixing magnetic detection for characterization and multiplex detection of superparamagnetic nanoparticles

A. M. Pourshahidi (2023), X, 149 pp

ISBN: 978-3-95806-727-1

Band / Volume 101

Unveiling the relaxation dynamics of Ag/HfO₂ based diffusive memristors for use in neuromorphic computing

S. A. Chekol (2023), x, 185 pp

ISBN: 978-3-95806-729-5

Band / Volume 102

Analysis and quantitative comparison of neural network dynamics on a neuron-wise and population level

R. Gutzen (2024), xii, 252 pp

ISBN: 978-3-95806-738-7

Band / Volume 103

3D Scaffolds with Integrated Electrodes for Neuronal Cell Culture

J. Abu Shihada (2024), vii, 163 pp

ISBN: 978-3-95806-756-1

Information

Band / Volume 103

ISBN 978-3-95806-756-1

Mitglied der Helmholtz-Gemeinschaft

